A Magnetic Semiconductor based Non-Volatile Memory and Logic Element

Dissertation

zur Erlangung des
naturwissenschaftlichen Doktorgrades
der Julius-Maximilians-Universität Würzburg

vorgelegt von
Stefan Mark
aus Essfeld \ Bayern

Würzburg 2011

Eingereicht am: August 2011

bei der Fakultät für Physik und Astronomie

Gutachter der Dissertation:

1. Gutachter: Prof. Dr. Laurens W. Molenkamp

2. Gutachter: Prof. Dr. Ralph Claessen

3. Gutachter: Prof. Dr. Dieter Weiss

Prüfer im Promotionskolloquium:

1. Prüfer: Prof. Dr. Laurens W. Molenkamp

2. Prüfer: Prof. Dr. Ralph Claessen

3. Prüfer: Prof. Dr. Björn Trauzettel

Tag des Promotionskolloquiums: 04.05.2012

Doktorurkunde ausgehändigt am: ...

Parts of this thesis have been published elsewhere; other manuscripts are in preparation:

- C. Gould, S. Mark, K. Pappert, R. G. Dengel, J. Wenisch, R. P. Campion, A. W. Rushforth, D. Chiba, Z. Li, X. Liu, W. Van Roy, H. Ohno, J. K. Furdyna, B. Gallagher, K. Brunner, G. Schmidt, L. W. Molenkamp, *An extensive comparison of anisotropies in MBE grown (Ga, Mn)As material*, New Journal of Physics **10**, No. 055007 (2008);
- S. Mark, C. Gould, K. Pappert, J. Wenisch, K. Brunner, G. Schmidt, L. W. Molenkamp, *Independent Magnetization Behavior of a Ferromagnetic Metal/Semiconductor Hybrid System*, Editors Suggestion, Physical Review Letters **103**, No. 017204 (2009);
- S. Mark, P. Dürrenfeld, K. Pappert, L. Ebel, K. Brunner, C. Gould, L. W. Molenkamp, *Fully electrically read-write device out of a ferromagnetic semiconductor*, Editors Suggestion and a Synopsis in Physics, Physical Review Letters, Vol. **106**, No. 057204 (2011);
- F. Greullet, L. Ebel and F. Münzhuber and S. Mark and G. V. Astakhov and T. Kiessling and C. Schumacher and C. Gould and K. Brunner and W. Ossau and L. W. Molenkamp *Induced magnetic anisotropy in lifted (Ga,Mn)As thin films*, Applied Physics Letters **98**, No. 231903 (2011);
- S. Mark, L. Ebel, K. Brunner, C. Gould, and L.W. Molenkamp *Local domain sensing with nanostructured TAMR probes*, Applied Physics Letters **99**, No. 202504 (2011);
- S. Mark, L. Ebel, K. Brunner, C. Gould, and L.W. Molenkamp *Read-Out of the Logic Device*, Manuscript in preparation (2011);

Contents

Zusammenfassung **4**

Summary **8**

1 Introduction **9**

2 (Ga,Mn)As, a Ferromagnetic Semiconductor **13**
- 2.1 Ferromagnetism in (Ga,Mn)As 13
- 2.2 Magnetic Anisotropies in (Ga,Mn)As 16
- 2.3 Transport Properties of (Ga,Mn)As 19
- 2.4 A Comparison of Anisotropies in MBE Grown (Ga,Mn)As Material 22

3 FM Metal/Semiconductor Hybrid System **25**
- 3.1 Permalloy Layers 26
  - 3.1.1 Exchange Bias 26
  - 3.1.2 Permalloy with Cap Layer 27
  - 3.1.3 Permalloy without Cap Layer 32
- 3.2 Independent Magnetization Behavior 34

4 Tunneling **45**
- 4.1 Metal-Insulator-Semiconductor Tunneling 45
- 4.2 TAMR 48

5 Micron and Submicron TAMR Probes **53**
- 5.1 AlOx Tunnel Barrier 53
  - 5.1.1 Electrical Properties of the AlOx Barrier 54
  - 5.1.2 Local Domain Sensing with Nanostructured TAMR Probes 59
  - 5.1.3 T-dependence of a nano-TAMR Probe 64
- 5.2 Epitaxial (Al,Ga)As barrier 67

6 Fully Electrical Read-Write Device Out of (Ga,Mn)As **71**
- 6.1 Read-Write Processing 71
- 6.2 Read-Write Device Design 76
- 6.3 Read-Write Device Operation 81

7 Domain Wall Resistance in (Ga,Mn)As **91**

8 Programmable Logic Device **95**
8.1 Characterization of the Individual Logic Bits 95
8.2 Logic Device Operation 98

9 Conclusion and Outlook **105**

A Uniaxial Nanobars **107**

B Picture Gallery **111**

Bibliography **119**

Zusammenfassung

Die Entdeckung des Riesenmagnetowiderstands (giant magneto resistance, GMR) im Jahr 1980 von P. Grünberg and A. Fert gilt als Durchbruch, der zum Beginn des Spintronincs Forschungsgebietes führt und die Speicherindustrie revolutioniert. 1997 ist IBM das erste Unternehmen, das GMR basierte Speicher-Köpfe in konventionellen Festplatten einsetzt. Bis heute dominieren die GMR Speicher-Köpfe und deren Weiterentwicklungen den Speichermarkt. Durch die stetig wachsenden Herausforderungen das Moor'sche Gesetz zu erfüllen, die fortwährende Miniaturisierung und immer neue Erfolge der Speicherindustrie, werden die fundamentalen Grenzen der Physik, wie atomare Grösseneinheiten, vermutlich 2020 erreicht. Diese Zukunftsaussicht lässt die Halbleiter-Industrie nach neuen innovativen Technologien jenseits von CMOS [Inte 11] streben. Ein gravierender Nachteil der heutigen Computerarchitektur sind die elektrischen Verbindungen, die die Information zwischen Halbleiter basierter Datenverarbeitung und metallischen Speicherelementen transportieren. Solche Verbindungen sind maßgeblich für die Wärmeentwicklung in Computern verantwortlich. Ein Konzept, indem Speicherelemente und Datenverarbeitung in einem einzigen Element vereint sind, kommt ohne diese Verbindungen aus. Um dieses Problem zu lösen, sucht die Spinelektronik zur Zeit nach einem Halbleiterbauelement, das rein elektrisch betrieben werden kann. Die Realisierung eines solchen Bauelements aus dem ferromagnetischen Halbleiter (Ga,Mn)As wird in dieser Arbeit gezeigt.

In Kapitel 2 führen wir den zur Zeit am besten kontrollierbaren ferromagnetischen Halbleiter (Ga,Mn)As ein. Das Material dient als ideale Umgebung für Transportuntersuchungen an Systemen, die die Zustandsdichte und die magnetischen Anisotropien über die Spin-Bahn-Kopplung verbinden. Die Vielfalt an Anisotropien in (Ga,Mn)As sind von verschiedenen Parametern, wie MBE Wachstumsbedingungen, Substrat Gitterkonstante und Dotierkonzentration abhängig. Zur Charakterisierung des Materials nutzen wir Transportmessungen, um die verschiedenen magnetischen Anisotropien zu bestimmen.

Während das hauptsächliche Thema dieser Arbeit ein progrmmierbares Logikelement ist, zeigen wir in einem zusätzlichen Kapitel (3) ein ferromagnetisches Metall/Halbleiter Hybridsystem. Ein praktisches Hindernis von (Ga,Mn)As zur kommerziellen Nutzung des Materials ist die niedrige Curietemperatur. Ein vielversprechender Versuch dieses Problem zu lösen, ist die Nutzung von Hybridsystemen, die aus ferromagnetischen Met-

all/ferromagnetischen Halbleiter Heterostrukturen bestehen. Der Magnetismus der metallischen Schicht kann in diesen Systemen genutzt werden, um die magnetischen Eigenschaften des Halbleiters zu verstärken und ein Weg sein, um T_C zu stabilisieren und zu vergrößern. Die magnetische Kopplung an der Grenzschicht zwischen Metall und Halbleiter ist natürlich entscheidend für potentielle Anwendungen. Die Magnetisierung der einzelnen Schichten verhalten sich unabhängig voneinander, obwohl keine nicht-magnetische Zwischenschicht vorhanden ist. Die Unabhängigkeit der beiden magnetischen Schichten wird durch Transportmessungen und durch direkte Magnetisierungsmessungen mittels SQUID (superconducting quantum interference device) bestätigt. Wir nutzen die magnetische Unabhängigkeit des Zwei-Schicht Hybridsystems um ein Speicherelement mit vier nicht-flüchtigen Zuständen bei Null-Feld zu demonstrieren.

Für die Realisierung eines programmierbaren Logikelements oder beliebiger nanometer grosser Bauteile, brauchen wir eine verlässlige Methode, um die Magnetisierungsrichtung lokaler Domänen auzulesen. Dafür erweitern wir die Untersuchungen an TAMR (tunneling magneto resistance) Strukturen und skalieren die Fläche des Tunnelkontakts von 100 µm auf 260 nm. In Kapitel 4 geben wir zunächst eine theoretische Beschreibung des TAMR Effekts und zeigen darauf im folgenden Kapitel 5 experimentelle Daten der miniaturisierten Tunnelkontakte. Mit diesen TAMR-Kontakten ist es möglich die Magnetisierung lokal in einer Grössenordnung von 100 nm zu detektieren. Sub-micron TAMR-Messungen und anisotrope Magnetowiderstandmessungen (AMR) an sub-millimeter Gebieten zeigen, dass das Verhalten von makrokopischen (Ga,Mn)As nicht das eines Makrospins ist, sondern ein Ensembledurchschnitt von vielen fast identischen Makrospins. Dieses Ergebnis ist mit der makroskopischen Beschreibung der lokalen magnetischen Aniotropien konform.

Ein rein elektrisch kontrollierbares Read-Write Speicherelement aus dem ferromagnetischen Halbleiter (Ga,Mn)As wird in Kapitel 8 gezeigt. Das Element besteht aus vier 200 nm breiten Streifen, die mit einer kreisförmigen zentralen Disc verbunden sind. Der erste Teil des Kapitels beschreibt die einzelnen Lithographieschritte zur Herstellung des Elements. Zum Auslesen der Magnetisierungsrichtung der zentralen Disc mit einem Durchmesser von 650 nm verwenden wir einen miniaturisierten TAMR-Kontakt. Die 200 nm breiten Streifen dienen als Quelle eines spinpolarisierten Stromes in die zentrale Disc. Das Injezieren von polarisierten Löchern mit einem Spin-Drehimpuls in eine magnetische Region verändert die Magnetisierung der Region durch p-d Austauschwechselwirkung zwischen lokalisierten Mn-Spins und den Löchern [Yama 04]. Die Magnetisierung der zentralen Disc kann rein elektrisch kontrolliert werden and als Bit eines Logikelementes verwendet werden. In Kapitel 7 untersuchen wir den Domänenwiderstand in (Ga,Mn)As. Am Übergang von den Streifen zur zentralen Disc ist es möglich 90°- und 180°-Domänenwände zu erzeugen und deren Widerstand zu messen.

Die Ergebnisse von Kapitel 5 bis 7, kombiniert mit dem bereits existierenden Ergebnis-

sen einer ultrakompakten (Ga,Mn)As-basierenden Speicherzelle von Ref. [Papp 07c], sind die Schlüsselelemente die man zur Realisierung eines programmierbaren Logikelements benötigt. Die Arbeit von Referenz [Papp 07c] nutzt Lithographie induzierte Deformationsrelaxation [Hump 07], um eine Struktur zu erzeugen, die aus zwei senkrechten Streifen besteht und durch eine Verengung verbunden sind. Der Widerstand dieser Verengung ist von der relativen Magnetisierungsorientierung der beiden Streifen abhängig.

Das programmierbare Logikelement besteht aus zwei zentralen Discs, die mittels einer schmalen Verengung verbunden sind. Die Magnetisierung der beiden zentralen Discs dienen als Eingänge und die Verengung als Ausgang während der Logikoperation. Das Konzept wird am Ende des sechsten Kapitels eingefürt und als Beispiel für eine Logikoperation wird ein XOR-Gate präsentiert. Die Funktionalität des hier gezeigten programmierbaren Logikschemas kann Problemlos auf ein multifunktionales Element erweitert werden. Diese Geometrie kann abhängig von der Anzahl der Eingänge und der gewählten Adressierung für verschiedene Rechenelemente genutzt werden.

Die Realisierung eines programmierbaren Logikelements ist in Kapitel 8 gezeigt. Der Widerstand der Verengung hängt von der relativen Magnetisierungsrichtung der beiden zentralen Discs ab und wird als Ausgang während der Logikoperation verwendet. Im Gegensatz zu Referenz [Papp 07c], indem die einzelnen über die Verengung verbundenen magnetischen Elemente jeweils nur zwei nicht-flüchtige magnetische Zustände besitzen, hat jede zentrale Disc in unserem Schema vier nicht-flüchtige magnetische Zustände. Das Verändern der Magnetisierungsrichtung einer zentralen Disc durch einen elektrischen Strom kann durch den jeweiligen TAMR-Kontakt und durch die Widerstandänderung der Verengung gemessen werden. Der Widerstands-Fingerabdruck (resistance polar plot) der Verengung zeigt die verschiedenen relativen Magnetisierungszutände der zentralen Discs.

Das hier präsentierte Konzept dient als reines Halbleiter und rein-elektrisches Logikelement. Es kombiniert eine Speicherzelle und Datenverarbeitung in einem neuartigen monolithischen Bauelement.

Summary

The discovery of the giant magneto resistance effect (GMR) by P. Grünberg and A. Fert [Bina 89, Baib 88] in 1980 was the breakthrough which launched the spintronics research field and has revolutionized the information storage industry. By 1997, IBM introduced GMR based read-heads in conventional hard drives and it as well as derivative technologies currently dominate the field. Faced with the ever increasing challenge of fulfilling Moore's law, and the stark reality, that with continued miniaturization and incremental breakthroughs, fundamental limits such as atomic structure size will be reached as early as 2020, the semiconductor industry is aggressively looking for a disruptive technology to take it beyond CMOS [Inte 11]. One major drawback in the current architecture are the interconnects carrying information between semiconductor based data processing units and the ferromagnetic metal based memory elements and are significantly responsible for heat generation. Combining memory elements and information processing in a single monolithic paradigm generates a scheme without the need of such interconnects. Spintronics is now aiming for an all-semiconductor, all-electrical memory element. In this theses we show the realization of such a device made from the ferromagnetic semiconductor (Ga,Mn)As (Gallium-Manganese-Arsenide).

In chapter 2 we introduce (Ga,Mn)As which is currently the best controlled ferromagnetic semiconductor. The material serves as an ideal testbed for transport studies in systems where the density of states and the magnetic anisotropies are connected via a strong spin-orbit-coupling. Its rich magnetic anisotropies are dependent on several parameters such as MBE growth conditions, substrate lattice constant and doping concentration. Here we present transport studies to characterize the material and its different magnetic anisotropies.

While the main topic of this theses is a programmable logic device we make an aside in chapter 3 to show a ferromagnetic metal/semiconductor hybrid system. A practical obstacle of (Ga,Mn)As to its device implementation is its rather low Curie temperature. One promising approach to overcome this obstacle is the use of hybrid ferromagnetic (FM) metal / FM semiconductor heterostructures where the metallic magnetism is used to enhance the magnetic properties of the semiconductor (SC). These hybrid systems could be a path to increase and stabilize T_C. The nature of the magnetic coupling be-

tween the metal and the SC will of course be crucial to eventual device operations. In particular we find an independent magnetization behavior of the individual layer without any non-magnetic spacer layer. The independence of the two magnetic layers is confirmed by transport observations, and direct magnetization measurements using SQUID (superconducting quantum interference device). We also make use of this functionality to demonstrate a two layer hybrid multi-valued memory element with four non-volatile configurations at zero magnetic field.

For the realization of a programmable logic device, or indeed any nanoscale device, we need a reliable method to probe the magnetization direction of local domains. For this purpose we extend investigations on the previously discovered tunneling anisotropic magneto resistance effect (TAMR) [Goul 04] by scaling the pillar size from 100 µm down to 260 nm. We start in chapter 4 with a theoretical description of the TAMR effect and show experimental data of miniaturized pillars in chapter 5. With such small TAMR probes we are able to locally sense the magnetization on the 100 nm scale. Sub-micron TAMR and anisotropic magneto resistance (AMR) measurements of sub-millimeter areas show that the behavior of macroscopic (Ga,Mn)As regions is not that of a true macrospin, but rather an ensemble average of the behavior of many nearly identical macrospins. This shows that the magnetic anisotropies of the local regions are consistent with the behavior extracted from macroscopic characterization.

A fully electrically controllable read-write memory device out the ferromagnetic semiconductor (Ga,Mn)As is presented in chapter 6. The structure consists of four nanobars which are connected to a circular center region. The first part of the chapter describes the lithography realization of the device. We make use of the sub-micron TAMR probes to read-out the magnetization state of a 650 nm central disk. Four 200 nm wide nanobars are connected to the central disk and serve as source and drain of a spin-polarized current. With the spin-polarized current we are able to switch the magnetization of the central disk by means of current induced switching. Injecting polarized holes with a spin angular momentum into a magnetic region changes the magnetization direction of the region due to the p-d exchange interaction between localized Mn spins and itinerant holes [Yama 04]. The magnetization of the central disk can be controlled fully electrically and it can serve as one bit memory element as part of a logic device. In chapter 7 we discuss the domain wall resistance in (Ga,Mn)As. At the transition from nanobars to central disk we are able to generate 90° and 180° domain walls and measure their resistance.

The results presented from chapter 5 to 7 combined with the preexisting ultracompact (Ga,Mn)As-based memory cell of ref. [Papp 07b] are the building blocks needed to realize a fully functioning programmable logic device. The work of ref. [Papp 07b] makes use of lithographically engineered strain relaxation [Hump 07] to produce a structure comprised of two nanobars with mutually orthogonal uniaxial easy axes, connected by a narrow

constriction. Measurements showed that the resistance of the constriction depends on the relative orientation of the magnetization in the two bars.

The programmable logic device consists of two central disks connected by a small constriction. The magnetization of the two central disks are used as the input bits and the constriction serves as the output during the logic operation. The concept is introduced in the end of chapter 6 and as an example for a logic operation an XOR gate is presented. The functionality of the programmable logic scheme presented here can be straightforwardly extended to produce multipurpose functional elements, where the given geometry can be used as various different computational elements depending on the number of input bits and the chosen electrical addressing.

The realization of such a programmable logic device is shown in chapter 8, where we see that the constriction indeed can serve as a output of the logic operation because its resistance is dependent on the relative magnetization state of both disks. Contrary to ref. [Papp 07b], where the individual magnetic elements connected to the constriction only have two non-volatile magnetic states, each disk in our scheme connected to the constriction has four non-volatile magnetic states. Switching the magnetization of a central disk with an electrical current does not only change the TAMR read-out of the respective disk, it also changes the resistance of the constriction. The resistance polar plot of the constriction maps the relative magnetization states of the individual disks.

The presented device design serves as an all-electrical, all-semiconductor logic element. It combines a memory cell and data processing in a single monolithic paradigm.

Chapter 1

Introduction

Spintronics (Spin transport electronics or Spin based electronics) makes use of the electron (hole) spin to manipulate the flow of electrons (holes) and thus requires materials where the spin and charge degree of freedom of carriers are strongly coupled [Jung 06]. One of these materials is the ferromagnetic semiconductor (Ga,Mn)As. Since its discovery 1996 by Ohno et al. [Ohno 96] many technological issues have been solved and the progress in device applications went rapidly. However, a single device which is able to write, store and retrieve information is still lacking. In this chapter we briefly introduce pre-existing results constituting the basic ingredients for realizing such a device out of (Ga,Mn)As.

One of the first experiments performed with a local anisotropy control of different magnetic (Ga,Mn)As regions is shown in [Rust 03]. The authors define three lateral bars connected with a small constriction, fig. 1.1. The left and right bar have identical dimensions whereas the smaller central region is $\sim$100 nm wide and $\sim$350 nm long. Due to different dimensions the bars have different anisotropies and thus different coercive fields. By sweeping a magnetic field along the bars the magnetization of the inner and outer regions is either parallel or anti parallel. Dependent on its width, the constriction either serves as a pinning center for a domain wall or acts as a tunnel barrier. If it the constriction is rather narrow the electrical response due to the magnetization reversal process of the individual magnetic elements can lead to an resistance effect as high as 1000%.

In a miniaturized form the TAMR effect discovered by Gould et al. [Goul 07b] in 2007 can serve as a magnetization read-out tool. The structure consists of a (Ga,Mn)As layer and a AlOx tunnel barrier covered by Ti/Au. The TAMR response with respect to the magnetization direction of the material is similar to the anisotropic magneto resistance effect (AMR) and stems from spin-orbit coupling and thus reflects the density of state of the ferromagnetic layer. TAMR measurements can be performed at low bias voltages and thus have a low operating current density through the barrier. These condition are ideal for a magnetic read-out procedure having a non-destructive current which does not perturb the magnetic state. The amplitude of the effect is sufficiently large to achieve a

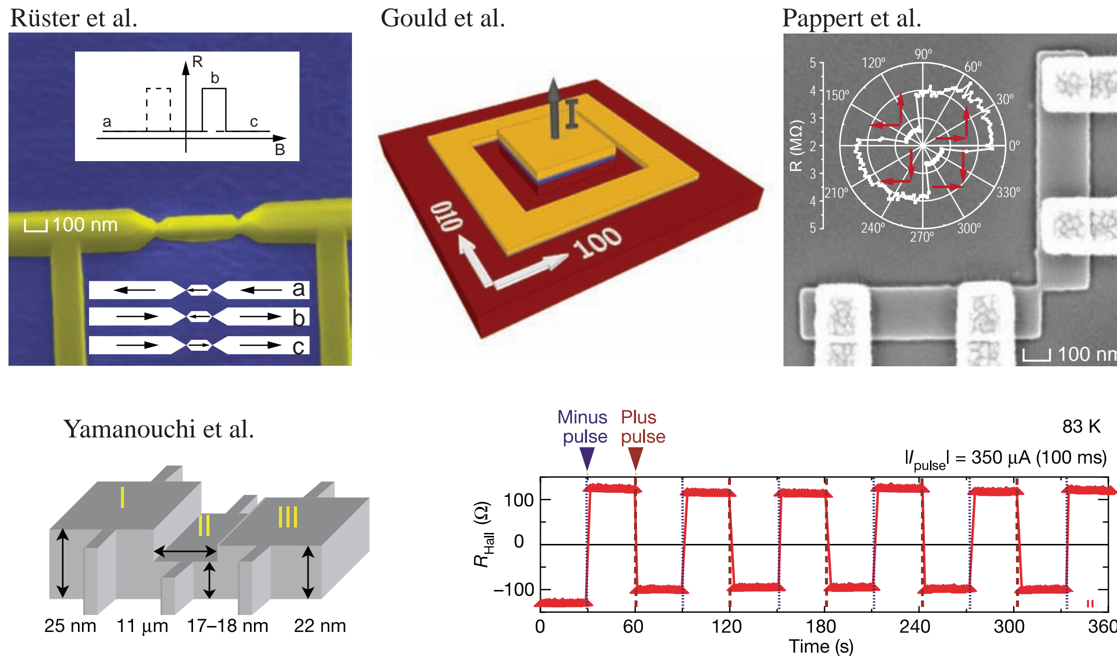

Fig. 1.1: Previous work on spintronic device application. Top panel from left to right: Rüster et al. [Rust 03]: The relative magnetization states for the different magnetic regions results in different resistances. The MR measurement is sketched in the inset. Gould et al. [Goul 07b]: First demonstration of TAMR on a 100 × 100 µm^2 structure including a ring as a backside contact. The device only includes one ferromagnetic layer. Pappert et al. [Papp 07c]: Two nanobars coupled with a small constriction realizes a non-volatile memory element out of (Ga,Mn)As. Bottom panel: Yamanouchi et al. [Yama 04]: First demonstration of current induced magnetization on gallium manganese arsenide. Figures taken from the respective publications.

clear high/low resistance ratio.

A further milestone in (Ga,Mn)As device applications is the work of K. Pappert et al. [Papp 07c], fig. 1.1. Here two 200 nm wide nanobars are coupled via a small constriction forming a L-shape and the long axis of the two nanobars are orthogonal. The constriction is in the non-linear transport regime and due to the coupling of the dipolar fields of the two nanobars the constriction resistance depends on the relative magnetization configuration of the nanobars. This device is the first realization of a non-volatile memory element out of (Ga,Mn)As. For changing the magnetic configuration of the nanobars a magnetic field is necessary. This experiment in combination with a current-induced domain wall displacement demonstrated in [Yama 04] leads to a multi-functional memory element.

The authors of [Yama 04] show current-induced switching in (Ga,Mn)As for the first time. Their material is tensile strained and thus has magnetic easy axis out of plane and the in-plane directions are hard magnetic directions. The experiment is performed on a Hall bar which consists of three regions with different (Ga,Mn)As layer thickness, fig. 1.1.

Two hall contacts are connected to each magnetic region to read-out the magnetization direction. The central region has the lowest coercive field and can be manipulated by a spin-polarized current injected from the outer magnetic regions. The outer magnetic regions are magnetized in an antiparallel configuration. Dependent on current direction the central magnetization aligns parallel to the region where the spin polarized carriers are injected. Due to the p-d exchange interaction between carriers and localized Mn atoms the magnetization of the central regions will align parallel to the respective magnetization direction.

In this thesis we show the realization of a fully electrical read-write device which combines all ingredients starting from local anisotropic strain relaxation, local read-out ability of the magnetic state with a miniaturized TAMR contact and a current-induced switching mechanism to write the magnetic state with electrical means. Chapter 2 introduces the ferromagnetic semiconductor (Ga,Mn)As and the techniques we use to map the different anisotropy components of the material. The independent magnetization behavior of a ferromagnetic metal/semiconductor hybrid system is discussed in chapter 3 as a side note to the main topic of the thesis. Chapter 4 and 5 deals with the tunneling anisotropic magneto resistance effect and shows miniaturized tunneling contacts. Measurements performed with these submicron TAMR probes are compared to longitudinal anisotropic magneto resistance measurements. In chapter 6 we present the fully electrical read-write device out of (Ga,Mn)As. Chapter 7 uses the read-write device geometry to determine the domain wall resistance in gallium-manganese-arsenide. The following chapter 8 combines two of the read-write devices to a programmable logic element.

Chapter 2

(Ga,Mn)As, a Ferromagnetic Semiconductor

This Chapter introduces the ferromagnetic semiconductor gallium manganese arsenide, (Ga,Mn)As. The first part concentrates on the magnetic properties of the material. The second part summarizes the known transport properties and presents an extensive comparison of anisotropies in MBE grown (Ga,Mn)As material performed as a part of this work [Goul 08].

2.1 Ferromagnetism in (Ga,Mn)As

GaAs is a III-V semiconductor with a zinc blende structure and a bandgap of $E_g \sim 1.5$ eV at low temperatures. Mn as a dopant substitutes a Ga and acts as a shallow acceptor and is in a Mn^{2+} configuration. For low doping concentrations (<<1%) the Mn is isolated and has an impurity binding energy of $E_a^0 \sim 113$ meV [Linn 97] with a localized hole and shows insulating character at low temperatures. As the Mn concentration is increased, the Mn-doped GaAs exhibits a phase transition to a state in which the Mn impurity levels sufficiently overlap and form a "metallic" ground state, where the states at the Fermi level are not bound to a single or a group of Mn atoms. The holes in the metallic state are delocalized across the system. The critical metal-insulator transition density occurs at around 1% Mn concentration. [Jung 07]

Furthermore the substitutional Mn impurity in the GaAs host material has a localized magnetic moment with $s = 5/2$ according to Hund's rules. Itinerant holes and the localized Mn moments couple anitferromagnetically and thus neighboring Mn atoms couple ferromagnetically due to the extension of the holes wave function. A Zener double-exchange magnetic interaction among itinerant holes and Mn moments create the hole-mediated ferromagnetism in (Ga,Mn)As [Diet 00]. For Mn concentrations between 2% and 9% the holes propagate quasifreely through the system [Goul 07a]. Instead of a Mn atom replacing a Ga (substitutional), the manganese impurity can intertitially incorporate into

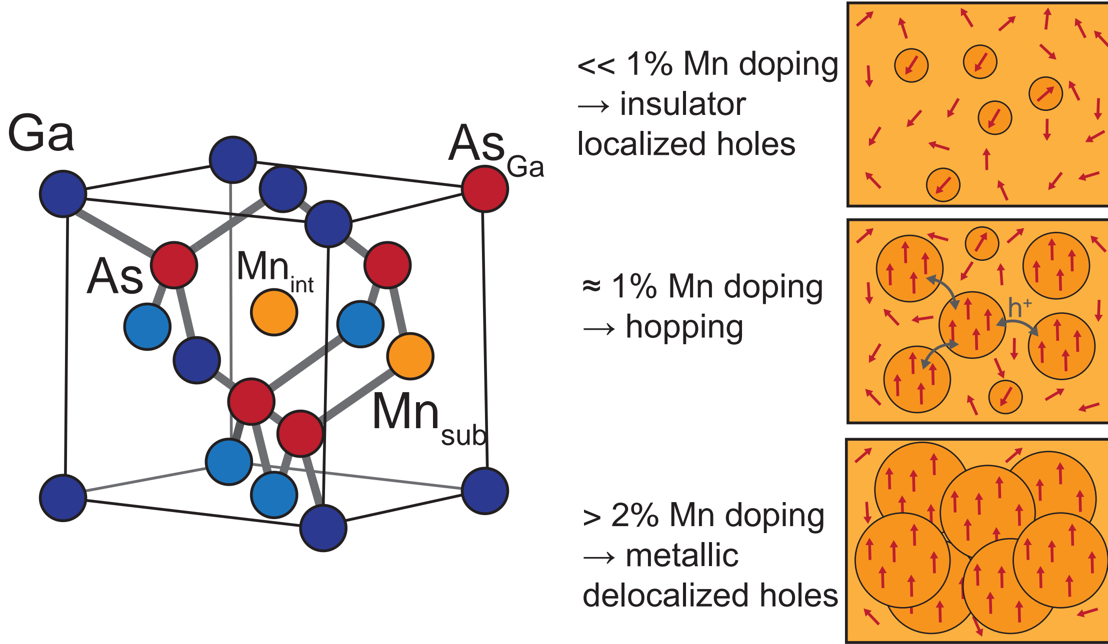

Fig. 2.1: Left: (Ga,Mn)As zinc blende lattice with substitutional and interstitial Mn atoms. Right top to bottom: simplified model of ferromagnetism in (Ga,Mn)As dependent on doping concentration. Mn concentration lower 1% the material is insulating at low T and has localized holes bound to the Mn impurity. At around 1% the material is in the hopping regime. Above 2% Mn doping the (Ga,Mn)As is ferromagnetic due to the coupling of the Mn atoms to the itinerant holes.

the GaAs lattice. The intertitial Mn have double donor character and compensate holes comming from substitutional Mn impurities. The first experimental observation of ferromagnetic (Ga,Mn)As was seen by [Ohno 96, Ohno 98] and a theoretical description of (Ga,Mn)as is the p-d mean field Zener model by [Diet 01, Abol 01].

Typically (Ga,Mn)As is grown epitaxially on a GaAs substrate or on a strain-relaxed (In,Ga)As buffer layer and due to the lattice mismatch, the cubic crystal symmetry is reduced and the material is either compressively [Shen 97] or tensile strained, respectively. Substitution of phosphor on the group V sites during growth results in a (Ga,Mn)(As,P) layer, which is also tensile strained without the requirement of a strain-relaxed buffer [Rush 08, Lema 08]. Compressively strained (Ga,Mn)As layers have an in-plane anisotropy whereas tensile strained layers have an easy axes perpendicular to plane. Due to its low Curie temperature (our samples usually have a T_C of ∼60 K to ∼70 K as grown) all measurements in the ferromagnetic phase are carried out in a magnet cryostat at low temperatures. Up to now the highest T_C with ∼190 K is observed in post growth annealed samples [Chen 09, Olej 09]. The lattice mismatch and the different thermal expansion coefficients of substrate and (Ga,Mn)As layer makes it challenging to achieve strain free (Ga,Mn)As layers at low temperatures. The ability to release the growth induced strain in (Ga,Mn)As layers are shown in [Greu 11]. Here the (Ga,Mn)As layer is lifted off the

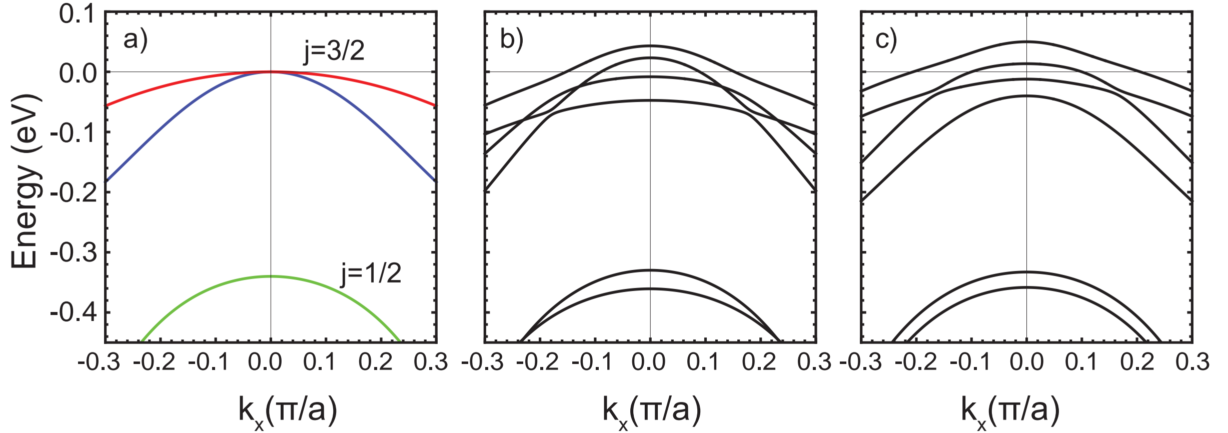

Fig. 2.2: a) Bandstructure of GaAs with double degenerate heavy, light and split-off band calculated with the Kohn-Luttinger Hamiltonian. Energy bands of (Ga,Mn)As along the k_x direction with magnetization parallel x- (b) and z- direction (c). The total Hamiltonian for band structure calculations in (Ga,Mn)As consists of $H_{KL}+H_{BS}+H_{pd}$

substrate and deposited back onto various carrier materials. All (Ga,Mn)As material used in this work is compressively strained and has a smaller lattice constant in plane compared to the growth direction.

The GaAs valence band picture is used as a starting point for calculating the (Ga,Mn)As band structure. The valence band wave functions in a zinc blende type semiconductor as GaAs can be derived from k.p perturbation theory and symmetry considerations. Symmetry considerations show that the wave functions of the valence band have p-like character [Yu 99]. Including heavy hole (HH), light hole (LH) and split off band leads to a 6×6 matrix, which is known as the Kohn-Luttinger Hamiltonian H_{KL} [Abol 01]. Fig. 2.2a shows the valence band of GaAs at the Γ-point. All three bands are double degenerate and the effective masses are $m^*_{HH} = 0.5m_e$, $m^*_{LH} = 0.08m_e$ and $m^*_{SO} = 0.15m_e$. The characteristic GaAs parameters for the calculations are the spin-orbit splitting $\Delta_{SO} = 0.34$ eV and three phenomenological Kohn-Luttinger parameters $\gamma_1 = 6.85$, $\gamma_2 = 2.1$, $\gamma_3 = 2.9$ [Abol 01].

The compressive strain influences the band structure and is considered with a biaxial strain matrix H_{BS}. The magnetic interaction between valence band holes with p-like character and Mn-3d states is treated in a mean-field model [Diet 01]. An effective field from the localized moments of the Mn 3d-states interacts with the hole-spin and the p-d hybridization results in a spin-dependent coupling between the holes and Mn ions, $H_{pd} = -\beta N_0 \mathbf{s} \times \mathbf{S}$. β accounts for the p-d exchange integral and N_0 is the concentration of the cation sites [Diet 01]. The quantity of $N_0\beta \sim -1$ eV is optically accessible and gives the value by which the energy of hole levels are modified due to the exchange interaction. The p-d exchange H_{pd} and the biaxial strain matrix H_{BS} can be found in ref. [Diet 01]. The total Hamiltonian for calculating the band structure of ferromagnetic (Ga,Mn)As is

the sum of

$$H = H_{KL} + H_{BS} + H_{pd}. \tag{2.1}$$

Figures 2.2b and c show the energy bands $E_n(\mathbf{k})$ of (Ga,Mn)As along k_x with a magnetization pointing along x- and z-direction, respectively. The double degenerate HH, LH and SO band existing in GaAs are now split due to the influence of H_{pd} and H_{BS}. As can be seen from 2.2b and c the energy bands $E_n(\mathbf{k})$ of (Ga,Mn)As change with magnetization direction. The Fermi energy E_F in 4% (Ga,Mn)As material is roughly 100 meV and lies somewhere around the top of the fourth band. The density of states $D(E)$ is explicitly connected to the energy band via

$$D_n(E) = \int_{E_n(\mathbf{k})=const.} \frac{dS_E}{4\pi^3} \frac{1}{|\nabla E_n(\mathbf{k})|}, \tag{2.2}$$

where dS_E is an element of the energy surface [Ashc 76] of the n-th band. Consequently, the density of states $D(E)$ of (Ga,Mn)As depends also on magnetization direction.

2.2 Magnetic Anisotropies in (Ga,Mn)As

If the magnetization of a magnetic material has one or more energetically preferential directions, the material has magnetic anisotropies. The system minimizes its energy by aligning its magnetization M along these directions. Several causes, such as strain, shape and exchange anisotropy can account for the direction dependence. The most important one for (Ga,Mn)As is the magneto crystalline anisotropy, caused by spin-orbit coupling through the anisotropy of the carrier-mediated exchange interaction [Diet 01]. Due to this exchange interaction, the hole energies are different for different magnetization directions. Figure 2.2 in section 2.1 shows that the band structure of (Ga,Mn)As depends on the direction of magnetization. Minimizing the total hole energy reveals the directions of easy magnetization. Axes where the anisotropy energy shows a local minima are magnetic easy axes and local maxima are magnetic hard axes. Without an external magnetic field, a magnetic system minimizes its energy with the magnetization parallel to a magnetic easy axis.

(Ga,Mn)As shows a rich magnetic anisotropy and the primary anisotropy component depends on the substrate lattice constant, temperature and hole concentration. All (Ga,Mn)As material used in this work is compressively strained and is epitaxially grown by L. Ebel. A compressively strained (Ga,Mn)As layer with 3% to 6% Mn shows a magnetic hard axis out of plane and a biaxial magnetic easy axes in-plane at 4.2 K. The two

magnetic easy axes are parallel to the (Ga,Mn)As [100] and [010] crystal directions and the magnetic properties of an unpatterned (Ga,Mn)As layer at 4.2 K are dominated by these two magneto crystalline easy axes. A more detailed analysis of the material uncovers two weaker uniaxial second anisotropy components along [$\bar{1}$10] and [010] crystal directions. Expression 2.3 is a phenomenological description of the anisotropy energy and includes all three anisotropy components [Papp 07a]:

$$E = \frac{K_{cryst}}{4} sin^2(2\vartheta) + K_{uni[\bar{1}10]} sin^2(\vartheta - 135^{\cdot}) + K_{uni[010]} sin^2(\vartheta - 90^{\cdot}) - MHcos(\vartheta - \varphi), \quad (2.3)$$

where ϑ denotes the angle between magnetization and [100] crystal axis and φ is the angle between an applied magnetic field and [100]. The first term on the right hand side gives the biaxial anisotropy along the [100] and [010] crystal directions. At 4.2 K $K_{cryst} \approx 3000 J/m^3$, which is equivalent to an anisotropy field of $H_a \sim 120$ mT ($\mu_0 M_s \sim 50$ mT). The conversion from an anisotropy constant K to an anisotropy field is given by:

$$H_a = \frac{2K}{M} \quad (2.4)$$

The second term in equation 2.3 accounts for a much weaker uniaxial anisotropy term along a [$\bar{1}$10] crystal direction [Sawi 04]. The third term stands for a small uniaxial anisotropy parallel to the [010] crystal direction [Goul 04]. This anisotropy component breaks the symmetry of the biaxial easy axes and becomes important for explaining the tunneling anisotropic magneto resistance (TAMR) effect. The origin of the two uniaxial terms is not clear up to now. All three anisotropy constants K_{cryst}, $K_{uni[\bar{1}10]}$ and $K_{uni[010]}$ are temperature dependent [Goul 04, Papp 07d]. $MHcos(\vartheta - \varphi)$ is the Zeeman term and accounts for the energy interaction between an external field and the magnetization of the sample.

Figure 2.3a shows the anisotropy energy potential of the three different contributions (crystalline (red), uniaxial [$\bar{1}$10] (orange), uniaxial [010] (brown)) and the total energy (blue) plotted versus the angle of magnetization ϑ without an applied magnetic field. The minima are magnetic easy directions. The red dot in the minimum along 270° accounts for the magnetization position and depends on the history of the material. Sweeping a magnetic field along the $\varphi = 70°$ direction changes the energy landscape. The response of the magnetization to an applied field is twofold: (1) coherent magnetization rotation (or Stoner-Wohlfarth-Rotation) and (2) a domain wall nucleation and propagation. The Stoner-Wohlfarth-Model [Ston 48] assumes, that the system can be described as a ideal macrospin without allowing a magnetization reversal process due to a domain wall. It takes the anisotropy energy of the system and the interaction between magnetization and an applied magnetic field into account and minimizes the energy. This basically means that the magnetization follows the development of the respective minimum. In the

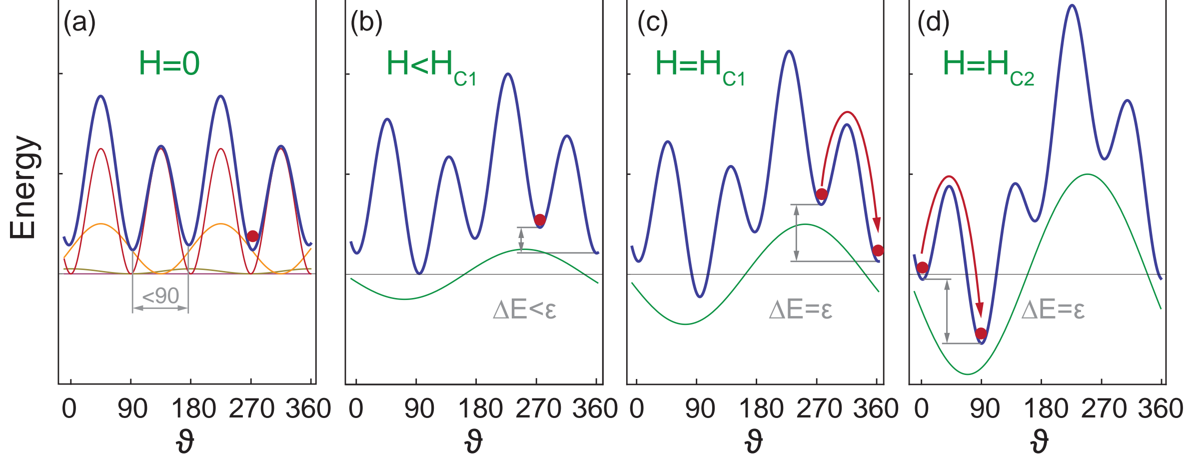

Fig. 2.3: Anisotropy energy landscape versus magnetization angle ϑ. (a) H = 0, blue: sum of the various anisotropy components. Single anisotropy terms: crystalline (red), uniaxial [$\bar{1}$10] (orange), uniaxial [010] (brown). (b,c,d) Sweeping an external magnetic field along the $\varphi = 70°$ direction (green) and development of the anisotropy energy with increasing field. The red dot represents the position of magnetization.

case of fig. 2.3b the magnetization rotates coherently from 270° towards larger angles. The second mechanism is the nucleation and propagation of a domain wall (DW). If the system is able to minimize its energy by a magnetization reversal and the energy difference among the two contributing minima is at least equal to the DW nucleation/propagation energy ϵ, the magnetization changes its direction by a DW reversal process. The result is an instantaneous change of the magnetization direction at H_{c1}. Fig. 2.3c shows the magnetization in a minimum around 270°. The applied field (green) increases the energy difference between the two minima at $\sim 270°$ and $\sim 360°$. As soon as the energy gain is large enough to overcome ϵ, the magnetization direction changes from $\sim 270°$ to $\sim 360°$ (H_{c1}). The magnetization reorientation is thermally activated. Further increasing of the external field yields a second magnetization reorientation process at H_{c2}, see fig. 2.3d. Note that the domain wall nucleation propagation energy empirically depends on $\Delta\vartheta$, which is the angle difference of the contributing minima [Papp 07a].

$$\epsilon_{\Delta\vartheta} = \epsilon_{90°}(1 - cos(\Delta\vartheta)) \qquad (2.5)$$

where $\epsilon_{90°}$ is the energy needed for nucleating and propagating a 90° domain wall. It is now possible to consider two extreme cases for the domain wall nucleation/propagation energy $\epsilon_{90°}$: (1) If $\epsilon_{90°}$ is small the magnetization chooses the global minimum. In the case of fig. 2.3b this results in an immediate magnetization reversal by 180° from $\approx 270°$ to $\approx 90°$. The magnetization in this case reverses at once instead of a double step reversal process as usual in (Ga,Mn)As. (2) If $\epsilon_{90°}$ is large, (e.g. larger as K_{cryst}) it will never be favorable to nucleate and propagate a domain wall. The magnetization remains in its

minimum until this disappears and "slides" into the adjacent minimum. The latter case also accounts for an immediate reorientation of M. In (Ga,Mn)As ϵ_{90° is typically about 5-10% of K_{cryst}.

2.3 Transport Properties of (Ga,Mn)As

In this section we summarize the transport properties of (Ga,Mn)As. All investigations are performed using standard Hall bar geometry, as shown in fig. 2.4a. Magneto resistance measurements are carried out in a magneto cryostat equipped with a vector field magnet capable of producing fields of up to 300 mT in any spatial direction. For the measurement discussed in this section, fields are always applied in the plane of the sample, and the direction of the magnetic field is given by the angle φ relative to the [100] crystal direction.

(Ga,Mn)As exhibits a strongly anisotropic magnetoresistance (AMR), where the resistivity $\rho_\perp$ for current flowing perpendicular to the direction of magnetization is larger than $\rho_{||}$ for current along the magnetization [Baxt 02] (negative AMR). The opposite is true for positive AMR, as usually observed in metallic ferromagnets, because the sign of the AMR effect depends of the ratio between the effective strengths of the non-magnetic and magnetic scattering [Rush 09]. As a result of this anisotropy in the resistivity tensor, the longitudinal resistivity ρ_{xx} is given by [Jan 57, McGu 75]:

$$\rho_{xx} = \rho_\perp - (\rho_\perp - \rho_{||}) \cos^2(\vartheta), \tag{2.6}$$

where ϑ is the angle between the direction of magnetization and the current. Note that there is also a dependence of the resistivity on the angle between the direction of magnetization and the underlying crystal orientation [Rush 07]. This additional term modifies the resistivity value for a given magnetization direction, but does not effect the field position of the magnetization reorientation events, and can thus be neglected for the purpose of the present analysis.

For each sample, we measure the four terminal longitudinal resistance using the lead configuration given in fig. 2.4a by passing a current from the I_+ to the I_- contacts, and measuring the voltage between V_1 and V_2. We scan the magnetic field from -300 mT to +300 mT along a given direction φ, and repeat this procedure for multiple angles. A measurement of such a scan for the case of $\varphi = 70^\circ$ is given in fig. 2.4b, and shows two switching events, labeled H_{c1} and H_{c2} associated with the two sequential 90° domain wall nucleation/propagation events, which accounts for the magnetization reversal in this material [Welp 03]. In order to analyze the data, the positive field half of each of these scans are converted to a sector of a polar plot as shown in fig. 2.4b inset. The two switching events then show up as abrupt color changes, as indicated in the figure. The compilation of all the sectors required for a full revolution produces an anisotropy fingerprint resistance polar plot (RPP) as the one in fig. 2.4d.

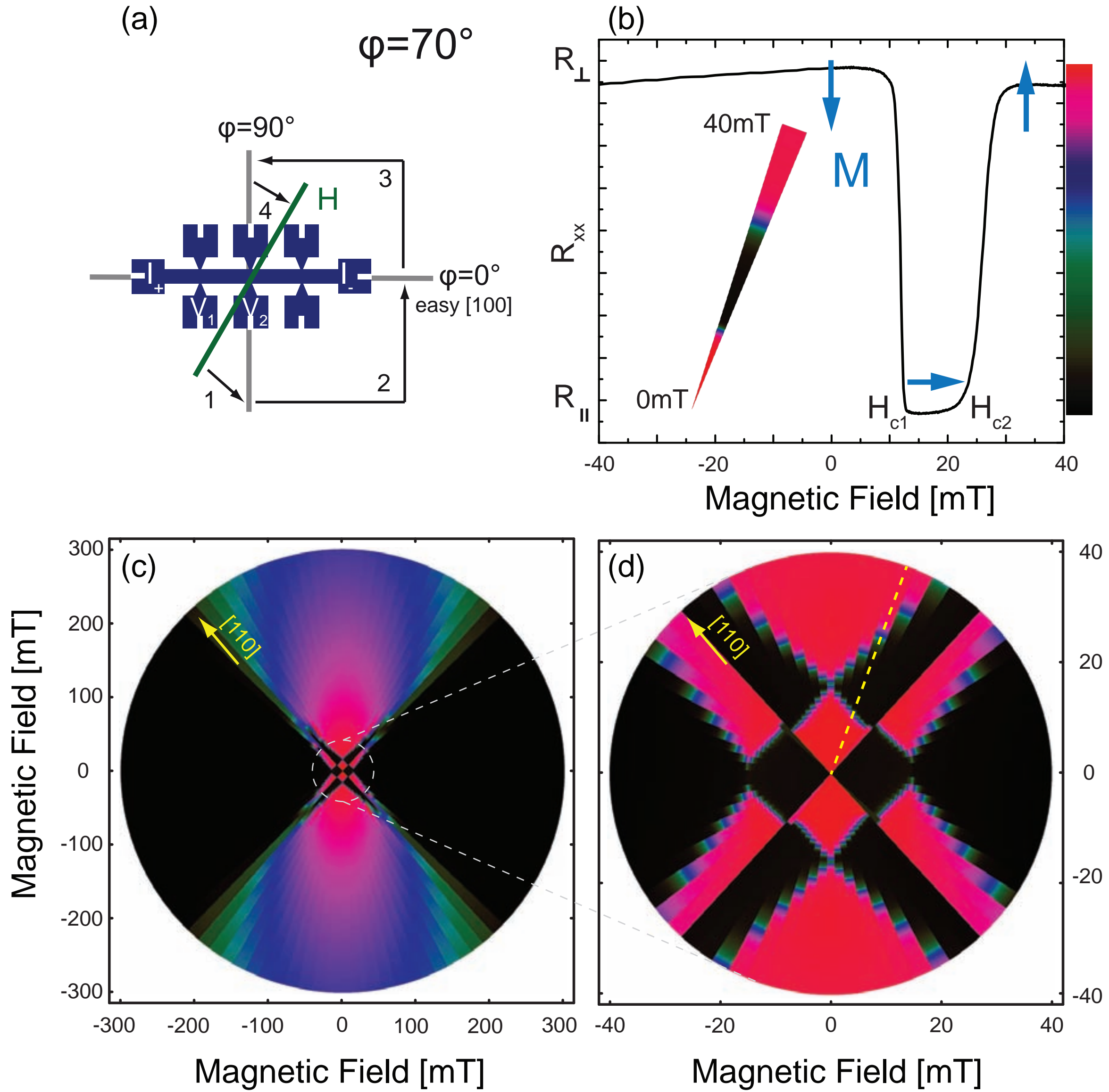

Fig. 2.4: a: Layout of the Hall bar used in the experiments and configuration for the measurements of a magnetoresistance scan along $\varphi = 70°$ (b), showing the two switching events H_{c1} and H_{c2} corresponding to the two subsequent 90° domain wall propagation events. This data is then converted to a sector of a resistance polar plot, see inset of (b). (c) Measurement of a full resistance polar plot comprised of sectors as in inset of (b). (d) measurement of the inner region of the polar plot.

For the purpose of characterizing the various anisotropy terms, the most important part of the data is the innermost region, whose boundaries are formed by the loci of first switching events (H_{c1}). fig. 2.4d shows a zoomed in view of this region for an experimental measurement on a characteristic piece of (Ga,Mn)As.

For the model case of a purely biaxial anisotropy, this inner region would take the form of a perfect square with corners along the easy axis and the length of the half diagonal given by ϵ/M, the domain wall nucleation/propagation energy scales to the volume magnetization (fig. 2.5a). The inclusion of a uniaxial anisotropy bisecting two of the biaxial easy axes moves the resulting easy axes towards the direction of the uniaxial anisotropy [Goen 05] and elongates the square into a rectangle, as schematically depicted in fig. 2.5b. The strength of the uniaxial anisotropy constant in the $[\bar{1}10]$ direction $K_{\bar{1}10}$ relative to the biaxial anisotropy constant K_{cryst} can be extracted from the angle δ, as defined in fig. 2.5b, by which the angle between two easy-axes is modified. The relationship is given by [Papp 07a]:

$$\delta = \arcsin\left(\frac{K_{uni[110]}}{K_{cryst}}\right) \tag{2.7}$$

In practice, because the mixing of the anisotropy terms leads to a rectangle with open corners, it is often more convenient to work with the aspect ratio of the width (W) to the length (L) of the rectangle, instead of the angle δ, which is related to the anisotropy terms as:

$$\frac{K_{uni[110]}}{K_{cryst}} = \cos\left(2\arctan\left(\frac{W}{L}\right)\right) \tag{2.8}$$

If an uniaxial anisotropy is added instead parallel to one of the biaxial easy axes, an asymmetry arises in the energy required to switch between the two biaxial easy axes. Essentially, the energy required to switch towards the easier of the two biaxial easy axis is less than to switch towards the second biaxial. The inner pattern is then comprised of parts of an inner and an outer square, and the difference in the length of their half diagonal is a measure of K_{010} (fig. 2.5c), where K_{010} is the [010] anisotropy constant. Because of deformation of the fingerprint near the corners of the rectangle, which results from mixing of the anisotropy terms, it is often easier to identify the presence of an [010] uniaxial easy axis by looking at the spacing between the sides of the squares (or rectangles in the case that a [110] uniaxial term is also present), as indicated by the yellow line in fig. 2.5c, which of course has a length equal to $\sqrt{2}K_{010}$.

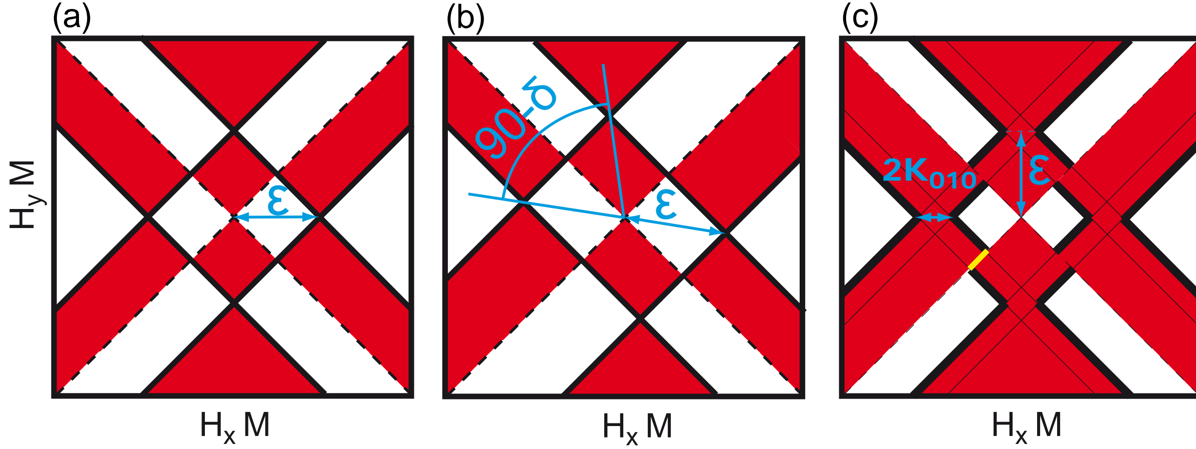

Fig. 2.5: Sketches of the expected shape of the inner region for a) a sample with only a ([100] and [010]) biaxial anisotropy. b) a sample with a biaxial plus a [$\bar{1}$10] uniaxial easy axis, and c) a sample with a biaxial plus a [010] uniaxial easy axis. Note that the axis are in magnetic field units scaled to the volume magnetization M.

2.4 A Comparison of Anisotropies in MBE Grown (Ga,Mn)As Material

All three anisotropy components in (Ga,Mn)As are now generally accepted. The existence of the [010] anisotropy component was controversial for a long time, because, amongst others, the [010] component is symmetry forbidden in the zinc blende crystal structure. In order to resolve this issue and confirm that this is a general property of the material and not a unique characteristic of (Ga,Mn)As wafers grown in Würzburg, we investigate the anisotropies in MBE grown material from different sources. We now present the results of measurements performed on samples patterned from layers grown in various laboratories and thus under varied growth conditions. This study confirms, that the [010] component is not a particularity of (Ga,Mn)As grown in a certain MBE chamber or under particular conditions, but is indeed ubiquitous to the material.

Figure 2.4d shows a fingerprint from a fairly typical layer grown in Würzburg. To illustrate the typical spread that can be expected, we present in fig. 2.6 two additional Würzburg layers with rather pronounced [010] (fig. 2.6a) or [110] (fig. 2.6b) components. In parts c-f of the figure we compare these to fingerprints on layers grown at IMEC, Nottingham, Tohoku, and Notre Dame. Values of the various parameters extracted from all these layers are given in table 2.1. The figure illustrates that not only the amplitude, but also the sign of the two uniaxial components can vary between samples. For the [110] uniaxial, this change in sign can be seen by a 90° rotation of the long axis of the rectangle, whereas the sign of the [010] is determined by whether the quarter of the rectangle with its primary diagonal along [010] is larger or smaller than that with the diagonal along

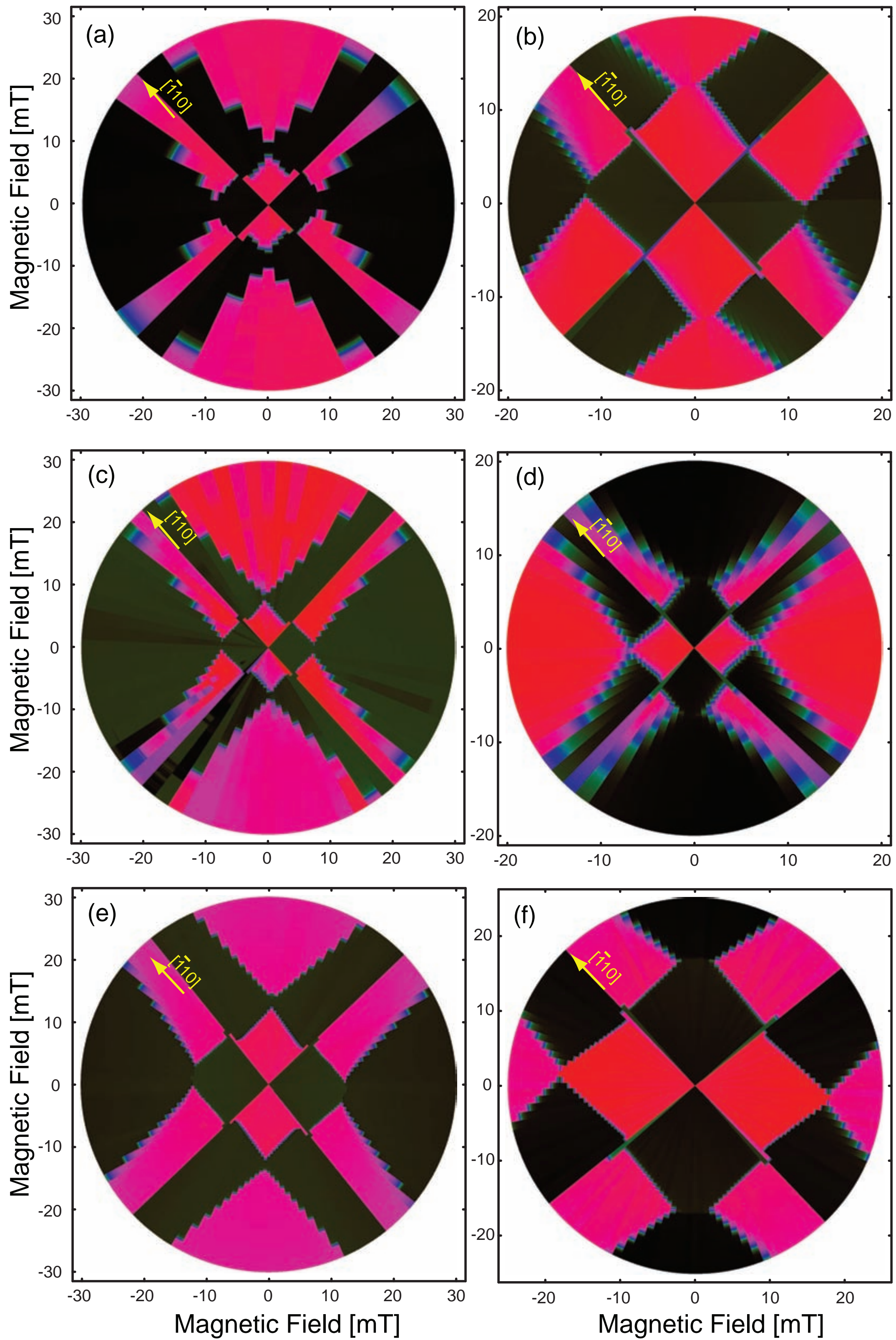

Fig. 2.6: Fingerprints from (Ga,Mn)As layers grown in various laboratories. a) and b) are layers grown in Würzburg with strong [010] and [110] easy axis, respectively. The other fingerprints are from layers grown at c) IMEC, d) Nottingham, e) Tohoku, and f) Notre Dame.

[100]. Note that the sign of the color scale (determining which regions are red and which are black) is determined by the direction of the current flow during the measurement, and is irrelevant to the current investigation.

	$\epsilon/M(mT)$	$K_{110}/K_{cryst}(\%)$	$K_{010}/M(mT)$
Wü. from fig. 2.4d	13	7	0.8
Wü. with large [010]	8.5	7	1.4
Wü. with large [110]	12	21	0.7
IMEC	7.8	11	0.7
Nottingham	7.1	9	0.65
Tohoku	12	4	1.25
Notre-Dame	16	9	0.75

Tab. 2.1: Characterization parameters extracted from the anisotropy fingerprints on various layers.

As is clear from the table, all samples show a significant contribution of both a [110] and [010] uniaxial anisotropy component. The values of the parameters that can be extracted from the fingerprints show variance from sample to sample, and typically fall in the range of some 7 to 18 mT for ϵ/M, 0.6 to 1.5 mT for K_{010}/M, 4 to 20% for the ratio of K_{110}/K_{cryst}. Note that, while the fingerprint technique cannot be used to reliably extract exact values for K_{cryst}, the shape of the curve as the magnetization rotates away from the easy axis towards the external magnetic field at higher fields can be used to estimate the strength of K_{cryst}/M. All samples investigated show a value of approximately 100 mT for this parameter, which means that the values of K_{110}/K_{cryst} quoted in percent in the table are also estimates of K_{110}/M in mT.

While the table clearly shows significant variation from sample to sample, it nevertheless allows the extraction of useful rules of thumb for relative amplitude of the various terms. As a general statement, the ratio of $K_{cryst} : K_{110} : K_{010}$ is of order 100 : 10 : 1, and the domain wall nucleation/propagation energy is of the order of 10% of the biaxial anisotropy constant.

The range of values for K_{010}/M and ϵ/M discussed in this study is a fair representation of (Ga,Mn)As in general. The span of values for the K_{110}/K_{cryst} ratio, which is already in the table larger than the other parameters, is however only a reflection of the subset of samples that we investigated. In general, this ratio can easily be tuned over a much larger range, for example as a function of hole concentration [Sawi 04] or of temperature [Papp 07a]. No systematic distinction is observed between samples from the various sources.

Chapter 3

FM Metal/Semiconductor Hybrid System

Semiconductor (SC) spintronic devices are leading candidates to combine modern magnetic element storage and SC based information processing into a single device paradigm [Awsc 07]. A practical obstacle to their implementation is the rather low Curie temperature. One promising approach to overcome this obstacle is the use of hybrid ferromagnetic (FM) metal / FM semiconductor heterostructures where the metallic magnetism is used to enhance the magnetic properties of the SC. The authors of ref. [Macc 08] report that the manganese within a 2nm thick (Ga,Mn)As region at the interface couples antiferromagnetically to a FM Fe over layer. The nature of the magnetic coupling between the metal and the SC will of course be crucial to eventual device operations. Devices whose functioning is based on the relative magnetization state of two controllable magnetic elements, such as GMR (giant magneto resistance) [Baib 88, Bina 89] based read heads [Thei 03] and TMR (tunnel magneto resistance) [Jull 75] based MRAM [Aker 05] are crucial to the modern information technology industry. So far, all such devices have been comprised of at least three layers: the two magnetic layers and a spacer layer to break the direct coupling between them and allow them to reorientate their relative magnetization. For obvious technological reasons, the removal of the functionally superfluous intermediate layer would be beneficial. In this chapter we show that, unlike the case of two FM metals, the bringing together of a FM metal with a FM SC can allow the layers to remain magnetically independent and thus permit the fabrication of devices without the need of a non magnetic interlayer. We demonstrate a first such device, which because of the strong anisotropies in the FM semiconductor layer has not only two, but up to four stable resistance states in the absence of a magnetic field. Before discussing the hybrid system the magnetization behavior of a single permalloy layer, which we use as the FM metal, will be shown. Parts of the measurements shown in this chapter have already been reported in [Mark 07]. Further measurements on this topic, analysis and interpretation of the data where done during the preparation of this work. Much of what is presented in this chapter has also been published in [Mark 09].

3.1 Permalloy Layers

3.1.1 Exchange Bias

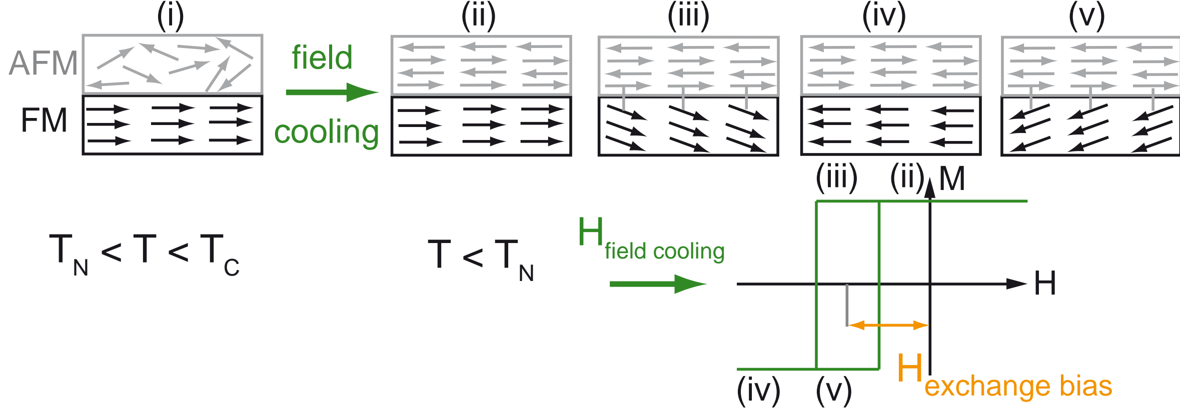

Fig. 3.1: Schematic diagram of the spin configuration of an FM-AFM bilayer at different stages (i)-(v) of an exchange biased hysteresis loop. Figure adapted to [Nogu 99]

When a ferromagnetic and an antiferromagnetic (AFM) layer with a common interface are cooled through the Néel temperature of the AFM (with the condition $T_C > T_N$) an anisotropy (exchange bias) is induced in the FM. Exchange bias is associated with the exchange anisotropy created at the interface between an AFM and FM material [Meik 56, Nogu 99]. When a magnetic field is applied in the temperature range $T_N < T < T_C$, the magnetic moments of the FM line up with the field, while the AFM spins remain random (Fig. 3.1 (i)). Cooling the system below T_N with an applied field, due to interaction at the interface the AFM spins at the interface align ferromagnetically with the FM (assuming ferromagnetic interaction). The net magnetization in the AFM is zero because the other spin planes follow the AFM order (Fig. 3.1 (ii)). Reversing the field the FM spins start to rotate and for a large enough AFM isotropy, the AFM spins remain unchanged (Fig. 3.1 (iii)). Therefore, the interfacial interaction between the FM-AFM spins at the interface, tries to align the FM spins with the AFM spins at the interface and exert a microscopic torque on the FM spins, to keep them in their original position (Fig. 3.1 (iii)). This force at the interface causes only one stable configuration for the FM spins at zero magnetic field. The material system behaves as if there was an extra (internal) biasing field which results in a unidirectional anisotropy. Thus the field needed to reverse the FM layer completely will be larger if it is in contact with an AFM, because an extra field is needed to overcome the microscopic torque. As a result of the internal biasing field the hysteresis loop is no longer symmetric around the origin. The hysteresis loop is shifted to the opposite direction of the cooling field and the loop shift is generally known as exchange bias (Fig. 3.1). Contrary to a uniaxial anisotropy with two easy directions the AFM-FM system has only one easy direction which is denoted as unidirectional anisotropy. [Nogu 99]

AFM layers on ferromagnetic metals are usually created due to surface oxidation. The natural oxide layer of permalloy, which forms by exposing the layer to air, shows a rather complicated behavior and the anisotropy is affected by magnetic field sweeps. Whereas a well defined AFM layer exists on top of permalloy when covered with sputtered Magnesium oxide (MgO). Metals, e.g. Ruthenium, can be used to prevent the permalloy layer from oxidation.

3.1.2 Permalloy with Cap Layer

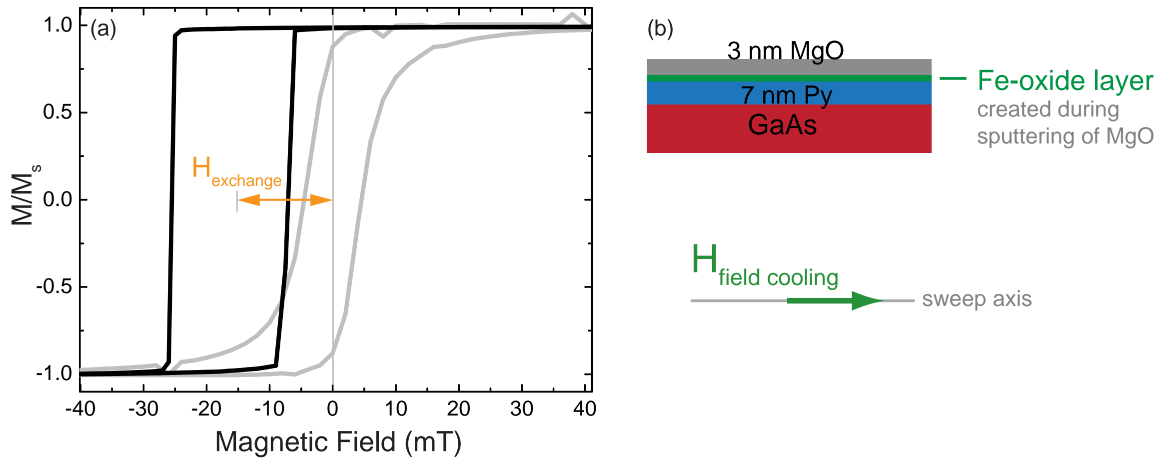

Fig. 3.2: SQUID measurement of a 7 nm Py and 3 nm MgO on GaAs (black). The hysteresis loop is shifted with respect to the origin due to the creation of an AFM layer during the MgO sputtering process. Reference measurement on a 7 nm Py layer covered with 10 nm Ruthenium (gray).

For an initial characterization of the magnetization behavior we cover the permalloy with a 3 nm MgO layer. The thin film stack is magnetron sputtered on GaAs substrate in a vacuum system with a base pressure of 1×10^{-8} mbar. The 7 nm permalloy layer is deposited using dc magnetron sputtering in Ar (5×10^{-3} mbar) from an alloy target ($Ni_{80}Fe_{20}$) and for MgO we use rf sputtering of a stoichiometric target in Ar (1×10^{-3} mbar). We find that sputtering MgO on Py forms a well defined uniform AFM layer. The AFM layer of the Py-MgO system is formed throughout the rf process by oxygen ions released by the sputtering of the MgO target [Read 07]. This layer couples ferromagnetically to the Py film. Our AFM layer most plausible consists of FeO and $Fe_xNi_{1-x}O$, which is the AFM layer obtained from oxidation of $Ni_{80}Fe_{20}$ [Nogu 99]. The Néel and the blocking temperature of $Fe_xNi_{1-x}O$ is between 200-520 K and 40-200 K, respectively. As pointed out by [Hage 67] these characteristic temperatures might be reduced for thin layers, making it impossible to use these as an exact identifier, but the rough agreement in temperature ranges is nevertheless rather convincing. The Néel temperature of NiO is

520K and the blocking temperature of NiO is between 450-500 K. Since we can set the exchange bias direction by warming up the sample to 150 K and field cool with 300 mT NiO seems to be an unlikely canditate. Cooling the Py/MgO system from above its Néel temperature to 4.2 K in an applied magnetic field the exchange bias coupling induces a stable unidirectional anisotropy in the Py film which is not affected by further magnetic field sweeps. Figure 3.2 shows magnetization hysteresis loops measured by SQUID at 4.2 K. A magnetic field of 300 mT is applied during the cooling procedure. The hysteresis loop is shifted with respect to the origin by the strength of the unidirectional anisotropy $H_{exchange} \approx 17mT$ and the direction of the anisotropy depends solely on the alignment of the cooling field. As a reference a hysteresis measurement of a 7 nm permalloy layer covered with a 10 nm Ruthenium layer is shown. The Ruthenium layer prevents the permalloy from oxidation and the hysteresis is symmetric to the origin. Transport and FMR measurements on permalloy layers covered with Ruthenium show a small uniaxial anisotropy at 4.2 K and room temperature (not shown).

A simplified vector model can be used to describe the magnetic behavior of the Py-MgO system below the Néel temperature (fig. 3.3a). The exchange bias induced anisotropy acts as an internal magnetic field and can be modeled as a magnetic field vector with constant amplitude and direction. The unidirectional easy axes can be aligned by applying a 300 mT field along the preferred direction and cooling the system through its Néel temperature. The unidirectional anisotropy is constant within a cooling cycle. It can be changed by warming the system above the Néel temperature and cooling it down with applied field in a different direction. For an intuitive picture we consider the unidirectional anisotropy and the external magnetic field. Figure 3.3a shows the vector addition, where H_{3D} is the external and $H_{exchange}$ the internal magnetic field.

$$\vec{H}_{eff} = \vec{H}_{3D} + \vec{H}_{exchange} \tag{3.1}$$

An analytical expression for the angle ϑ can be deduced to

$$\vartheta = arctan\left(\frac{|\vec{H}_{exchange}| \cdot sin(\alpha) + |\vec{H}_{3D}| \cdot sin(\varphi)}{|\vec{H}_{exchange}| \cdot cos(\alpha) + |\vec{H}_{3D}| \cdot cos(\varphi)}\right) \tag{3.2}$$

where ϑ, α and ϕ are the angles between H_{3D}, $H_{exchange}$ and H_{eff} and current I, respectively.

In this model the magnetization M follows an effective field H_{eff} and ϑ can be calculated analytically as function of $|H_{3D}|$, $|H_{exchange}|$, α and φ. $|H_{exchange}|$ and α are constants within one cooling cycle and are defined by the cooling procedure. Having the angle ϑ the anisotropic magneto resistance can be calculated. Figure 3.3c shows calculated "phiscans" where the amplitude of the external field $|H_{3D}|$ is a constant and the angle φ is

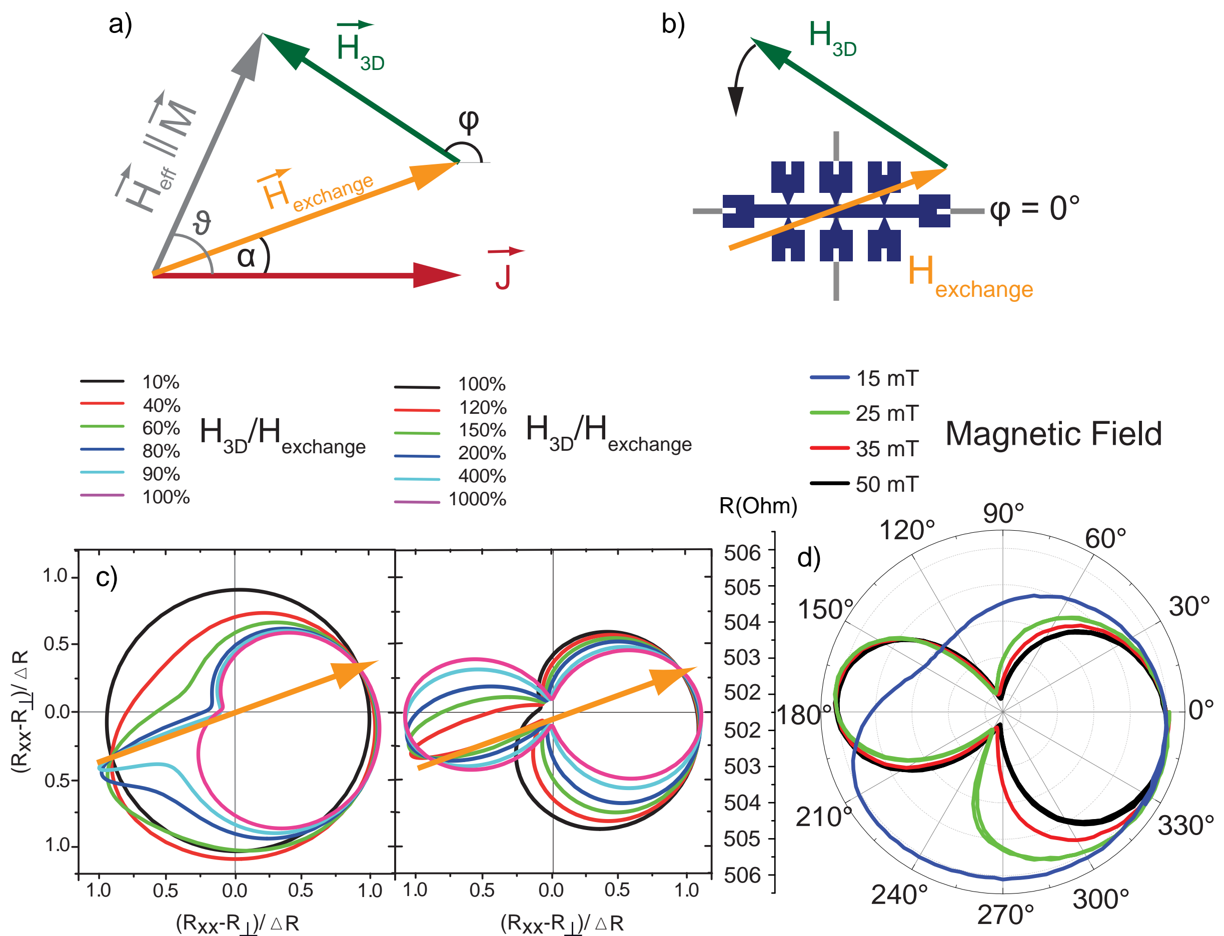

Fig. 3.3: a) Simplified vector model for calculating ϑ analytically. b) Experimental situation after setting the unidirectional anisotropy along 20° with respect to the current direction. c) Phiscan simulations for $H_{3D} < H_{exchange}$ left and $H_{3D} > H_{exchange}$ right. d) Measurements for 15, 25, 35, 50 mT.

varied from 0° to 360°. The exchange bias direction is set along $\alpha = 20°$. Metaphorically speaking, the external field H_{3D} rotates around the tip of the internal exchange field (fig. 3.3b). We can distinguish between two cases. First, the external magnetic field is smaller than the internal exchange field. In this case (fig. 3.3c left) the shape of the phiscans look more circular. In the extreme case ($H_{3D} << H_{exchange}$) of a circle, where the magnetization points along $H_{exchange}$ independent of H_{3D} (fig. 3.3c left black). Second, the external field exceeds the internal exchange field, fig. 3.3c. For $H_{3D} >> H_{exchange}$ the magnetization follows the external field and the AMR resistance shows the typical $cos^2(\vartheta)$ behavior (fig. 3.3c right magenta). Comparing the simulations and the measurements (fig. 3.3d) shows, that the internal exchange field $H_{exchange}$ is between 15 mT and 25 mT, which is in agreement with $H_{exchange}$ extracted from SQUID in fig. 3.2 of 17 mT.

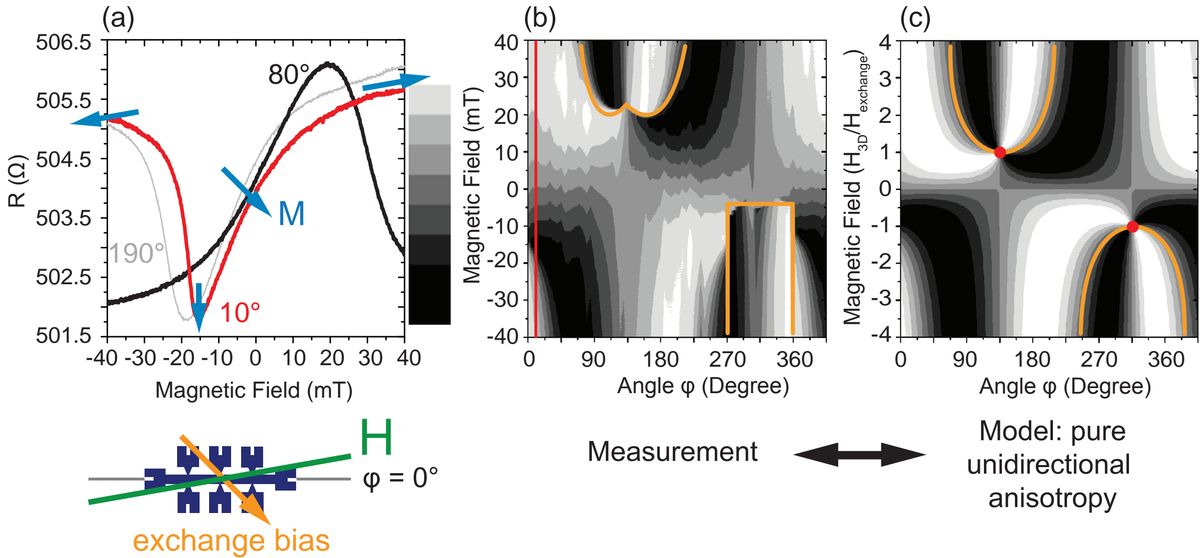

Fig. 3.4: a) MR measurements of a 7 nm permalloy, 3 nm MgO on GaAs for 10° (red), 80° (black) and 190° (gray). b) MR measurements for various direction compiled into a resistance density plot. c) Simplified calculated resistance density plot including the exchange bias anisotropy and the external magnetic field.

Figure 3.4a shows magneto resistance measurements of a Py-MgO system with the exchange bias direction along 315°. Applying a magnetic field of -300 mT along $\varphi = 10°$ the magnetization points parallel to the field in the 190° direction (fig. 3.4 red). The angle ϑ between magnetization and current path, which defines the 0° direction, is 10° and as a result the longitudinal resistance is 97% of its maximum value. When the field is swept to zero the magnetization rotates towards the exchange bias direction. At around -15 mT magnetization and current are perpendicular and the resistance reaches its minimum. At zero field M points along the exchange bias direction, which is true for all field sweep directions. When H_{3D} is large enough it will force the magnetization parallel to 10°. Similar to the RPP the resistances can be color encoded with black as low and white as high resistance (see color code next to fig. 3.4a). Magnetoresistance

measurements for various angles are compiled into a resistance density plot (RDP), fig. 3.4b. The red line is a guide to the eyes for the MR-measurement along 10° described earlier. Calculated magneto resistance measurements, with the exchange bias pointing along the 315° direction, are compiled into a RDP and shown in figure 3.4c.

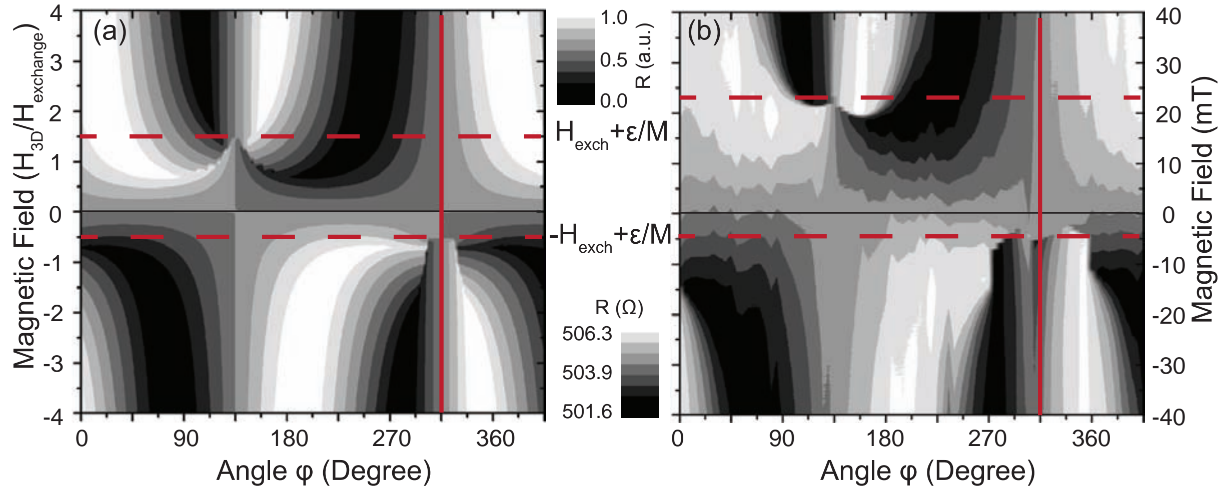

Fig. 3.5: a) Modeled resistance density plot for a Py-MgO system including exchange bias, biaxial anisotropy and domain wall nucleation propagation energy. b) MR measurements for various direction compiled into a resistance density plot.

The basis of the calculation is the simple vector model as described earlier in this section. By comparing measurement with the simulation it is obvious that the vector model assumption are appropriate for an intuitive picture of the Py-MgO system, but it can not explain the details along the exchange bias axis (315°, 135°). The model has two nodal points along the exchange bias axis ((315°, -1) and (135°, 1)), where all contour lines meet. At this point the internal exchange bias and the external magnetic field H_{3D} have the same amplitude. The two nodal points are not visible in the experiment. The parabolic shape of the nodal lines in the simulation are replaced by a double-u and a rectangular shape along 315° and 135°, respectively.

Adding a biaxial anisotropy and allowing the system to change the magnetization direction due to domain wall nucleation propagation with an energy ϵ, the model can explain the difference. Fig. 3.5 shows the measured and the calculated RDP. Both missing features from fig. 3.4 are now visible in the modeled RDP. Analysis of the incorportion of the domain wall nucleation propagation energy show, that the shift of the nodal points give a value for ϵ. The nodal points are shifted by ϵ/M. The easy axes of the biaxial anisotropy are along 315° and 135° and the strength of $H_{exchange}$ and ϵ/M can be determined to 14 mT and 9 mT, respectively.

3.1.3 Permalloy without Cap Layer

Naturally oxidized Permalloy thin films exhibit a uniaxial anisotropy at room temperature. At low temperature the anisotropy changes with magnetic field [Hage 67]. Exchange coupling between the ferromagnetic permalloy and the antiferromagnetic oxide below the Néel of the AFM accounts for this phenomena. The reason is, that the reversal of the permalloy magnetization direction also reverses a large fraction of the spin orientations in the antiferromagnetic material. This effect implies the presence of a rotatable anisotropy in such systems. Ref. [Stil 99] proposes a model for exchange anisotropy in polycrystalline AFM/FM bilayers in which independent antiferromagnetic grains are coupled to the magnetization of the ferromagnetic layer. The AFM layer contains stable grains, which contribute to the unidirectional anisotropy, and hysteretic grains which account for the rotatable anisotropy. Without a cap layer the natural oxide consists of NiO on an Fe oxide layer [Fitz 06].

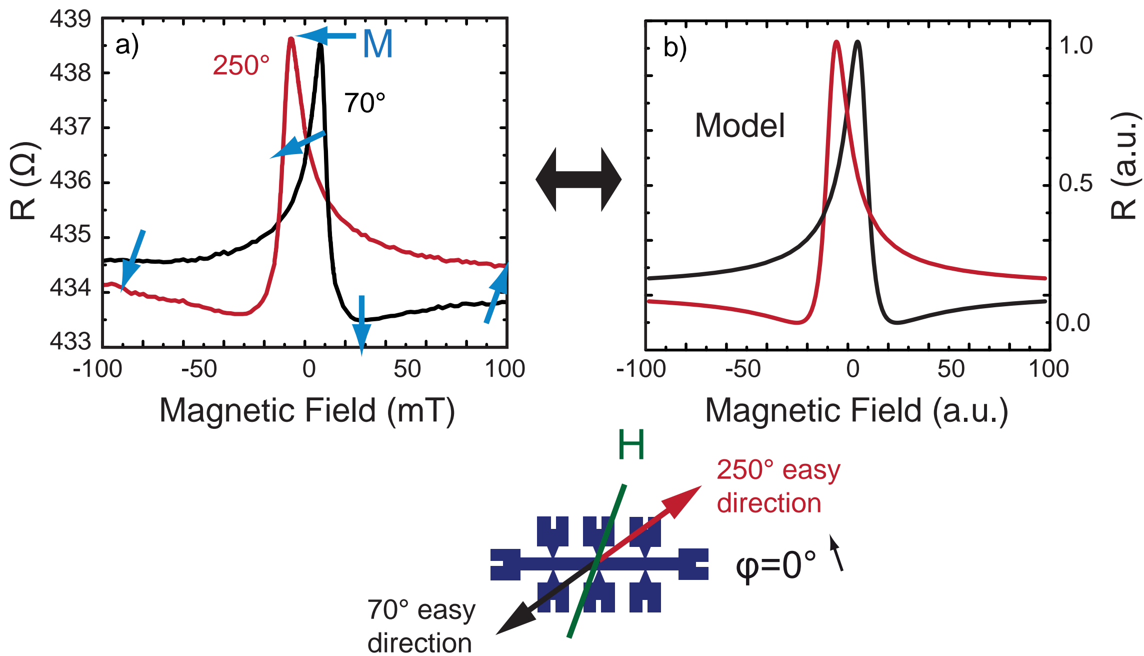

Fig. 3.6: a) MR measurements along 70° and 250° of a 7 nm permalloy layer naturally oxidized on air on a GaAs substrate. Blue arrows show the magnetization reversal of the 70° (black) measurement. b) Calculated MR measurements for 70° and 250°. For the 70° the unidirectional anisotropy points towards 210° and for the field sweep along 250° the easy axes is parallel to 30°. Sketch of the experimental configuration.

Figure 3.6a presents two MR measurements along 70° (black) and 250° (red) of a 7 nm permalloy layer naturally oxidized on air on a GaAs substrate. The blue arrows in 3.6a (black) show the magnetization reorientation of the permalloy when sweeping a magnetic field from -300 mT to +300 mT along 70°. Two calculated MR measurements along 70° and 250° are shown in fig. 3.6b. In the field sweep directions along 70° the calculation

assumes a unidirectional anisotropy along 210°, fig. 3.6. For the 250° direction the easy axes is orientated along 30°. The model and the experiment are in good agreement, which shows the presence of a rotatable anisotropy in our system. The two measurements of fig. 3.6a are taken from a set of MR measurements starting from 0° to 360° with $\Delta\varphi = 10°$. The mirror symmetry of the two shown measurements stems from the analogues preparation procedure by the previous measurements. Taking both MR measurements right after each other yields a different result, because the history is different compared to the measurements in fig. 3.6a. In summary the naturally oxidized permalloy layers show a complicated behavior which can be explained by a rotatable anisotropy. MR measurements on such a layer depend on the history of the system.

3.2 Independent Magnetization Behavior

Having characterized the magnetic behavior of the individual permalloy (previous section) and (Ga,Mn)As (chapter 2) layers we now discuss a hybrid structure. To prepare a hybrid structure, a 100 nm (Ga,Mn)As layer is grown by low-temperature molecular beam epitaxy on a GaAs buffer and substrate. Subsequently, without breaking the vacuum, the sample is transferred to a UHV magnetron sputtering chamber, and a permalloy film with a thickness of 7 nm (and in some cases a 3 nm thick magnesium oxide (MgO) capping film) is deposited on top of the (Ga,Mn)As layer (fig. 3.7b). Using optical lithography and chemically assisted ion beam etching (CAIBE), this layer stack is patterned into a 40 μm wide Hall bar oriented along the (Ga,Mn)As [010] crystal direction. Ti/Au contacts are established through metal evaporation and lift-off.

For an initial study of the layer system, we include an MgO film on top of the permalloy layer to prevent the permalloy from naturally oxidizing in air. Both the unidirectional anisotropy of Py and the principally biaxial in-plane easy axes of (Ga,Mn)As [Sawi 04] can be observed in direct magnetization measurements. Figure 3.7a shows two magnetization hysteresis loops of a layer system composed of (Ga,Mn)As and Py/MgO measured by SQUID. In this experiment a magnetic field of +300 mT has been applied during the cooling procedure from 150 to 4.2 K along the field sweep direction. As a result, the hysteresis curve of the Py/MgO system is shifted along the field axis generally in the opposite ('negative') direction of the cooling field. In addition to the Py/MgO contribution one can see the very characteristic double-step reversal process of the (Ga,Mn)As layer. This layer is not exchange biased, and its behavior is symmetric around the origin. These two statements can be verified by a detailed analysis of the hysteresis curves as follows.

In Fig. 3.7, the red curve was obtained by sweeping the field along 20° with respect to the [010] (Ga,Mn)As crystal direction. The measurement begins at +300 mT, with the magnetization of both layers pointing along the field direction. As the field is reduced the Py magnetization $\mathbf{M}_{Py}$ continues to point in the 20° direction, whereas the (Ga,Mn)As magnetization $\mathbf{M}_{SC}$ gradually relaxes to the [010] easy axis (see inset in fig. 3.7a). In our configuration, the SQUID measures only the projection of the total moment onto the field axis, therefore the (Ga,Mn)As magnetization rotation towards the [010] axis changes the value to $\mathrm{M}_{SC}\mathrm{Cos}(20°)$. This rotation occurs at fields greater than 30 mT and is not visible in the figure. As the field is lowered through zero, at -12 mT a 90° domain wall nucleates and propagates through the (Ga,Mn)As layer, causing a 90° switch in the direction of its magnetization to the [$\bar{1}$00] crystal direction. At -16 mT a second 90° (Ga,Mn)As domain wall nucleates and propagates, completing the reversal. Right after this second (Ga,Mn)As event, the Py changes its magnetization (at -17 mT) from 20° to the 200° direction. For the back sweep of the magnetic field, because it is exchange biased, the Py layer reverses its magnetization before zero field at -6 mT. $\mathbf{M}_{SC}$ is hysteretically symmetric and reverses its direction at positive fields through the same double-step switching process as before. This behavior is characteristic of the two layers responding independently to the applied

magnetic field. After warming the sample to 150 K, and recooling with a magnetic field along 0°, the second hysteresis loop with a field sweep along the (Ga,Mn)As [010] easy axis is measured (fig. 3.7a, gray curve). Due to its unidirectional anisotropy, which is set by the exchange bias and is once again oriented along the measurement axis, the permalloy shows a behavior identical to the 20° direction measurement. Because the sweep direction is now along a (Ga,Mn)As easy axis, the projection onto the field axis after the first 90° switching event is almost zero, and the two switching events occur at almost the same field with an intermediate state having a value corresponding to only the Permalloy total moment. This again confirms the independent character of the two layers. As a reference fig. 3.7b and c shows analogues SQUID measurements of a single (Ga,Mn)As layer and a Py/MgO bilayer.

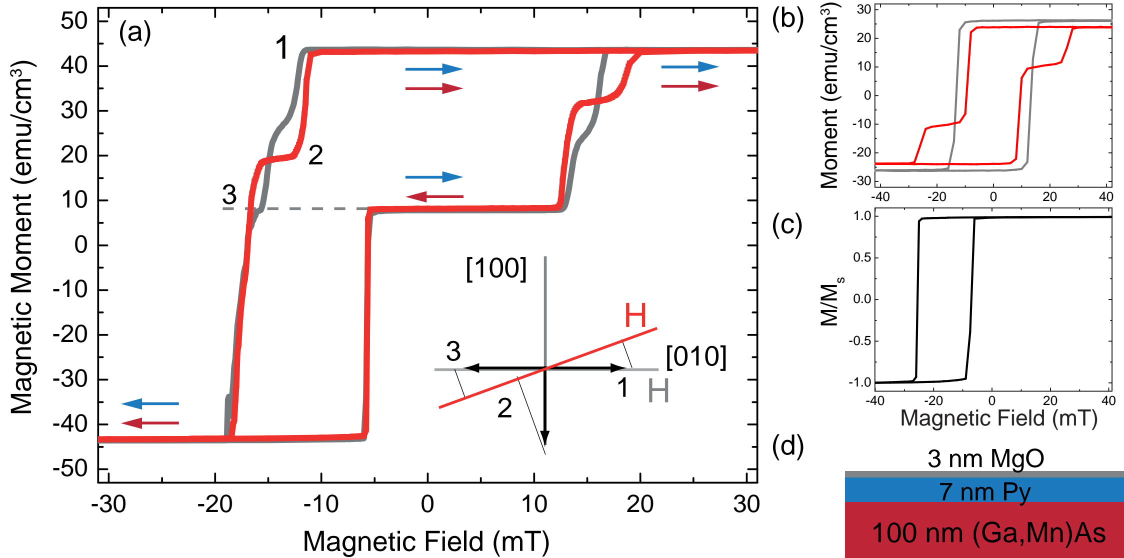

Fig. 3.7: (a) Magnetization hysteresis loop of a hybrid layer system measured along 0° (light gray) and 20° (red) relative to the (Ga,Mn)As [010] easy axis after cooling the sample to 4.2 K in a field of 300 mT. The measurements exhibit clear double-step switching of the (Ga,Mn)As layer and a shifted magnetization contribution of the Py/MgO due to exchange bias. Inset: projection of the magnetization reversal process for the (Ga,Mn)As layer. SQUID measurements of a single (Ga,Mn)As layer along 0° (light gray) and 20° (red) (b) and on a Py/MgO bilayer system (c). (d) Layer stack of the hybrid system.

For a more detailed analysis of this independent switching behavior, transport measurements are performed at 4.2 K in a magnetocryostat fitted with three orthogonal Helmholtz coils which can produce a magnetic field of up to 300 mT in any direction. Results discussed here are for longitudinal resistance (R_{xx}) measurements. In (Ga,Mn)As, the resistance is larger for current perpendicular to the magnetization than for current parallel to the magnetization [Baxt 02] while the opposite is true for permalloy.

Figure 3.8a presents a magnetoresistance curve along 20° for the hybrid system of fig.

3.7 (100 nm (Ga,Mn)As, 7 nm Py and 3 nm MgO), obtained after cooling the sample in a 300 mT field oriented along 0°, and where one can identify the properties of the individual layers. The reorientation of $\mathbf{M}_{Py}$ starts at negative fields and switches to the preferred axis at $H_{Py} \sim -9$ mT. The two (Ga,Mn)As switching fields H_{c1} and H_{c2} are at ~ 11 mT and ~ 20 mT, respectively. To outline the full anisotropy, the positive field half of such magnetoresistance curves for multiple directions (here every 5°) are merged into a gray scale resistance polar plot with the magnetic field H along the radius as shown in fig. 3.8b. The gray scale encodes the resistance values, where black denotes minimum and white maximum resistance. The single curve from fig. 3.8a is along the dashed line in fig. 3.8b. In order to more clearly understand the anisotropy pattern of this hybrid system, we now present data on characteristic individual (Ga,Mn)As and Py/MgO layers.

Figure 3.8c shows AMR of a 7 nm thick Py layer capped by a 3 nm thick MgO layer. Its primary anisotropy is unidirectional due to exchange bias of ~ 15 mT. After a field cooling procedure the unidirectional anisotropy points along the Hall bar which is defined as the 0° direction in this case. At high negative magnetic fields along 20° the Py magnetization is antiparallel to the 20° direction. As the field is brought back towards zero (black curve) $\mathbf{M}_{Py}$ rotates towards the unidirectional easy direction. Since this is more than 90° from the original direction, this rotation initially increases as $cos^2\vartheta$, and this leads to a decrease in resistance. At $H_{Py} \sim -9$ mT, $\mathbf{M}_{Py}$ switches abruptly to the 0° direction before having reached the point where $\mathbf{M}_{Py}$ and $\mathbf{I}$ are perpendicular to each other. At zero magnetic field $\mathbf{M}_{Py}||\mathbf{I}$, and we observe a high resistance state. A back trace from high positive field to negative field for the 20° direction is also shown in fig. 3.8c (light gray). For a pure unidirectional anisotropy one expects two identical MR-curves. The deviations of the two directions comes from an additional biaxial anisotropy in the Py/MgO system [Mich 98] with a strength of approximately 7 mT.

Figure 3.8e presents a (Ga,Mn)As magnetoresistance curve along 20°. At -20 mT the magnetization has already relaxed to the [0$\bar{1}$0] (Ga,Mn)As easy axis. A first abrupt resistance change at the field H_{c1} happens due to a reorientation of $\mathbf{M}_{SC}$ towards the [100] (Ga,Mn)As easy axis. A second reorientation of $\mathbf{M}_{SC}$ towards [010] at H_{c2} completes the magnetization reversal. By comparing to the RPP of the individual layers (fig. 3.8d,f), it is clear that in the RPP of the hybrid system the characteristic square pattern of the (Ga,Mn)As anisotropies is superimposed on the pattern from the Py layer. This behavior again demonstrates the independent switching of the two magnetic layers.

As in GMR and TMR devices, these two independent magnetic layers allow us to set up two non-volatile resistance states. We demonstrate this with minor loops, sweeping the magnetic field from negative saturation to a positive field value and back to negative saturation. Figure 3.9a shows two minor loops along 20° and a reference full trace (light gray) as described in fig. 3.8a. The unidirectional anisotropy in the Py layer is now set by field cooling along the (Ga,Mn)As [010] crystal direction. Each minor loop is of course identical to the reference curve until their reversal point. Therefore only the back sweeps of the minor loops are shown. Coming from negative saturation the magnetization

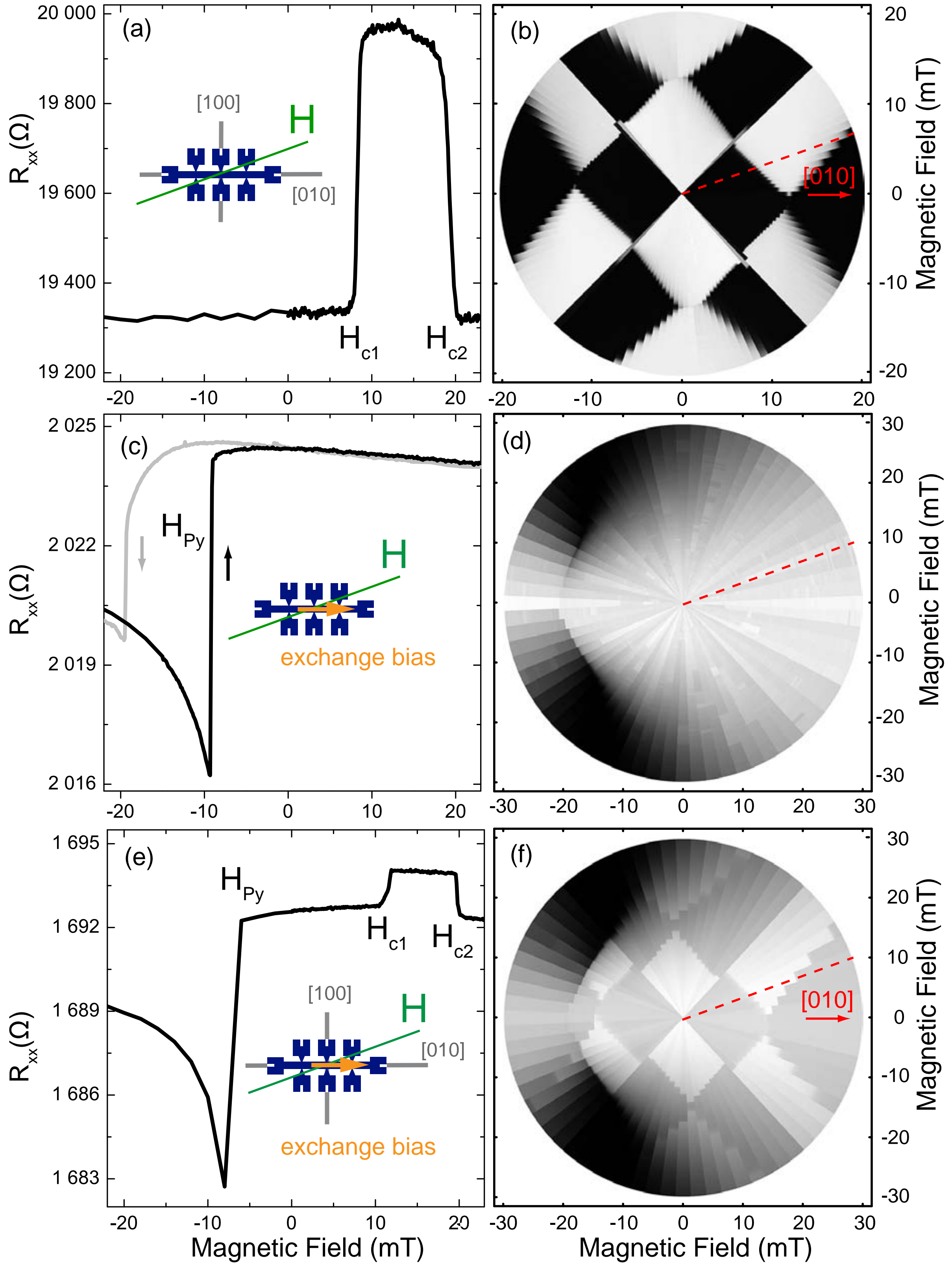

Fig. 3.8: AMR measurements along 20° for layers composed of (Ga,Mn)As/Py/MgO (a), and control samples of Py/MgO (c) and (Ga,Mn)As (d). b) Grayscale resistance polar plot of the (Ga,Mn)As/Py/MgO Hall bar, with the 20° direction is marked by a dashed line. RPP for the two control layers are given in the insets of (c) and (d).

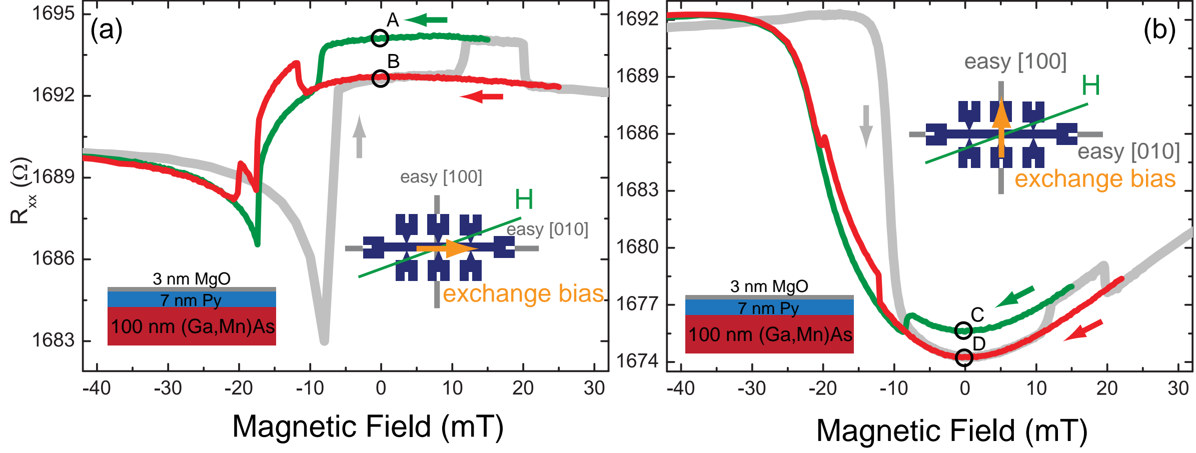

Fig. 3.9: Minor loops measured along 20° with respect to the (Ga,Mn)As [010] crystal direction on a hybrid system. (a) with Py/MgO unidirectional anisotropy along [010] and (b) with Py/MgO unidirectional anisotropy along [100]. Light gray: reference curve, green: back sweep from 15 mT, and red: back sweep from 25 mT.

states of both layers are antiparallel at zero field (fig. 3.9a). Sweeping the magnetic field further, the (Ga,Mn)As magnetization reorients at ~ 11 mT to the [100] crystal direction through a domain wall nucleation and propagation. On stopping the field at ~ 15 mT and sweeping it back to zero, $\mathbf{M}_{SC}$ points perpendicular to $\mathbf{M}_{Py}$. This corresponds to a high resistance state associated with an angle of $\vartheta_{Py} = 0°$ between $\mathbf{I}$ and $\mathbf{M}_{Py}$ and an angle of $\vartheta_{SC} = 90°$ between $\mathbf{I}$ and $\mathbf{M}_{SC}$. Repeating the whole procedure and sweeping the magnetic field to ~ 25 mT instead of ~ 15 mT, (Ga,Mn)As completes the magnetization reversal through a second domain wall nucleation and propagation. Back at zero field the magnetization states of the Py and (Ga,Mn)As layers are aligned parallel to each other. This corresponds to a high resistance state for Py and a low resistance state for (Ga,Mn)As.

Figure 3.9b shows a similar configuration except the unidirectional anisotropy is reset by warming the sample to 150 K and cooling it with an appropriate applied magnetic field, to point along [100] instead of [010]. At zero field the Py magnetization is always parallel to [100], which is equal to a permalloy low resistance state ($\mathbf{I} \perp \mathbf{M}_{Py}$). The behavior of the (Ga,Mn)As layer is identical to the minor loop described in fig. 3.9a. There are again two different resistance states which can be ascribed to the AMR effect of the individual layers (fig. 3.9b labeled C and D).

To confirm that the magnetic independence of the two layers does not originate from an insulating layer causing electrical decoupling at the interface, we determined the interface resistance in samples where current is passed through the interface. The resulting contact resistance is less than $10^{-5}\Omega cm^2$, which is comparable to high quality ohmic contacts on (Ga,Mn)As. An explanation for the lack of magnetic coupling between the layers stems from the fact that the magnetism in the Py layer is mediated by free electrons whereas

in the (Ga,Mn)As it is hole mediated. We note that this hypothesis is not inconsistent with the observation that charge transport takes place freely through the interface. For a charge current to flow between an n-type and a p-type layer only requires a mechanism to provide charge conversion at the interface; e.g., Zener tunneling. In contrast, the transport of magnetic order through the interface has much stricter requirements, necessitating the two type of carriers to coherently exchange spin information. Although our best experimental efforts have not detected one, an intrinsic interlayer caused by some inter diffusion of atomic species at the interface [Sacc 08] [Brei 08], can never be fully excluded.

Having established the characteristics of the two in layers, we now show how it can lead to a multi-value memory element. We proceed with a new sample; a layer stack as in fig. 3.7b, but with the MgO left out in favor of a natural oxide on the Py layer. This allows the use of a magnetic field to modify [Stil 99] the exchange bias coupling direction, enabling measurements for various Py magnetization directions at zero field, while remaining at constant temperature. Figure 3.10 shows three minor loops and a full magnetoresistance curve (light gray) of a hybrid system consisting of a 70 nm (Ga,Mn)As and a 7 nm Py layer. The sample is cooled without an applied magnetic field and the magnetic field sweep direction is 70°.

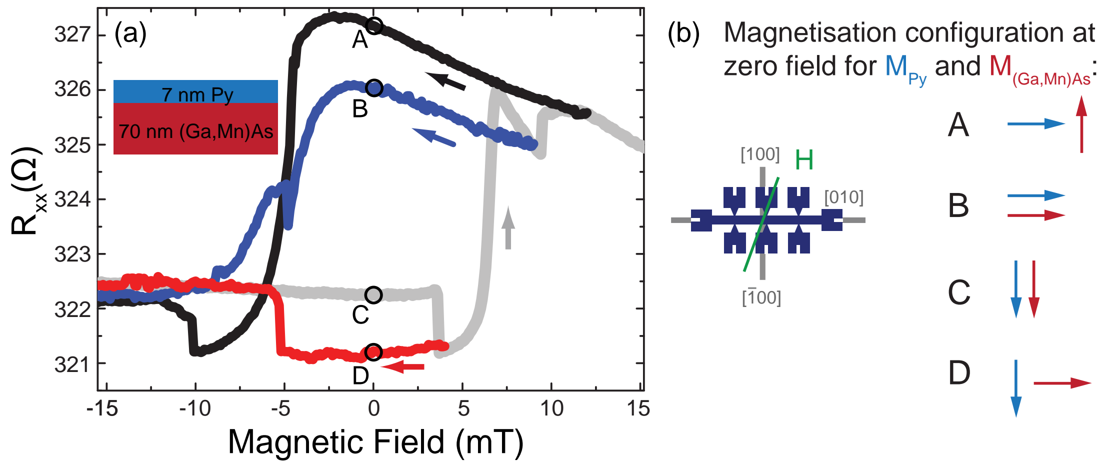

Fig. 3.10: Magneto resistance measurements at 4.2 K along 70° of a hybrid system composed of 70 nm (Ga,Mn)As and 7 nm permalloy without cap layer. Minor loops starting at negative saturation and sweeping to 4 mT, 9 mT and 12 mT.

The field sweep starts at -300 mT, and at 0 mT (labeled C in fig. 3.10) the total resistance has a lower intermediate state, where both magnetization states point parallel towards the (Ga,Mn)As [$\bar{1}$00] which is associated with a high resistance state for (Ga,Mn)As and a low resistance state for Py. The first abrupt resistance change at ∼3.5 mT corresponds to a 90° reorientation of $\mathbf{M}_{SC}$ towards the other (Ga,Mn)As easy axis. Sweeping the field from 4 mT back to zero one reaches the lowest resistance state of the hybrid system (labeled D). By sweeping the magnetic field past +9 mT, we make use of the field rotation effect to realign the exchange bias field between the Py and the natural

oxide layer and therefore also realign the induced anisotropy in the Py layer. Due to this reorientation the Py has a different magnetization state for zero field. This leads to two additional stable states (A,B) in the figure corresponding to $\mathbf{M}_{SC}$ pointing along [010] (B) and [100] (A). The magnetization of the Py layer for these cases is almost parallel to the current direction. These four states are comparable to those we observed earlier with a thermal cycle (fig. 3.10). This time however, all four states are achieved without warming the sample, simply by proper manipulation of the levels using a magnetic field.

Hybrid System with Ruthenium as Cap Layer

The development of FM metal/FM semiconductor hybrid systems and its independent magnetization behavior has been on particular interest of various groups [Macc 08, Zhu 07, Olej 10], which report antiferromagnetic coupling of epitaxial grown FM layers. We do not have evidence for an antiferromagnetic coupling of the Py/MgO and the Mn at the interface, which of course only indicates that the effect of any such coupling is below our detection limit. The effect reported in this work is local in nature, influencing the Mn in the vicinity of the interface, and essentially imposing an order on them. It is of course possible (and indeed likely) that Mn near the interface are subject to a similar interface, but they will also couple strongly to the bulk of the ferromagnetic (Ga,Mn)As layer. The (Ga,Mn)As and the Py/MgO layers have strong inherent anisotropies. We measure the 100 nm (Ga,Mn)As layer and even if some 2 nm of this layer is subjected to a force that attempts to align it anti-parallel to the permalloy, this would have only a small effect on the behavior of the layer. For further investigations on a FM metal / FM semiconductor hybrid system we leave out the MgO and cover the permalloy with a 10 nm Ruthenium layer.

Figure 3.11a presents a magnetization measurement of a 70 nm (Ga,Mn)As, 7 nm permalloy and 10 nm Ruthenium layer. Sweeping the magnetic field from negative saturation to positive saturation shows, that the permalloy layer reverses its magnetization just after zero magnetic field. At around 8 mT the (Ga,Mn)As magnetization switches by 180°. At zero magnetic field the magnetization of both layers point along the same direction and the layers show no antiferromagnetic coupling. Figure 3.11b shows a SQUID measurement of a second wafer with a similar layer stack. In this case the magnetization of the permalloy reverses the direction at negative magnetic fields and the magnetizations of the two layers are in an antiferromagnetic configuration at zero field. Up to now it is not clear which mechanism dominates the coupling at the interface. It is also conceivable that the coupling at the interface reduces the coercive field in the first case, but was not strong enough, to align them antiferromagnetically. Several mechanisms like RKKY like exchange through the interface, orange skin effects, the exact morphology at the interface, dominating anisotropies in the layers could be the origin of the coupling mechanism at

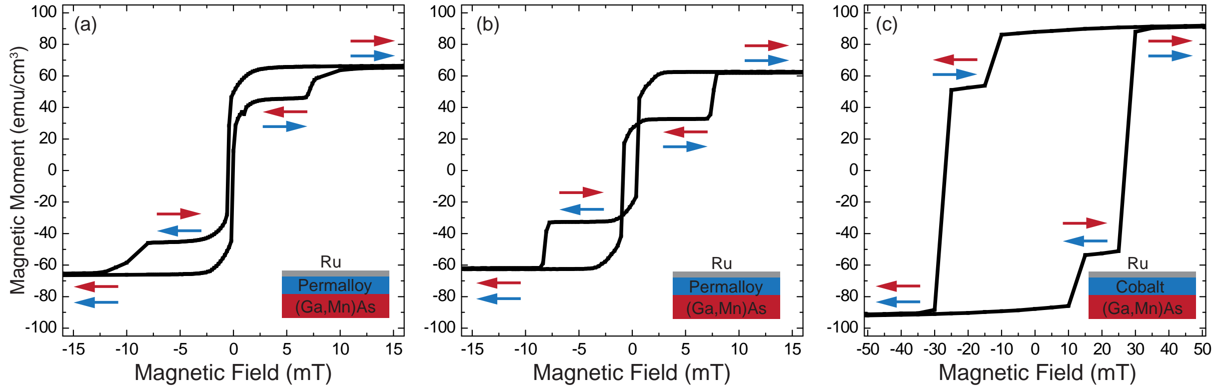

Fig. 3.11: a,b) Hysteresis curves of a 70 nm (Ga,Mn)As, 7 nm permalloy and 10 nm Ruthenium layer which show no coupling (a) and antiferromagnetic coupling (b) at zero field. c) SQUID measurement of a 70 nm (Ga,Mn)As, 6 nm Cobalt and 10 nm Ruthenium layer stack which also shows independent magnetization behavior. The Co is deposited via electron beam evaporation.

the interface.

Replacing the sputtered permalloy layer by 6 nm cobalt (Co) deposited by electron beam evaporation and covered with 10 nm Ru also shows independent magnetization behavior. The alignment of the (Ga,Mn)As and Co magnetization is parallel at zero magnetic field, fig. 3.11c. All measurements in fig. 3.11a, b, c are performed on unpatterned 3×3 mm pieces.

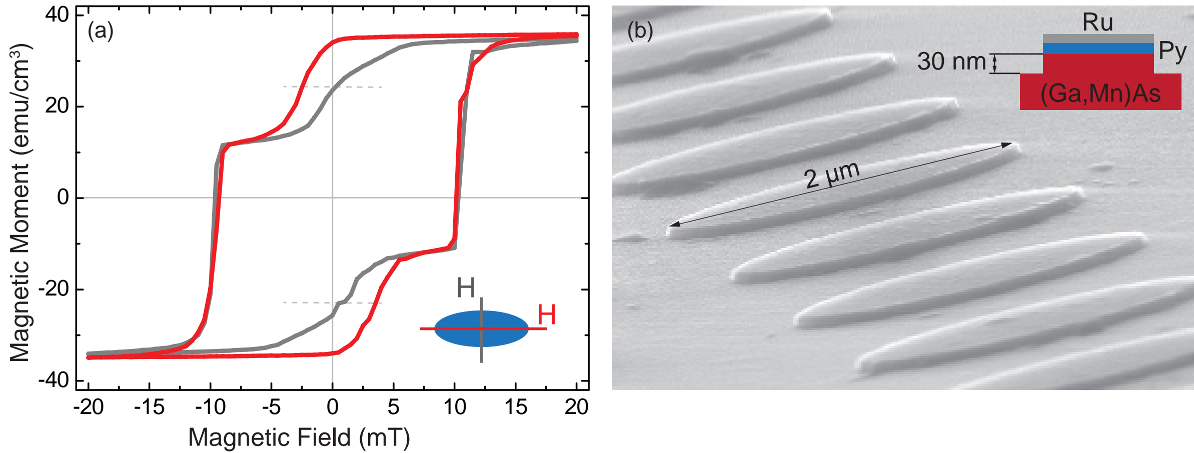

Fig. 3.12: SQUID measurement of 70 nm (Ga,Mn)As, 7 nm Py and 10 nm Ruthenium. The permalloy layer is patterned in array of 1000000 ellipses with the dimensions of 1×2 μm. The magnetic field sweep direction is parallel (red) and perpendicular (grey) to the long axis of the ellipse.

A last example for the independent magnetization behavior is shown in fig. 3.12a. We measure an array of one million permalloy ellipses using a the material of fig. 3.11a. The permalloy ellipses with the dimensions of 1×2 μm are still covered with Ruthenium and

representatives of them can be seen in fig. 3.12b. After e-beam lithography we use Ti as an etching mask and CAIBE for etching the permalloy ellipse array. Etching stops ∼30 nm inside the 70 nm (Ga,Mn)As layer, see sketch in fig. 3.12b. Due to shape anisotropy, the permalloy ellipse has its magnetic easy axis parallel to the long axis of the ellipse. The shape anisotropy of the permalloy ellipse can be calculated to $K_{shape,Py} = 1740\frac{J}{m^3}$ (with a permalloy saturation magnetization of $\mu_0 M_s$=0.8 T), which is equivalent to an anisotropy field of H_A = 5.5 mT [Ahar 98]. The (Ga,Mn)As shape anisotropy of the patterned top 30 nm is $K_{shape,GaMnAs} = 22\frac{J}{m^3}$ and negligible versus the magneto crystalline anisotropy of $K_{cryst,GaMnAs} = 3000\frac{J}{m^3}$. The long axis of the ellipse is parallel to a (Ga,Mn)As easy axis. Two SQUID measurements along (red) and perpendicular (gray) to the ellipses long axis are shown. For the field sweep along the long axis, the magnetizations of the layers are parallel at zero field. Sweeping the external field to positive values the permalloy magnetization start to reverse. The reversal process finishes at 6 mT and the permalloy and the (Ga,Mn)As are in their antiparallel magnetization state. Increasing the external field switches the (Ga,Mn)As magnetization by a 180° at ∼10 mT. Sweeping the magnetic field perpendicular to the long axis of the ellipse and thus along the other (Ga,Mn)As magnetic easy axes results in an identical SQUID response for the (Ga,Mn)As layer. After saturating the magnetization of the permalloy and sweeping the magnetic field back to zero the permalloy magnetization starts to rotate towards its easy axis. The rotation starts at ∼ 6mT, which agrees with the calculated anisotropy field of 5.5 mT. The two magnetizations have a perpendicular state at zero field.

In conclusion we have shown that the coupling of a surface layer of a FM SC to a FM metal observed in ref. [Macc 08] does not preclude independent magnetic behavior between FM bulk (Ga,Mn)As and Permalloy in direct contact, without the need for a nonmagnetic interlayer. The independence of the layers was confirmed both by transport observations, and direct magnetization measurements using SQUID. The SQUID measurements shown on the unpatterned material are ambiguous and need a more detailed investigation of the coupling mechanism at the interface. We also made use of this functionality to demonstrate a two layer hybrid multi-valued memory element with four non-volatile configurations at zero magnetic field.

All transport measurements in this chapter are performed in a lateral transport geometry sending the current parallel to the metal-semiconductor interface. A second possibility is to send the current perpendicular to plane through the interface (CPP configuration). This attempt has also been investigated during this work, using a pillar with an elliptic shape. A ring contact on the (Ga,Mn)As layer was used as backside contact. The results are potentially promising but inconclusive at this stage and need further investigations. The challenge is to increase or isolate the FM-SC/FM-metal interface resistance with respect to measurement disturbing lateral pick up and back-side contact resistances. One approach would be to use a p-doped GaAs as a backside contact similar to ref. [Zhu 07].

The authors of this reference demonstrated the CPP spin valve effect in self-exchange biased ferromagnetic MnAs/(Ga,Mn)As bilayers, as well as in MnAs/ p-GaAs/(Ga,Mn)As trilayers.

Chapter 4

Tunneling

4.1 Metal-Insulator-Semiconductor Tunneling

T is a quantum mechanical transmission probability for an incident particle to tunnel trough an one-dimensional square energy barrier with barrier height V_0 and thickness $2a$ (fig. 4.1a). The transmission probability for a particle incident from the left is

$$T = \frac{1}{1 + (1 + (\epsilon^2/4)sinh^2 2\kappa a}. \tag{4.1}$$

ϵ and κ are defined as $\epsilon = \frac{\kappa}{k} - \frac{k}{\kappa}$ and $\kappa = \sqrt{2m(V_0 - E_z)\hbar}$. k is the wave vector of the incident wave with $k = \sqrt{2mE_z}/\hbar$, V_0 the height of the energy barrier and E_z the energy of the particle. The transmission probability is shown in fig. 4.1b. If the energy E_z of an incident particle is lower than the barrier height V_0, the transmission probability increases with increasing E_z.

The transport of electrons between two metals, separated by a thin insulating layer, is the three dimensional case of the situation described above. Theoretical considerations have led to analytical expressions of the current-voltage characteristics in the tunneling process of Metal-Insulator-Metal (MIM) structures [Simm 63]. An extension of Simmon's model is the theoretical description of transport through a metal-insulator-semiconductor (MIS) junction. Using the WKB approximation and assuming the conservation of energy E and transverse momentum k_z, the tunneling current along z-direction between two conducting regions 1 and 2 through a forbidden region can be written as [Chan 67]:

$$j = \frac{q}{4\pi^2\hbar} \int e^{-\lambda}[f_1(E) - f_2(E)] dk_z^2 dE, \tag{4.2}$$

where q is the electron charge, λ is the tunneling exponent and f_1 and f_2 are the Fermi functions of the two conducting materials left and right of the barrier. Figure 4.2a shows

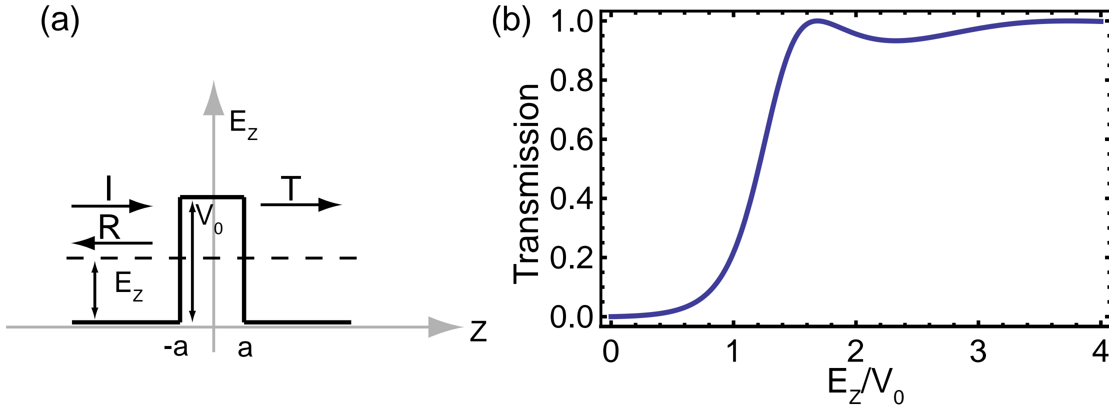

Fig. 4.1: (a) One-dimensional potential barrier with I:incident-, R:reflected-, T:transmitted wave. (b) The transmission for a particle incident upon a potential barrier of height V_0 and thickness 2a. The abscissa E_z/V_0 is the ratio of the total energy of the particle to the height of the potential barrier.

a simplified band diagram of a MIS structure with a degenerate p-type semiconductor in the equilibrium state. Metals typically have a Fermi energy of several electron volt (∼5 eV) and the Fermi energy of the p-type degenerate semiconductor in the sketch is assumed to be ∼150 meV deep in the valence band. The effective masses of the conduction band on the metallic side and the valence band on the semiconductor side differ by a factor of two.

Band bending, image forces and potential drops across the insulating layer at equilibrium are neglected for simplicity. The application of a positive voltage to the metal side, fig. 4.2c , causes electrons tunneling from the valence band of the semiconductor into empty conduction band states of the metal. The current increases monotonically. Due to an increasing applied voltage, the average barrier height decreases and the current further increases. [Dahl 67]

Applying a small negative voltage to the metal, fig. 4.2d, results in electrons tunneling from the metal to the empty valence band states of the p-type semiconductor. Increasing the voltage implies an decrease of the effective barrier height for electrons tunneling from the metal into the empty states of the valence band. If the applied voltage exceeds the maximum of the valence band (assumption: no interface trap states in the forbidden energy gap, fig. 4.2e), the increase in effective barrier height causes a decrease in the tunneling current and has a negative I-V characteristic as can be seen in fig. 4.2g. The increase in effective barrier height is only valid for electrons, which still tunnel into the empty valence band states. The deposition of an oxide layer on the semiconductor leads to the creation of surface states in the forbidden region of the semiconductor energy gap. These surface states influence the IV-characteristic of the MIS structure by acting as available energy states in the forbidden region or as recombination centers for

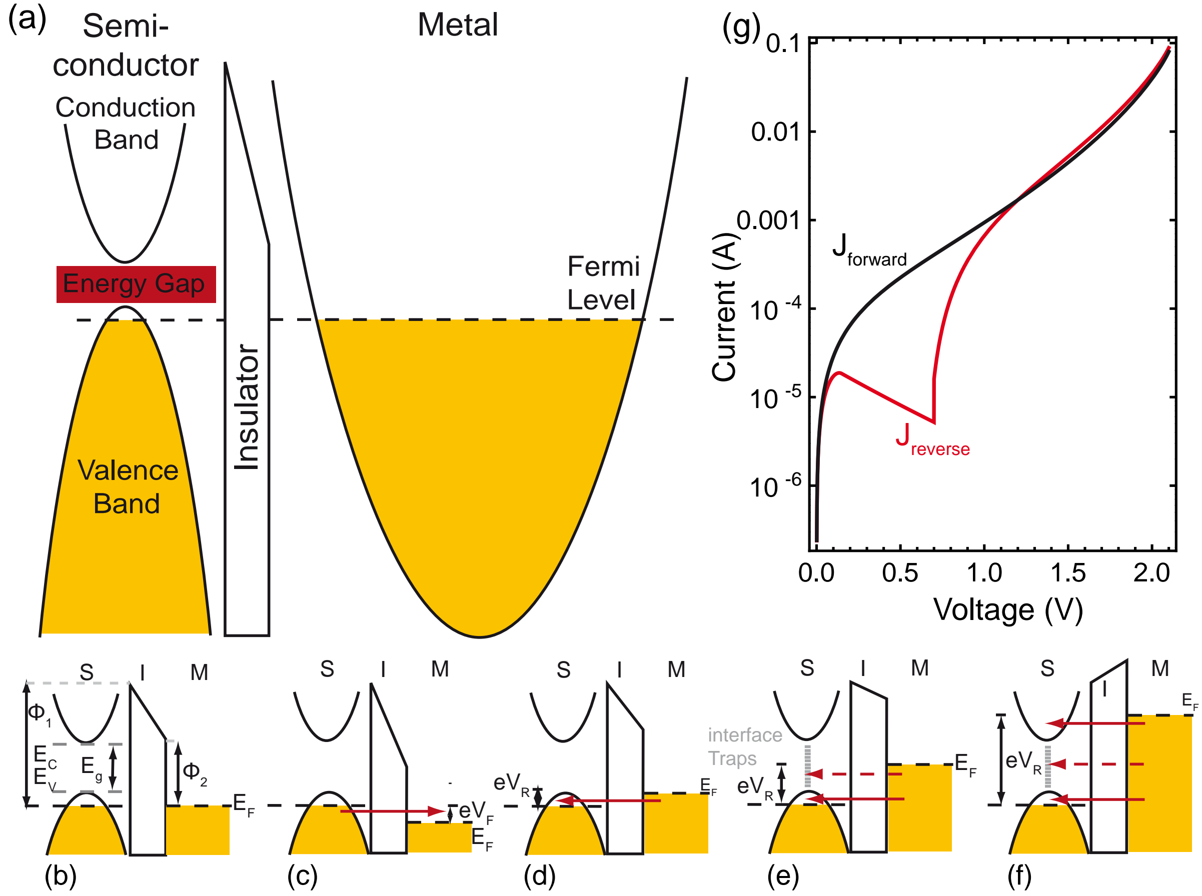

Fig. 4.2: a) Simplified band model of a MIS-tunneling structure. The semiconductor is p-type degenerate b) V=0, equilibrium state, no net current flowing c) V > 0, tunneling of valence electrons into the metal d) V < 0, electrons tunnel into unoccupied states of the valence band e) V < 0, electrons tunnel into unoccupied valence states and empty interface states and recombine with majority holes f) a third component add to the current as tunneling of electrons into empty conduction band. (g) Calculated I-V characteristic (after [Chan 67]) for an ideal case of no interface traps. Figure adapted to [Dahl 67].

the electrons tunneling from the metal. For non perfect barriers the electrons with higher energies can tunnel into empty interface states and immediately recombine with holes in the valence band. Since the barrier decreases with bias for electrons tunneling into the interface trap states, this current component has a positive I-V characteristic. A third component adds to the total current when the applied voltage is high enough to allow the electrons of the metal to tunnel in states of the semiconductor conduction band. [Dahl 67]

Figure 4.2g shows a calculated I-V characteristic for a barrier without interface trap states (after [Chan 67]). The current in the reverse direction starts to decrease as soon as the applied voltage is equal to the Fermi energy of the p-type semiconductor and it rapidly increases again when the applied voltage reaches the bottom of the semiconductor

conduction band. The current in the forward direction is a monotonically increasing function.

4.2 TAMR

TAMR (Tunneling anisotropic magneto resistance) [Goul 04, Rust 05b] was first discovered in an experiment investigating the injection of tunneling current into a ferromagnetic semiconductor. For realizing this, a ferromagnetic (Ga,Mn)As layer is covered by an Aluminum oxide (AlOx) tunnel barrier. To define a proper tunnel barrier, the AlOx is covered by a Ti/Au capping layer. Traditional magneto resistance experiments, as GMR (Giant Magneto Resistance) or TMR (Tunneling Magneto Resistance), consist of at least two ferromagnetic layers in contrast to this experiment, which only has a single ferromagnetic layer.

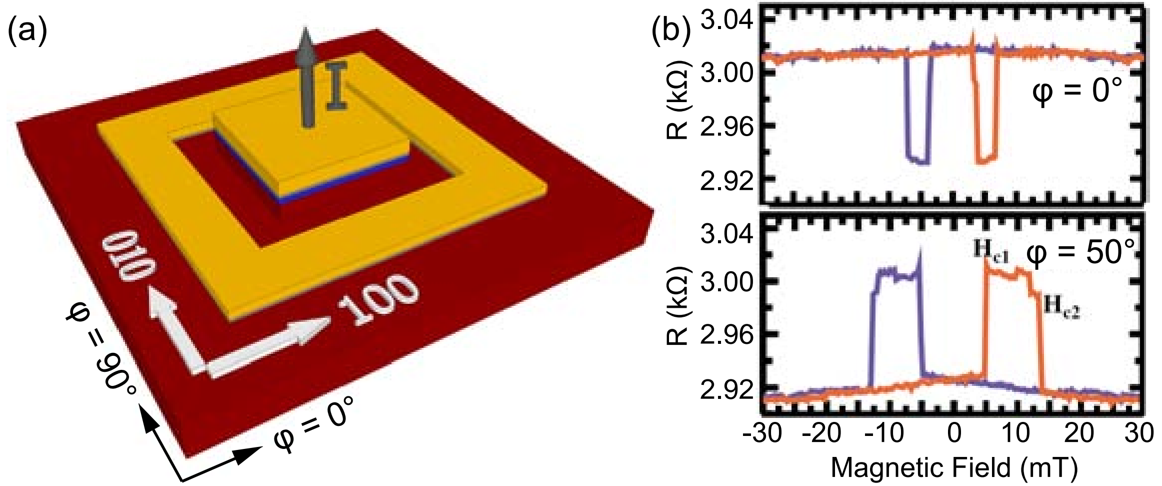

Fig. 4.3: a) Sample design of the original TAMR structure. The layer stack consists of a 70nm (Ga,Mn)As, 2.7 nm AlOx and a Ti/Au capping layer. b) Magnetoresistance measurements along $\varphi = 0°$ and $\varphi = 50°$ including the back sweep of the respective direction (MR taken from ref. [Goul 04]).

The original structure consists of a 100×100 µm^2 pillar surrounded by a Ti/Au back side contact, see fig. 4.3a. The (Ga,Mn)As resistance between the central pillar and the backside contact is much lower as the tunneling resistance and can therefore be neglected in this geometry. Figure 4.3b represents two magnetoresistance measurements [Goul 04]. Sweeping the magnetic field in the sample plane along the $\varphi = 0°$ direction (parallel to the [100] crystal direction) the magnetization reverses its direction due to the characteristic double step switching process of (Ga,Mn)As (fig. 4.3b red). The back sweep (blue) is also shown. The magnetoresistance looks similar to a spin-valve-like signal. Analogue to

AMR or IPH the sign and the switching fields H_{c1} and H_{c2} depend on field sweep direction φ, fig. 4.3b. The tunneling resistance of the layer stack is obviously dependent on the magnetization of the (Ga,Mn)As layer.

The current through a tunnel barrier is proportional to:

$$I \propto \int_{-\infty}^{\infty} DOS_{(Ga,Mn)As}(E) \cdot T(E) \cdot DOS_{Au}(E') \cdot (f_{SC}(E) - f_M(E'))dE, \quad (4.3)$$

where DOS_{GaMnAs} and DOS_{Au} are the density of states for the (Ga,Mn)As and the Au-contact, respectively. The $f_{SC}(E)$ is the Fermi distribution of the semiconductor, $f_M(E')$ the Fermi function of the Au contact and E is the total energy perpendicular to the barrier. $T(k_z)$ is the tunneling probability. Since $T(k_z)$ of the AlOx barrier and DOS_{Au} are in first order approximation independent of the external magnetic field, the magnetic response of this material system has to originate from the (Ga,Mn)As density of states. The switching fields H_{c1} and H_{c2} in a TAMR and an AMR polar plot coincide and confirm this theory. The equivalence of the TAMR and AMR measurements will be discussed in detail in section 5.1.2. Since the effect depends on the magnetic response of $DOS_{(Ga,Mn)As}$, the TAMR can be seen as a tool for sensing the density of states of (Ga,Mn)As.

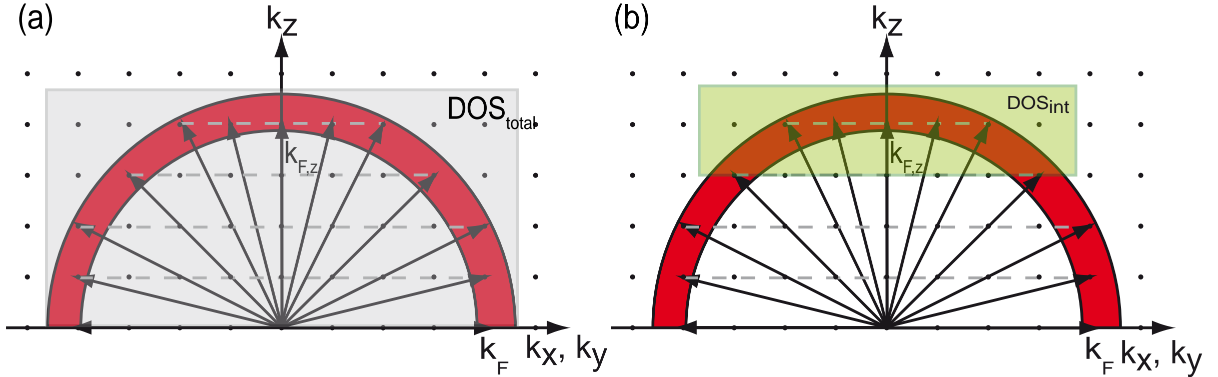

Fig. 4.4: Simplified Fermi sphere of (Ga,Mn)As. States in the red shell participate to the tunnel current. a) In the case of total DOS all k_z contribute b) For a realistic tunnel barrier only a fraction (DOS_{int}) of k_z participates in tunneling.

The amplitude of the TAMR effect for the measurements are shown in fig. 4.3b is $\sim 3\%$. The explanation of the amplitude includes the contribution of the different k-states. For the 3-dimensional case the total energy is:

$$E_{total} = \frac{\hbar^2 k^2}{2m} = \frac{\hbar^2}{2m} \cdot (k_x^2 + k_y^2 + k_z^2) \quad (4.4)$$

where k_x and k_y are the in-plane momentum components. Figure 4.4 shows a simplified Fermi sphere. The tunneling probability in a 3-dimensional case is mainly dependent on

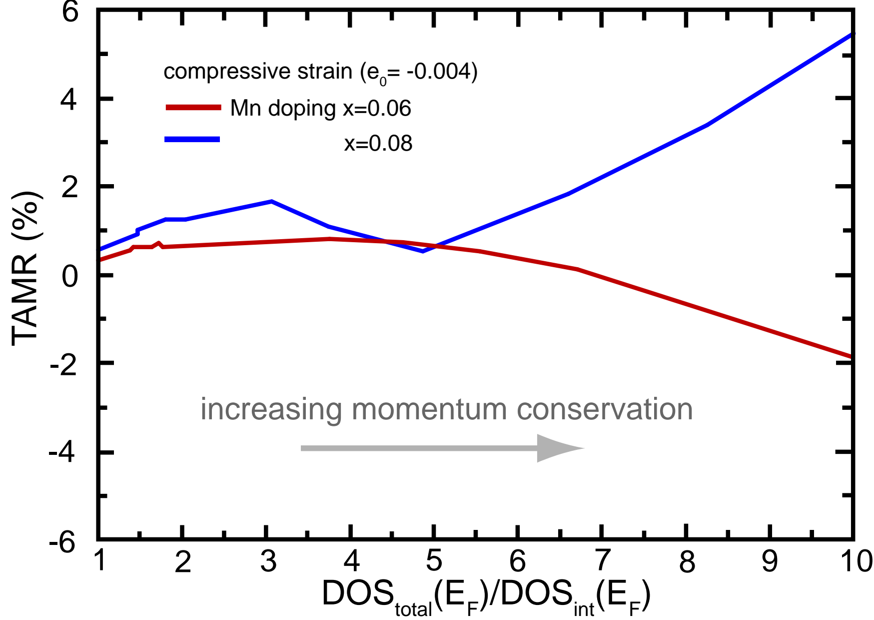

Fig. 4.5: The theoretically calculated TAMR effect size plotted versus the amount of the DOS at the Fermi energy that is assumed to contribute to tunneling, normalized by the total DOS at the Fermi energy. Moving from left to right corresponds to gradually enforcing the momentum conservation condition [Rust 05a].

transverse momentum k_z and the in-plane components contribute with an extra factor to the current. k_z has several values ($0 \leq k_z \leq \sqrt{\frac{2mE_{total}}{\hbar^2}}$) for a given total energy. The Fermi energy E_F of (Ga,Mn)As is $\sim$ 150 meV and the applied voltage is typically $\sim$ (1 - 10) mV. According to 4.3 only states, which are in the region $f_{SC}(E) - f_M(E - eV)$, give a non vanishing contribution to the tunneling current. Consequently, contributing states are within a shell at the Fermi energy and this region is marked red in fig. 4.4. Hence, the current in equation 4.3 depends on the density of states at the Fermi level.

We now consider two extreme cases for the tunneling process. First, total coherent tunneling (ballistic tunneling) without scattering in the barrier, which results in total momentum conservation for k_z and $k_{||}$ (momentum parallel the tunneling barrier k_x, k_y). Second, dirty barriers with no in-plane momentum conservation (incoherent, sequentiell tunneling) and elastic scattering at the interface or in the tunnel barrier. For the second case of no in-plane momentum conservation, all states have the same tunnel probability $T(k_z) = const.$ independent of their initial k_z-state. Thus all states have the same weight to the tunnel current. The total DOS (DOS_{total}, fig. 4.4a) obtained by integrating over all k_z up to the Fermi wave vector $k_{F,z}$, and summing over all bands, has an anisotropy with respect to the magnetization direction at E_F of less than 1% and can not explain the measurements.

For the case of total in-plane momentum conservation the tunneling is dominated by

states in (Ga,Mn)As with k_z close to k_F in each band, because states with higher k_z have higher tunnel probability, see fig. 4.1b. That is the case, when the tunnel barrier is perfect and only states with large k_z contribute considerable to the TAMR effect. These circumstances raise the amplitude of this relative effect. For a proper treatment of the tunnel barrier it would be necessary to treat the different k_z states with a different tunnel probability, see fig. 4.1b.

In the experimental situation neither of the two extreme cases does apply. To explain the experimental results, we relax the momentum conservation condition and add states with decreasing k_z to the tunnel current, see green box for DOS_{int} in fig. 4.4b. It is assumed, that all contributing k_z states have the same tunnel probability. This assumption is oversimplified, but appropriate to conceptional explain and quasi quantitatively give a right order of magnitude of the TAMR effect. For $\sim 10\%$ of the total DOS at E_F participating in the tunneling, the theoretical DOS_{int} (integrated over the assumed range of k_z contributing to tunneling and summed over the four bands) anisotropy is consistent with the experimentally observed TAMR effect of several percent. Figure 4.5 shows the TAMR effect size versus the selectivity of k-states. If the ratio of DOS_{total}/DOS_{int} is one, all k_z states will equally contribute to TAMR and the amplitude is $\sim 0.5\%$. The calculations show, that the TAMR effect is very sensitve to the sample parameters. Mn and hole concentration, strain and of course the quality of the barrier can change the magnitude and even the sign of TAMR.

Chapter 5

Micron and Submicron TAMR Probes

Miniaturizing a tunneling anisotropic magneto resistance contact allows local sensing of the density of states of (Ga,Mn)As. This offers the possibility to locally read-out magnetization states in nanoscale devices without the need to add disruptive metal contacts. Using this technique we show that the behavior of (Ga,Mn)As at a submicron scale is closer to that of an ideal macrospin then is the case for macroscopic (Ga,Mn)As layers. In section 4.2 is a theoretical description of the TAMR effect. While in the original TAMR experiment 100 $\times$ 100 μm tunnel contacts are used to measure the effect [Goul 04, Rust 05a], here we employ e-beam lithography to reduce the pillar size down to 260 nm. The original dimensions are not appropriate for device incorporation. The reduced TAMR pillars in this section are able to locally probe the magnetic anisotropies of the material on the submicron scale. In [Goul 04, Rust 05a] AlOx and GaAs were used as a tunnel barrier. During this work alternative barrier materials have been tested, such as amorphous MgO [Bock 09] and epitaxial (Al,Ga)As. Unfortunately neither of them are appropriate for devices incorporation. The reason for (Al,Ga)As will be discussed in section 5.2. If not stated otherwise all measurements in this chapter are done at 4.2 K. Parts of this chapter are also published in [Mark 11b].

5.1 AlOx Tunnel Barrier

The first TAMR structures in [Goul 04] have a square pillar with a square ring contact. The geometry is similar to a Corbino-geometry. The device resistance is dominated by the barrier and the AMR terms for the different current direction cancel out. An alternative geometry approach is a non-local three terminal configuration, which is used for characterization of the tunnel barrier during this work. After MBE growth of the (Ga,Mn)As layer, and without breaking vacuum, the sample is transferred to a UHV evaporation chamber or a magnetron sputtering chamber, where several layers of aluminum are deposited on

the (Ga,Mn)As layer. Each of the Al layers is oxidized for 8 hours in a 200 mBar oxygen atmosphere. For a 1.8 nm Alox barrier we deposit and oxidize 2× 0.9 nm Al (1.5 nm Alox is equivalent to (0.9 + 0.6) nm Alox, 1.2 nm Alox = (0.6 + 0.6) nm Alox). All wafers discussed in this section consist of 70 nm (Ga,Mn)As covered in-situ with Aluminum. To protect the barrier, the AlOx layer is covered in-situ with 5 nm Ti and 30 nm Au. The optical process development was done together with T. Bock [Bock 09].

5.1.1 Electrical Properties of the AlOx Barrier

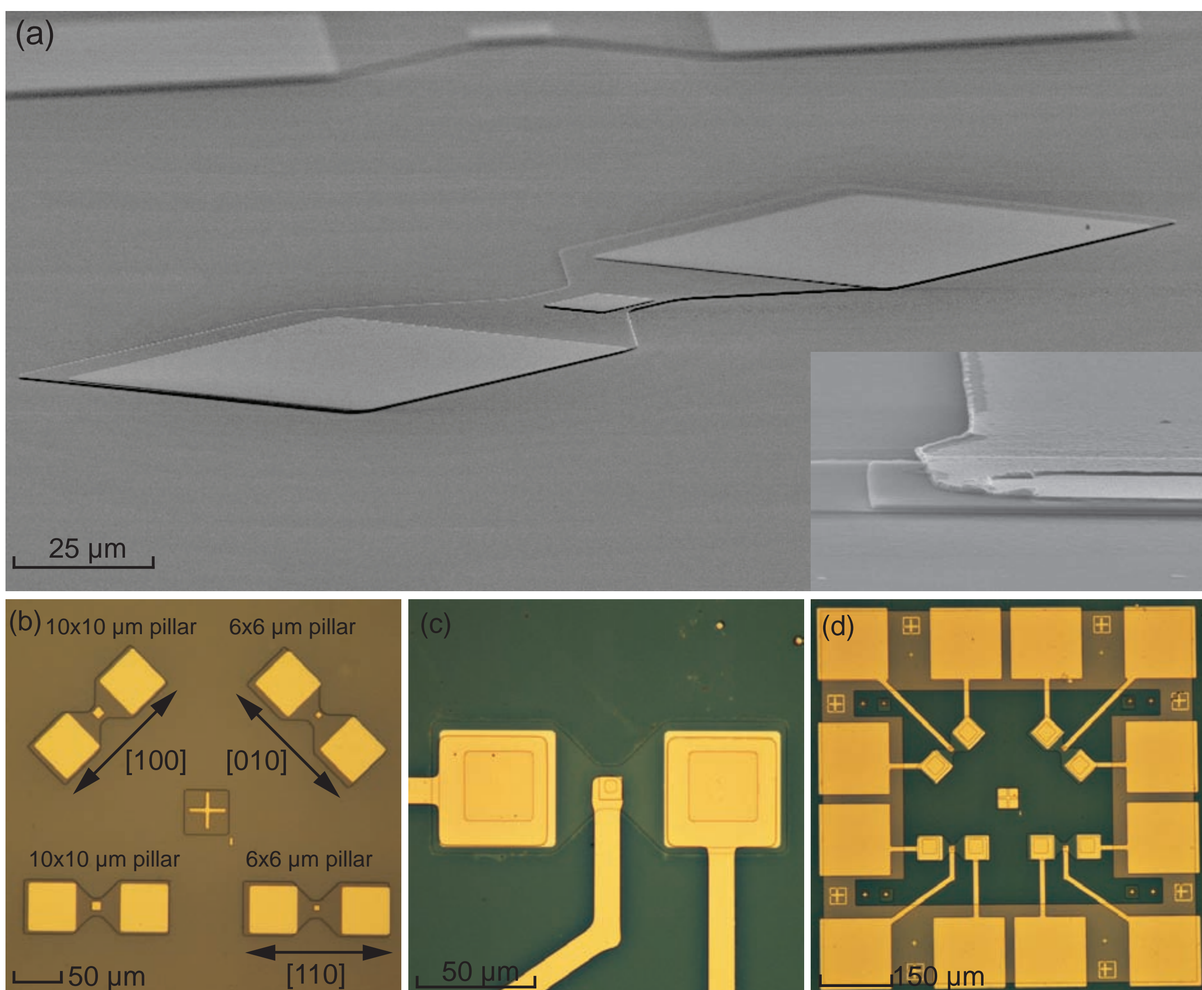

Fig. 5.1: (a) SEM picture of a TAMR structure with a central tunnel barrier and two backside contacts. Side view of the device after three lithography steps and the final structure with the etched SIN and contact leads (inset). (b) top view of the structure with two $10\mu m \times 10\mu m$ and two $6\mu m \times 6\mu m$ pillars. (c) A single TAMR structure and (d) a final structure consisting of four TAMR pillars. The SIN appears green in the figure.

In this section, we discuss the electrical properties of an AlOx tunnel barrier. An optical lithography process is used to miniaturize the pillars down to 6µm × 6µm for a

first characterization of the barrier. Figure 5.1 shows SEM and optical pictures of the three terminal configuration.

The first of five optical lithography steps defines the pillar with the tunnel barrier by evaporation of Ti/Au/Ti as an etching mask. Dry etching with Argon removes the non-covered in-situ metal and etches into the 70 nm (Ga,Mn)As layer. In a second lithography step two Ti/Au backside contacts are evaporated on the etched (Ga,Mn)As layer and a third step defines the mesa for the current path by wet chemical etching. A side view of the first three lithography steps is shown in a SEM picture in fig. 5.1a. The small central square includes the tunnel barrier and the two larger squares serve as backside contacts. Fig. 5.1b (a) shows a top (side) view at this lithography stage. One structure includes four tunnel barriers with two 10μm × 10μm and two 6μm × 6μm pillars. One of each size is aligned along a (Ga,Mn)As easy axes and the other one is parallel to a hard axes. During the fourth lithography step silicon nitride (Si_3N_4, green in fig. 5.1c and d) is used as an insulator to planarize the sample surface. After etching of the SIN with reactive ion etching (RIE) to access the pillar, the two backside contacts and to improve bonding abilities (the SIN below the bonding pads is also removed, see fig. 5.1d), we evaporate a Ti/Au layer. A final structure with a 10μm × 10μm tunnel barrier is shown in fig. 5.1c. The inset in fig. 5.1a shows a side view of a pillar with contact leads and etched Si_3N_4.

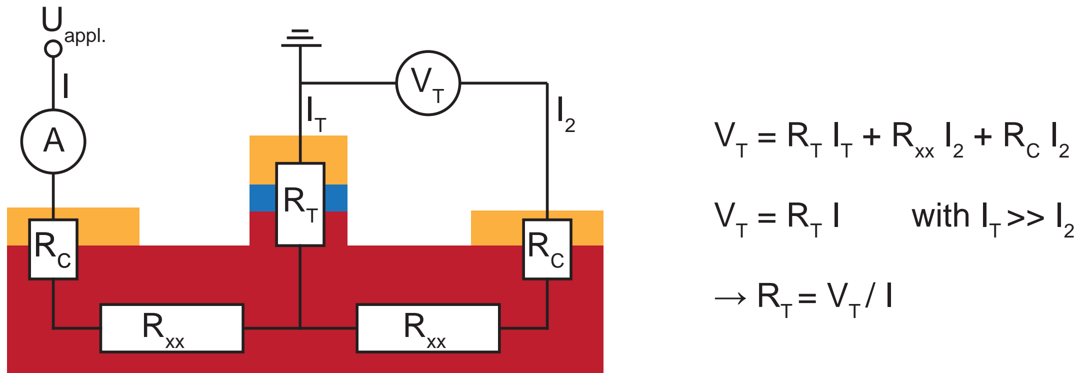

Fig. 5.2: Three terminal non-local configuration for measuring the tunneling properties. This three terminal measurement configuration is dominated by the tunnel barrier resistance R_T and cancels the longitudinal resistance effects of the (Ga,Mn)As sheet.

To characterize the tunnel barrier we use a non-local three terminal configuration. A sketch of the experimental measurement setup can be seen in fig. 5.2. The voltage is applied between the left backside and the central tunneling contact. The circuit includes the contact resistance from one backside contact R_c, the longitudinal resistance R_{xx} and the tunneling resistance R_T. The voltage is measured between the second backside contact and the central pillar. If the inner resistance of the voltmeter is much larger than R_T, the current I_2 is much smaller than I and I_1 and thus the measured resistance is dominated by the tunneling resistance R_T. This simplified model is only valid without current crowding

below the tunnel barrier. Current crowding can be neglected when the tunnel resistance is much larger than the sheet resistance below the barrier. The three terminal measurement configuration is dominated by the tunnel barrier and eliminates the longitudinal resistance effects of the (Ga,Mn)As sheet. Unless otherwise outlined all measurements of the tunnel barrier in this work are measured in a three terminal configuration.

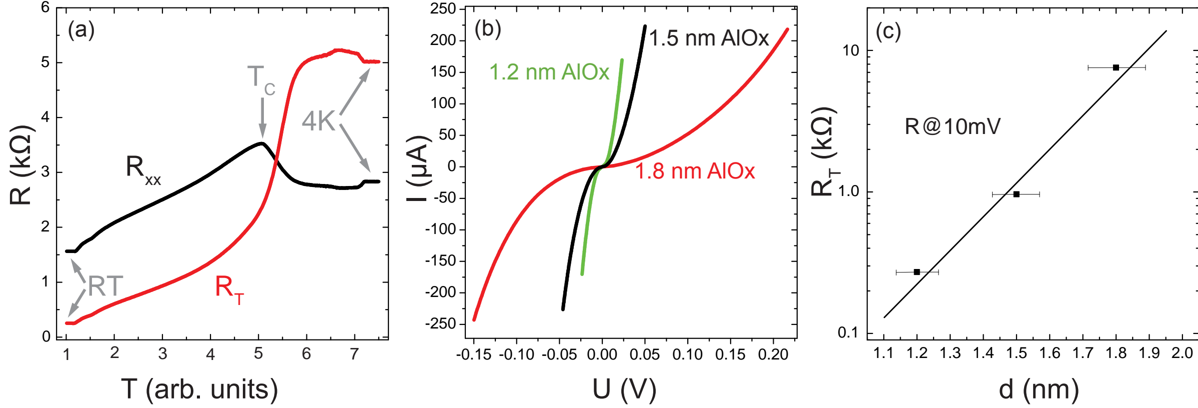

Fig. 5.3: AlOx barriers from sputtert Aluminum layers (a) Three terminal tunnel- (red, 1.5 nm AlOx) and two terminal sheet- (black) resistance as a function of temperature. (b) IV's for three different barrier thicknesses d. (c) Tunnel resistance at 10mV as a function of barrier thickness.

Figure 5.3a (red) shows a typical temperature behavior of the (Ga,Mn)As sheet resistance. The measurement is taken in a two terminal configuration between two back-side contacts on a structure as shown in fig. 5.1c. A detailed description of the temperature dependence of the longitudinal resistance R_{xx} in (Ga,Mn)As is given in [Nova 08]. As the temperature decreases R_{xx} increases as expected for a doped semiconductor. The longitudinal resistance has its maximum at the Curie temperature T_C. R_{xx} decreases below T_C and just before the temperature reaches 4.2 K R_{xx} obviously increases. This last increase can be attributed to a weak localization effect changing the density of states of (Ga,Mn)As. The 4.2 K resistance for a "metallic" (Ga,Mn)As layer is usually between the maximum and the room temperature value [Sawi 04]. As a rule of thumb the sheet resistance for a 70 nm layer with $\sim$ 3.5% Mn concentration is $\sim$1kΩ/square at low T. The distance of two back-side contacts is approximately two squares and since processing reduces the (Ga,Mn)As layer thickness to about 50 nm, the sheet resistance of $\approx$ 3 kΩ is as expected. Rowell defined three criterions, which are applicable to our system to identify a tunneling barrier [Aker 02]: (I) exponential thickness dependence of the resistance, (II) non-linear behavior of the current-voltage relation, and (III) insulating-like temperature dependence of the resistance. The temperature dependence of the tunneling resistance is shown in fig. 5.3a (red) and increases monotonically except for a small decrease just before the temperature reaches 4.2 K. The tunneling resistance does not show a maximum or any other discontinuity at T_C, which confirms, that we indeed measure the

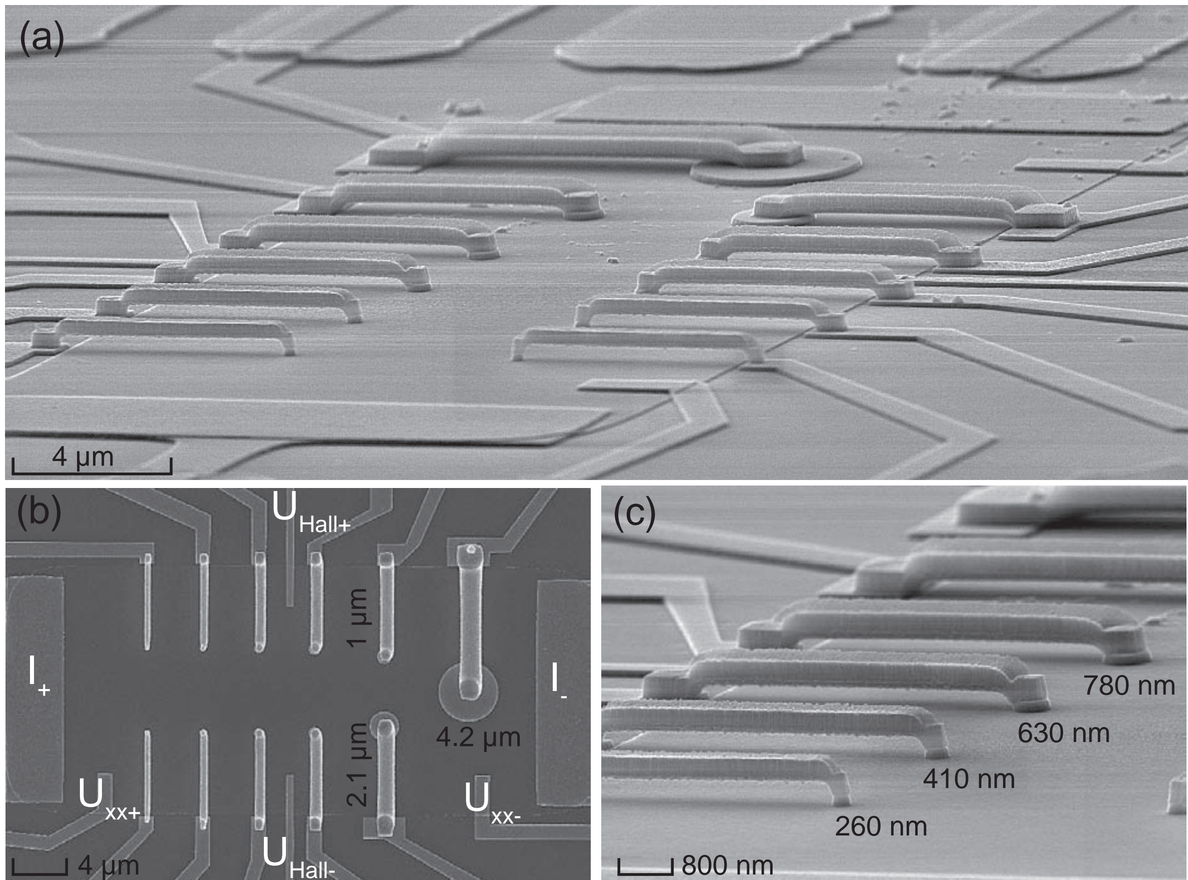

Fig. 5.4: SEM picture of a structure fitted with pillars having various diameters, 260 nm, 410 nm, 630 nm, 780 nm, 1 μm, 2.1 μm and 4.2 μm, respectively.

tunneling properties in a three-terminal configuration. The increase in tunnel resistance with decreasing temperature reveals, that pinholes in the barrier are not dominating. The decrease in tunnel resistance just before the temperature reaches 4.2 K originates from the weak localization effect also visible as an increase in R_{xx}. This decrease of R_T does not stem from a pinhole dominated transport though in the barrier. Fig. 5.3b shows I-V measurements for different barrier thicknesses of 10μm × 10μm pillars. Resistance (R at 10mV) versus barrier thickness shows an exponential dependence as expected from the first Rowell criteria, see fig. 5.3c.

For implementing the TAMR effect in nano-devices the pillar size of 10μm × 10μm and 6μm × 6μm is still to large and needs to be reduced in the submicron range. E-beam lithography is used to define pillars with various diameters. The process is similar to the optical process described above, but instead of using silicon nitride as an insulating material we use metallic-air-bridges made from Ti/Au [Borz 04] to contact the barrier. Fig. 5.4 shows SEM pictures of the device design.

The resistance-area-product versus pillar diameter does not show a constant behavior, fig. 5.5a. The two smallest pillars have a diameter of 260 nm and show a RA-product of

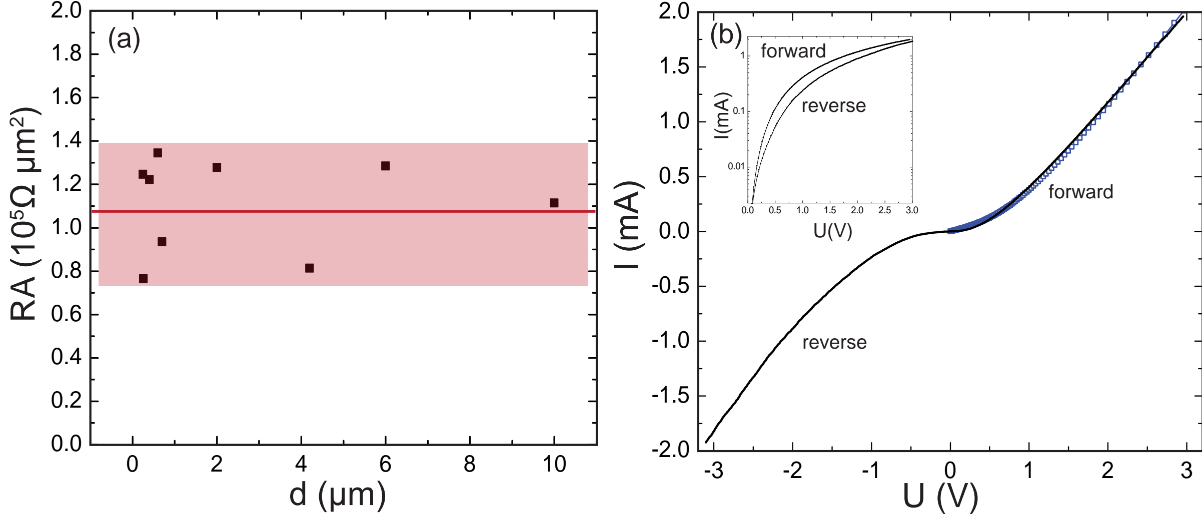

Fig. 5.5: (a) Resistance-area-product for (Ga,Mn)As, AlOx, Ti/Au tunnel barrier. Resistances measured at 10 mV. (b) I-V measurement of a 800 nm pillar for forward and reverse direction. Reverse direction is defined when a negative voltage is applied to the metal. Fit of the forward direction to the model described in section 4.1. I-V measurement in a log-plot (inset).

0.76 $\Omega \times 10^5 \mu m^2$ and 1.24 $\Omega \times 10^5 \mu m^2$. The reason for the spread can be twofold, first a inhomogeneity of the tunnel barrier property or second variations and fluctuations in the density of states of the (Ga,Mn)As layer. A mean value for the RA-product can be given to $(1.1 \pm 0.4)\ \Omega \times 10^5 \mu m^2$. In section 4.1 we describe the theoretical model of an I-V measurement in a M-I-S tunnel structure. Fig. 5.5b shows an I-V measurement of a 800 nm pillar up to ± 3 V. Without any interface states in the bandgap a negative I-V characteristic in the reverse direction should be visible. The reverse direction is defined when a negative voltage is applied to the metal. For comparison with the simulation, the inset of fig. 5.5b shows the same data plotted in a log-plot. The predicted negative resistance is not visible in our samples and is apparently masked by the tunneling of electrons from the metal into the interface states. However, a strong asymmetry among forward and reverse direction exists. This asymmetry confirms two different types of electrodes in the given configuration. The method used for depositing the oxide on top of the doped semiconductor is crucial to actually see a clear band structure influence in the I-V characteristic [Dahl 67]. Nevertheless it is possible to fit the model to the measurement of the forward direction including an additional series resistor, fig. 5.5b blue squares. The $\sim$1 kΩ series resistor in the model limits the current in the high voltage range and accounts for the longitudinal resistance of the material in the circuit. The best fitting values are a barrier thickness of d = 1.5 nm and an average barrier height of $\bar{\phi} = 0.6$ eV. The barrier has a thickness of d = 2.7 nm (3×0.9 nm) (fig. 5.5) and is deposited in a UHV evaporation chamber. This nominal thickness does however not agree with the fitting parameters. A 1.5 nm AlOx barrier deposited in a magnetron sputtering chamber yields an equivalent current-voltage characteristic and agrees with theory. The discrepancy for

the 2.7 nm barrier from the evaporation chamber most likely stems from a higher pin hole density reducing the effective barrier thickness. The temperature dependence of the tunneling resistance of both barriers (not shown) supports this assumption.

5.1.2 Local Domain Sensing with Nanostructured TAMR Probes

After having characterized the tunnel barrier with I-V measurements we now apply an external magnetic field to analyze the magnetic properties (TAMR) of the pillars. In this section, we report both traditional AMR as well as tunneling anisotropic magneto resistance (TAMR) investigations in a 45 μm × 20 μm (Ga,Mn)As mesa structure. The (Ga,Mn)As anisotropies have been investigated in depth in macroscopic samples, but given the intrinsic inhomogeneities of a dilute system such as (Ga,Mn)As [Rich 10], microscopic examination is essential to understanding the properties of nanoscale devices. Fig. 5.6a shows a SEM picture of our device design which has various TAMR pillars of different diameters from 4.2 μm down to 260 nm. The longitudinal resistance R_{AMR} is measured by sending the current from contact I_+ to I_- (which is set to ground), and measuring the voltage drop between contacts V_1 and V_2. To measure the TAMR effect across the tunnel barrier we use a non-local three terminal configuration. Sending the current from contact I_+ to the respective pillar and measuring the voltage drop from the pillar to contact I_-. This three terminal measurement configuration is dominated by the tunnel barrier and cancels the longitudinal resistance effects of the (Ga,Mn)As sheet as discussed in section 5.1.1.

Figure 5.6b shows a AMR (red) measurement of the full mesa, as well as a TAMR (black) measurement on a 260 nm pillar where the magnetic field is directed at an angle of 20° to the [100] crystal direction (fig. 5.6a). The current I in this configuration is along 90°, again with respect to the [100] crystal axis. After saturating the magnetization at a negative field in the 20° direction and sweeping the external field back to zero the magnetization is parallel to the 180° direction and therefore perpendicular to the current. This results in a high resistance state for the longitudinal resistance (AMR effect).

The 0° and 180° directions are also the high resistance states in the TAMR measurement. Sweeping the magnetic field to positive values, the magnetization changes its direction by 90° due to domain wall nucleation and propagation at H_{c1}. Magnetization and current are parallel in this configuration, which results in a low resistance state for both the AMR and the TAMR measurement. Increasing the applied magnetic field along 20° the magnetization orientation changes again due to a 2nd 90° DW (H_{c2}). Noticeable in the data of fig. 5.6b is that in the AMR measurement (red) the magnetization reversal at H_{c1} and H_{c2} are not crisp switches. The magnetization change at H_{c1} starts at 9.4 mT and extends to 11.4 mT. This broadening likely stems from a break up in a multi domain state during the magnetization reversal [Welp 03]. The longitudinal resistance is an average measure of the (Ga,Mn)As material between the two voltage leads V_1 and V_2 and therefore also measures domains with a slightly different domain wall nu-

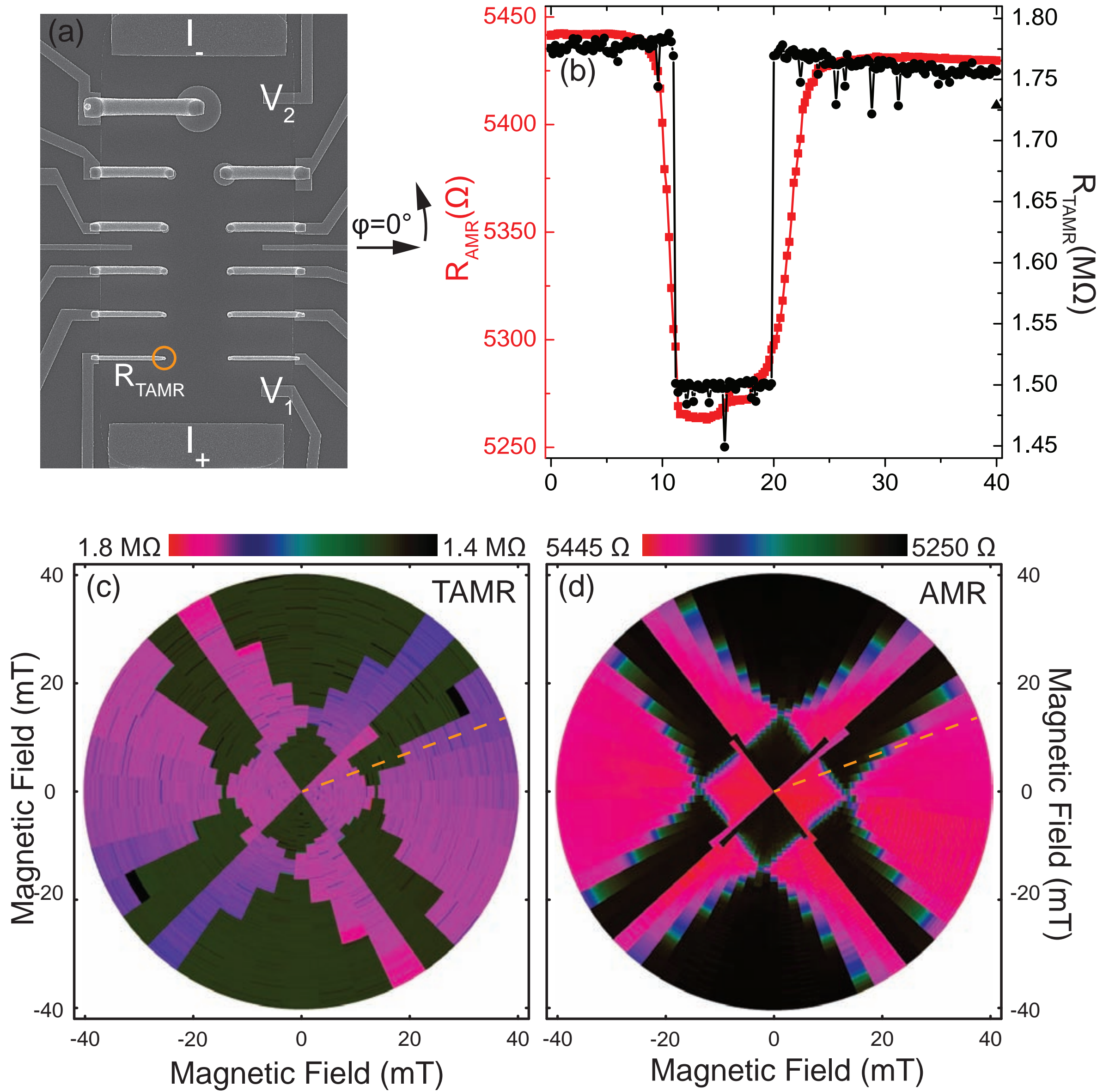

Fig. 5.6: (a) SEM picture of the device, indicating the measurement configuration. The TAMR measurement is taken from a 260 nm diameter pillar marked orange in (a). (b) AMR (red) and TAMR (black) measurements where the magnetic field is at an angle of $\varphi = 20°$ with respect to the [100] crystal direction. (c) TAMR and (d) AMR polar plots for various field sweep directions.

cleation/propagation energy ϵ. Some domains already switch their magnetization at 9.4 mT while other domains switch at slightly higher fields until the reversal process ends at 11.4 mT when all domains have rotated. In contrast to the AMR, the TAMR pillar only senses the (Ga,Mn)As material directly below the tunnel barrier. In our case it measures a circular area with a diameter of 260 nm and the TAMR measurement shows a crisp magnetization reversal event for both switching fields H_{c1} and H_{c2} at 11 mT and 20 mT, respectively. The area below the tunnel barrier obviously behaves as a true macrospin.

If we color code the MR-measurements, where black is low and red is high resistance, we can compile sweeps in various field direction into a resistance polar plot. The associated polar plots for various TAMR and AMR measurements along different magnetic field sweep directions are shown in fig. 5.6c and d, respectively. The broadening of the domain wall switching process is also visible in the resistance polar plot as a smooth transition in the color code. Instead of changing the color abruptly from red to black at H_{c1}, blue and green colors representing intermediate resistance values are visible. This gradual switching is not a unique feature of our device design or (Ga,Mn)As layer, but is ubiquitous to the material [Goul 08]. The transition in the TAMR polar plot, on the other hand, is an abrupt change from red to black at H_{c1} as expected from a single domain event. Comparing the AMR and the TAMR polar plots shows that both measurement techniques give the same magnetic anisotropies. However, the nano-TAMR pillars give us the possibility to directly sense the magnetization in nanometer scaled areas and devices without the need of relatively large disruptive Ti/Au contacts.

Neglecting the crystalline terms [Rush 07] in the AMR, the longitudinal resistance in (Ga,Mn)As, has a $\cos^2(\vartheta)$ dependence, where ϑ denotes the angle between magnetization and current. In (Ga,Mn)As, the resistance for current perpendicular to the magnetization is larger than for current parallel to the magnetization [Baxt 02]. The TAMR effect is more complex. Its resistance depends on the density of states of the two electrodes and the tunneling coefficient $T(k_z)$, which describes the barrier. The density of states of the Au electrode and the tunneling coefficient are to a very good approximation magnetization independent, whereas the (Ga,Mn)As density of states depends on the magnetization of the material. Calculations show that the size and sign of the TAMR effect are very sensitive to sample parameters [Goul 04] such as the anisotropy in the (Ga,Mn)As density of states and the quality of the barrier. Our amorphous AlOx barrier does not perfectly conserve momentum and the exact properties of the barriers may also vary across the sample. Resistance polar plots taken on the different TAMR pillars (not shown) reveal similar abrupt switching fields H_{c1} and H_{c2} for all pillars, with a spread in their exact value which is within the broadening observed in the AMR measurement. Because of the critical influence of the (Ga,Mn)As density of states and the tunneling coefficient on the TAMR resistance, the amplitude of the effect varies from pillar to pillar. To illustrate this we measure the effect when applying a 300 mT saturation field and rotate the field in the sample plane (fig. 5.7). The bias voltage is 10 mV. The external field is large enough that the magnetization follows the external field. For the pillars in fig. 5.7b, f the resistance

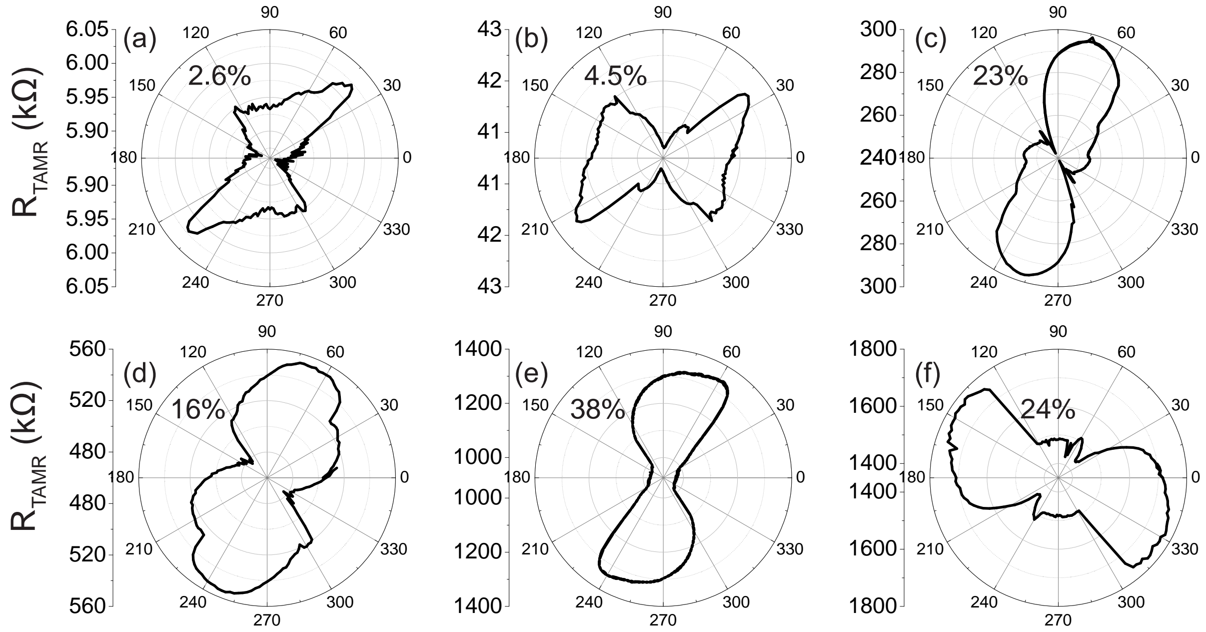

Fig. 5.7: Angular dependence of the magnetization as a function of the direction of a 300 mT external magnetic field for different pillar diameters and at a bias voltage of 10 mV. (a) 4.2 µm, (b) 2.1 µm, (c) 780 nm, (d) 630 nm, (e) 410 nm, (f) 260 nm. The TAMR amplitude is noted in the measurement.

for magnetization along 0° is large compared to 90° and the opposite is true for fig. 5.7a, c, d, e. Since the amplitude of the TAMR is a very complex convolution of k-conservation and the details of the density of states, there is a not a simple relation linking the high resistance state to a specific crystal direction. In particular the [100] and [010] crystal directions (0°, 90°, 180°, 270°) do not necessarily have extremal resistance values.

Noticeable however is that the TAMR amplitude generically tends to increase with reducing pillar size. This is just a loose trend which has its exceptions, such as the 410 nm pillar showing a lower amplitude than the 260 nm pillar. As mentioned earlier the TAMR effect size depends crucially on the combination of barrier quality and the anisotropy in the density of states of (Ga,Mn)As. Very local doping fluctuations in the (Ga,Mn)As and slightly varying barrier properties result in a changing contribution of k-states to the tunneling current. Since not only the amplitude, but even the sign of the TAMR effect depends on these local conditions, averaging over a large sampling area tends to include canceling contributions and thus yields a lower signal than the individual local contributions.

However, for device purposes the total TAMR amplitude plays a minority role. A difference in resistance between the [100] and [010] magnetic easy axes is necessary to be able to distinguish the directions at zero field. In a pure biaxial system the two direction are equivalent and have the same density of states. This results in an identical tunnel resistance. Adding a [110] uniaxial contribution does not change the situation, because

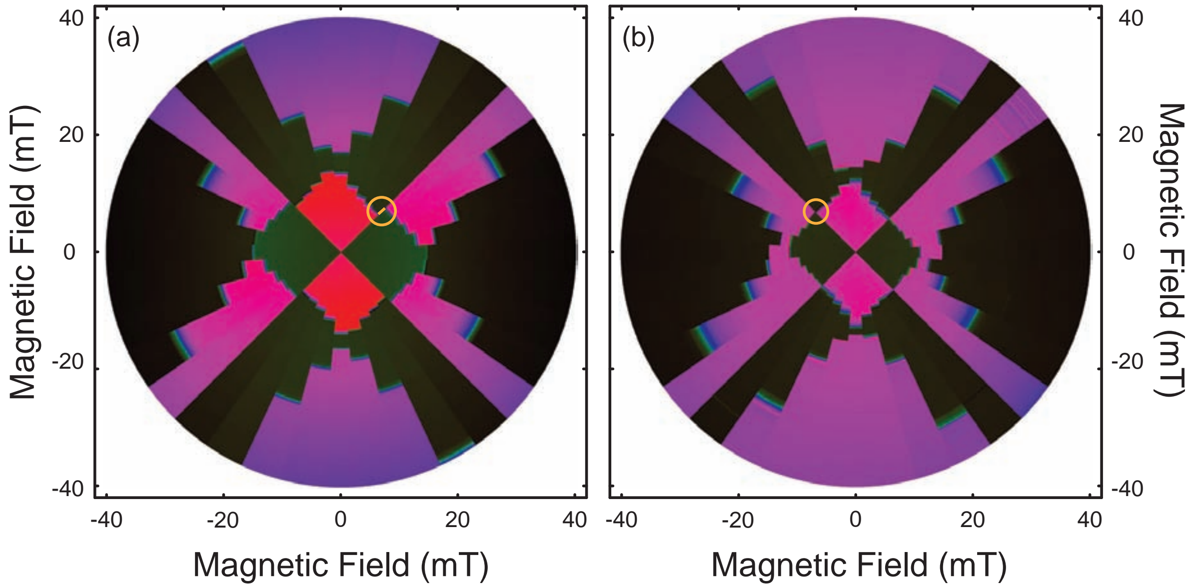

Fig. 5.8: AMR polar plots for two 70 nm (Ga,Mn)As layers grown under identical growth condition. (a) shows a symmetry breaking K_{010} anisotropy component of 1.2 mT whereas in (b) no K_{010} is visible.

the [110] acts equivalently on the two biaxial easy axes. To break the symmetry between the [100] and [010] direction theory introduces an in-plane uniaxial strain term along one of the [100] or [010] direction [Goul 04]. As discussed in section 2.3 this additional uniaxial anisotropy component is also visible in a resistance polar plot where a gap opens in the RPP for the H_{c1}s along a hard axis. Fig. 5.8 shows two AMR polar plots for two 70 nm (Ga,Mn)As layers. Both layers are grown under identical growth conditions one after the other on the same day. The opening in fig. 5.8b is hardly noticeable if there at all. Whereas in fig. 5.8a the opening is clearly exists and the strength of the [010] uniaxial anisotropy component can be calculated to $K_{010} = 1.2$ mT. The existence or strength can not be controllable influenced during growth because up to now the mechanism which generates the symmetry breaking K_{010} is not clarified.

In summary we have miniaturized TAMR pillars down to 260 nm in diameter. With such a small area, one is able to locally sense the magnetization in nanometer device applications. Comparing TAMR and AMR measurements shows that the behavior of macroscopic (Ga,Mn)As regions is not that of a true macrospin, but rather an ensemble average of the behavior of many nearly identical macrospins. Our results show that the magnetic anisotropies of the local regions are consistent with the behavior extracted from macroscopic characterization. The amplitude of the TAMR read out is position dependent, and while it does not follow a strict size dependence, it exhibits a trend of increasing for smaller sample size.

5.1.3 T-dependence of a nano-TAMR Probe

The temperature dependence of the TAMR amplitude at zero field is strongly connected to the T-dependence of the [010] anisotropy component. Figure 5.9 and fig. 5.10 shows the temperature dependence of the symmetry breaking K_{010} uniaxial anisotropy component. The figures presents a comprehensive study of the temperature evolution of AMR- (left column), TAMR-resistance polar plots (center column) and TAMR angular dependent saturation φ-scans (right column). According to ref. [Papp 07a] the temperature dependence of anisotropy components originates in their power-law dependence on the volume magnetization. While K_{cryst} depends on the volume magnetization as M^4, $K_{uni[\bar{1}10]}$ follows as M^2. This particularly means that both components are present till the volume magnetization disappears at T_C. The temperature development of the K_{010} uniaxial anisotropy component can best be observed in the existence of the TAMR signal. As soon as the symmetry breaking component disappears the TAMR signal at zero field disappears. While at 1.6 K the TAMR signal is well pronounced, is rapidly decreases with increasing temperature before it almost vanishes at 25 K.

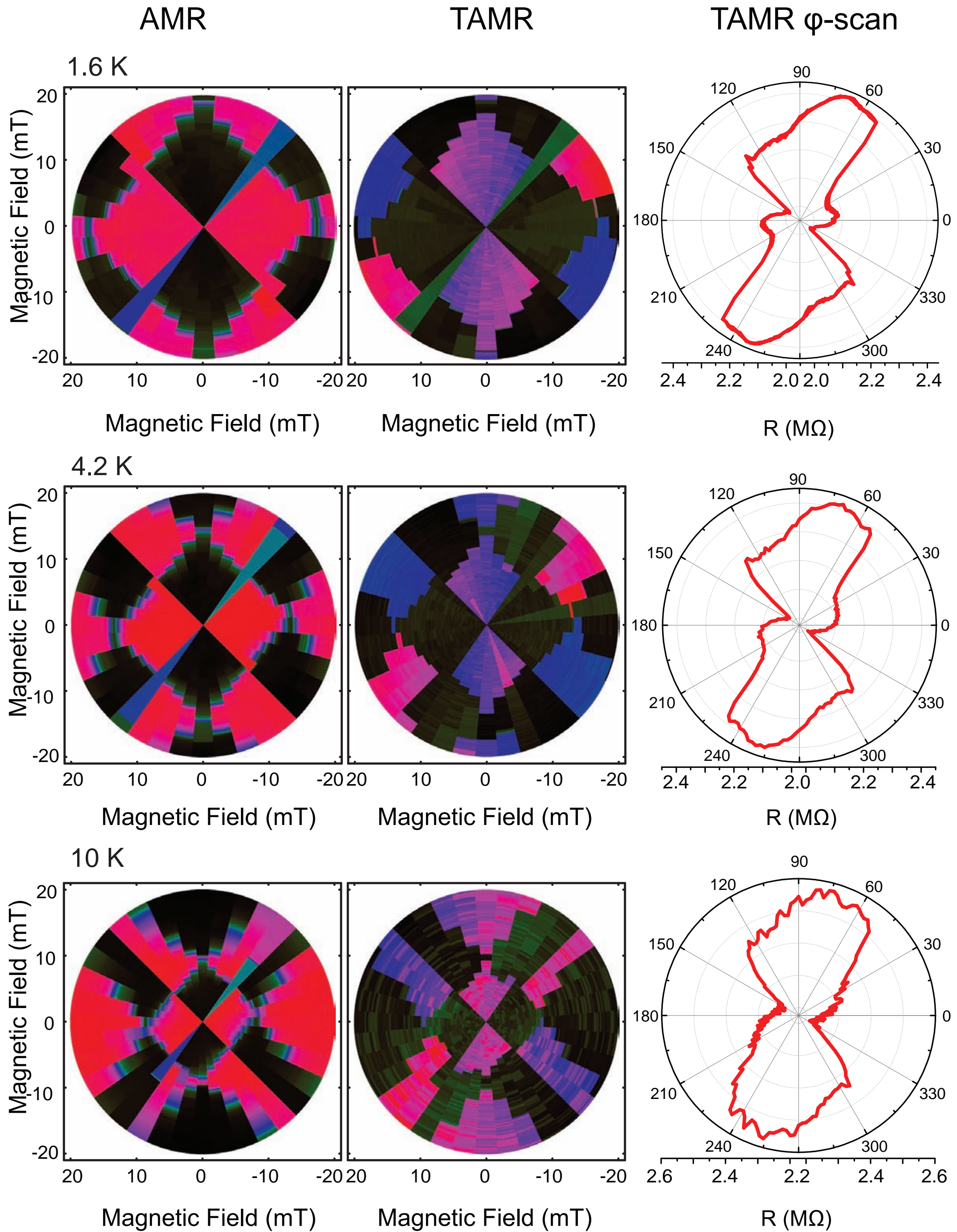

Fig. 5.9: Anisotropic magneto resistance (AMR, first column) verses tunneling anisotropic magneto resistance (TAMR, second column) measurements for different temperatures 1.6 K (first row), 4.2 K (second row) and 10 K (third row). Angular dependence of the magnetization in a saturation φ-scan for the respective temperatures. TAMR measurements are taken at a bias voltage of 10 mV on a 260 nm $\oslash$ pillar

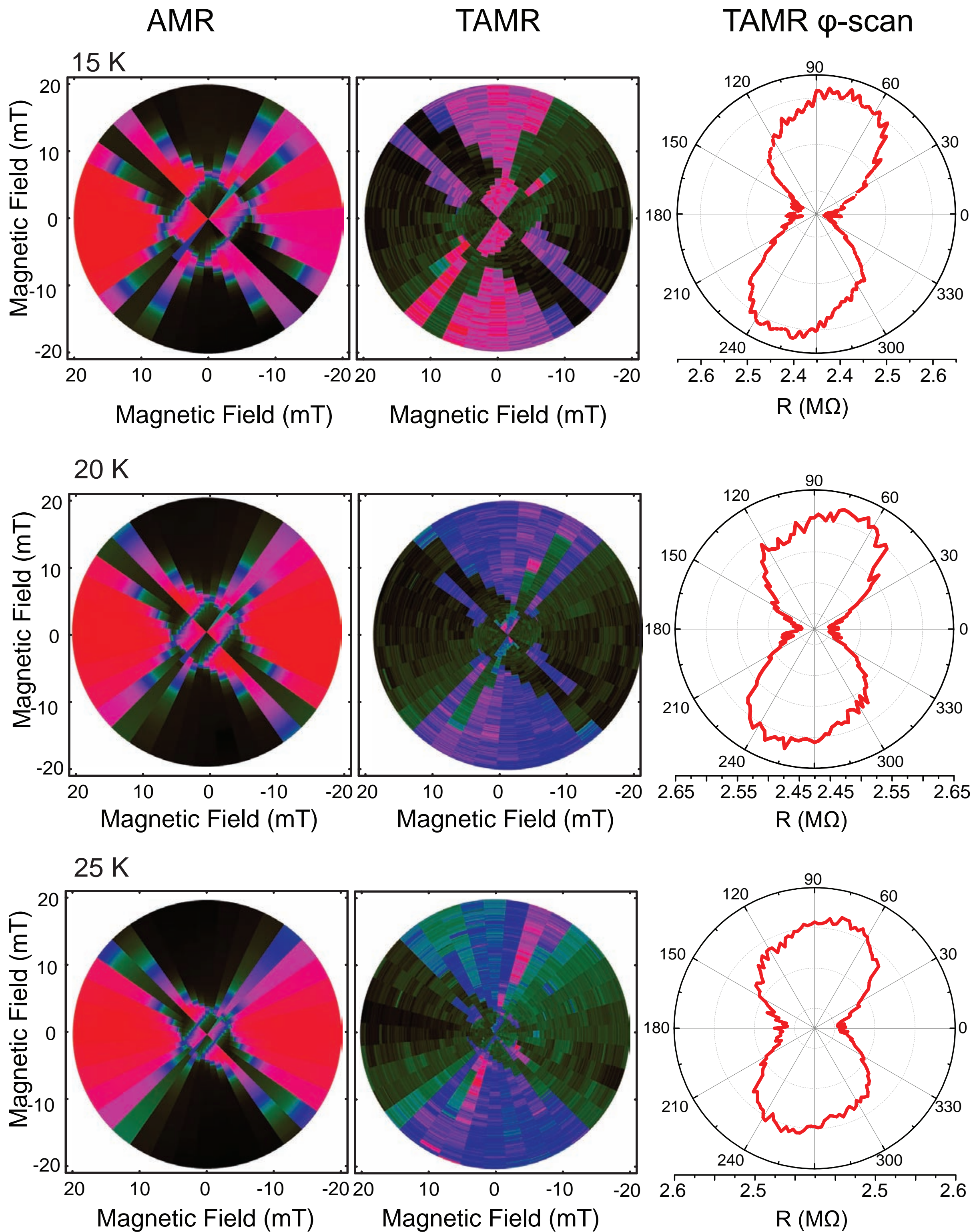

Fig. 5.10: Anisotropic magneto resistance (AMR, first column) verses tunneling anisotropic magneto resistance (TAMR, second column) measurements for different temperatures 15 K (first row), 20 K (second row) and 25 K (third row). Angular dependence of the magnetization in a saturation φ-scan for the respective temperatures.

5.2 Epitaxial (Al,Ga)As barrier

In this section we use an epitaxial (Al,Ga)As layer as a tunnel barrier. One drawback of an amorphous AlOx barrier is, that the TAMR resistance has no strictly defined magnetization dependence, which is connected to the crystal orientation as discussed in the previous section, fig. 5.7. Annealing of the AlOx barrier increases the crystalline properties of the barrier and enhances the ratio between high and low resistance in metal based TMR devices [Park 99], but annealing also changes the magnetic anisotropies of the (Ga,Mn)As layer. An alternative approach to an amorphous AlOx barrier is an epitaxial barrier grown in the MBE. A first realization of an epitaxial barrier is reported in ref. [Rust 05b]. This work reports a very large TAMR effect exceeding 150 000% on an epitaxial (Ga,Mn)As/GaAs/(Ga,Mn)As layer stack. This experiment uses two instead of one ferromagnetic (Ga,Mn)As layers, which gives limitations for spintronic device application. One major advantage of the TAMR effect is, that only one ferromagnetic layer is necessary. Ref. [Gira 05] shows TAMR measurements on a ferromagnetic p^{++}-(Ga,Mn)As/n^{+}-GaAs Zener-Esaki diode. As in a simple tunnel diode the p-n junction of the degenerate semiconductors serves as a tunnel barrier. The (Ga,Mn)As layer in this experiment is compressively strained and thus has its magnetic easy axis in-plane and a magnetic hard axis out of plane. Unfortunately this article only reports a volatile TAMR response for an out of plane magnetic field sweep. For spintronic device applications the TAMR resistance can be used as a read-out for the non-volatile in-plane magnetization direction of the (Ga,Mn)As layer. For this purpose the TAMR amplitude at zero field must necessarily be non-vanishing. Here we investigate the TAMR response of a similar layer stack for in-plane magnetic field sweeps.

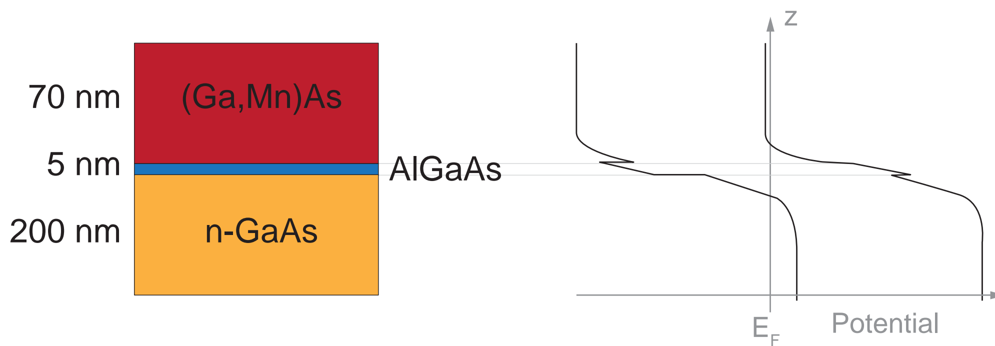

Fig. 5.11: a) Layer stack consisting of 200 nm Si doped n-GaAs, 5 nm AlGaAs barrier and 70 nm thick (Ga,Mn)As layer. b) Potential evolution modeled with WinGreen [WinG] and assuming a n-GaAs layer with a carrier concentration of 1×10^{18} and a p-doped GaAs layer with a concentration of 1×10^{20}. Modeling by M. Rüth.

Our approach for a crystalline tunnel barrier is similar to a tunnel diode. Instead of using the pure p-n junction as the barrier we grow an additional high temperature (T$\sim$ 500°) (Al,Ga)As layer between the high temperature grown Si-doped GaAs and

the p-doped (Ga,Mn)As layer grown at low temperature (T∼ 260°). Fig. 5.11 shows the layer stack and the band diagram in thermal equilibrium modeled with WinGreen [WinG] by M. Rüth. Both semiconductors are heavily doped with impurities and thus are degenerate. The Fermi level is at the origin and lies within the valence band of the (Ga,Mn)As layer and in the conduction band of the Si-GaAs layer. The 5 nm (Al,Ga)As layer has a bandgap of ∼1.8 eV with a Al content of x = 0.3 and presents an additional barrier to the p-n-junction.

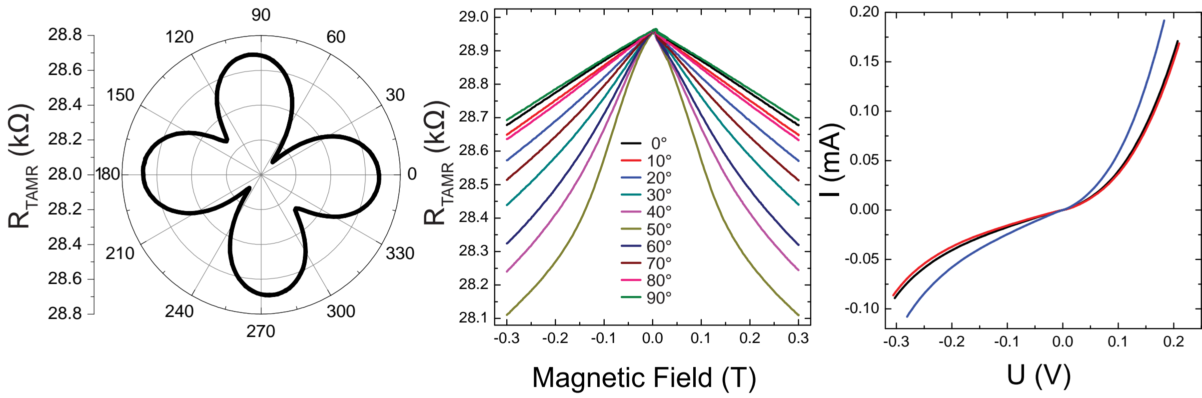

Fig. 5.12: a) Angular dependence of the magnetization in a 300 mT saturation φ-scan at a bias voltage of 10 mV and 5 nm (Al,Ga)As. b) Magnetic field sweeps along various angles starting at the [100] (0°, black) (Ga,Mn)As crystal direction in steps of $\Delta\varphi = 10°$. c) IV measurements on two 150 × 150 µm pillars (black and red) and a 100 × 100 µm pillar (blue).

Before measuring the tunneling properties of the heterostructure we characterize the (Ga,Mn)As layer in a lateral Hall bar geometry. The AMR measurement shows a normal resistance polar plot (not shown) with all three anisotropy components as expected for high quality compressively strained (Ga,Mn)As. The K_{010} anisotropy component, which breaks the symmetry between the [100] and [010] crystal direction, is nicely present in the polar plot and has a strength of 1.5 mT. For the tunneling experiment optical lithography is used to define square pillar sizes of 100 µm, 120 µm and 150 µm. We use CAIBE to etch into the Si-doped GaAs layer and pattern down a Ti/Au ring as a backside contact. IV characteristics can be seen in fig. 5.12a. Either electrons tunnel from the valence band to the conduction band, or vice versa, depending on the direction of the bias voltage. The asymmetry of the device is mirrored in the asymmetry of the IV measurements. Figure 5.12a shows the TAMR angular dependence of the magnetization in a 300 mT saturation φ-scan. The directions 0°, 90°, 180° and 270° are along the crystal directions [100] and [010] and coincide with the high resistance states whereas the magnetic hard axes of (Ga,Mn)As have a low resistance state. The TAMR amplitude at 300 mT is ∼ 2%. This fourfold cloverleaf shape of the magnetization angular dependence is reproducible for various pillars from the same wafer with different pillar sizes. Measurements on samples with a AlGaAs barrier thickness of 3 nm and 4 nm show identical results. Contrary to the amorphous AlOx barrier we have a fourfold symetry, where the tunneling magneto resis-

tance is directly coupled to the lattice directions in the MBE grown crystaline structure. Unfortunately the difference in resistances along 0° and 90° is only in the ppm range and one can thus not distinguish between the two magnetization directions. This situation becomes more obvious by sweeping a magnetic field as shown in fig. 5.12b. Sweeping the magnetic field from -300 mT to 300 mT along the 0° direction (black) results in a high resistance state for the magnetization pointing either along 180° or 0°. Applying a negative saturation field along e.g. 60° the magnetization points along 240° which results in a low resistance state. The magnetization is rotating towards the 270° direction (the nearest magnetic easy axes) when sweeping the field back to zero and the resistance reaches a high state of the 270° direction. The symmetry of the TAMR measurements is uniaxial altough we have a magnetic biaxial material. The two magnetic easy axes are not distinguishable at zero magnetic field.

We have shown in-plane magnetic field sweeps on a zener tunneling structure with an additional epitaxial AlGaAs barrier. In this configuration we have a reproducible resistance-vs-lattice dependence as can be seen from various angular dependent magnetization measurements. The symmetry breaking [010] anisotropy component plays only a minor role in this configuration and thus we loose the possibility to identify the [100] and [010] crystal directions by a difference in resistance at zero field. The equivalence in resistance at zero field for the two (Ga,Mn)As easy axes makes it hardly suitable for spintronic device applications.

Chapter 6

Fully Electrical Read-Write Device Out of (Ga,Mn)As

At present memory and logic fabrication are two fully separated architectures [Awsc 07, Wolf 01]. While bulk information storage traditionally builds on metallic ferromagnet's, logic makes use of gateability of charge carriers in semiconductors. Combining storage and processing in a single monolithic device not only would solve current technical issues such as the heat dissipation generated by transferring information between the two architectures, but also offer the possibility of a fully non-volatile information processing system. Here we present a read-write device which can be used as one element of an electrically programmable logic gate. Parts of this chapter are also published in [Mark 11a].

6.1 Read-Write Processing

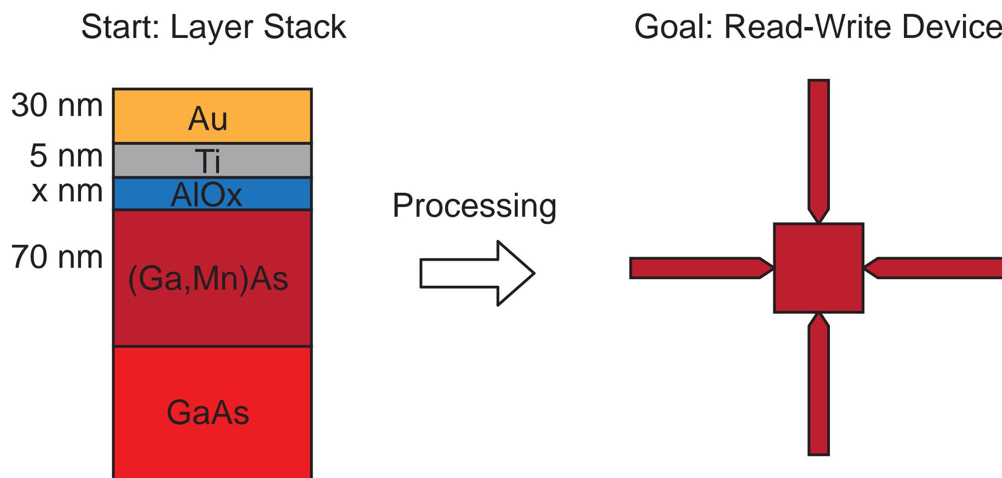

Fig. 6.1: Initial layer stack for processing a Read-Write device (top view).

In this section we give a description of the process used for fabricating the read-

write (RW) device. A layer stack is shown in fig. 6.1. The 70 nm thick (Ga,Mn)As layer is grown by low-temperature molecular beam epitaxy (MBE) on a GaAs buffer and substrate by Lars Ebel. The material is typically grown at a temperature of $\sim$ 260°C, instead of $\sim$ 600°C for normal high temperature GaAs growth, to avoid MnAs clusters. Due to the lattice mismatch to the GaAs buffer the (Ga,Mn)As layer is compressively strained [Shen 97]. After growth of the MBE layers, and without breaking the vacuum, the sample is transferred to a UHV evaporation or a magnetron sputtering chamber, and several aluminum layers are deposited on top of the (Ga,Mn)As layer. After deposition, each of the Al layers is oxidized by keeping it for 8 hours in a 200 mbar oxygen atmosphere. The wafer is covered in-situ by 5 nm Ti and 30 nm Au to properly define and protect the barrier.

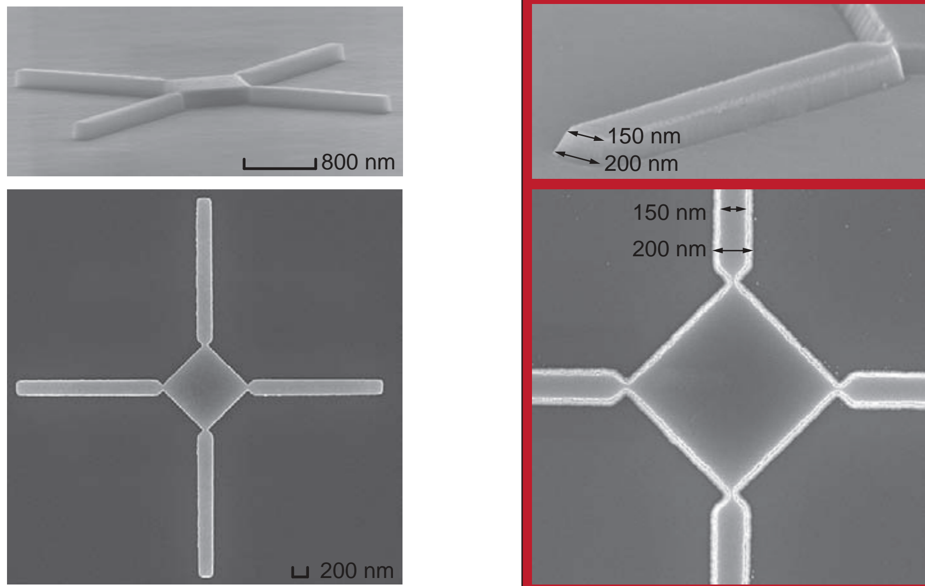

Fig. 6.2: First lithography step (EBL 1). Define the device structure and use Titanium as an etching mask for a dry etching step with CAIBE. Left: optimized etching with a 400 V and a 80 V BCl_3 process. Right: etching with a 400 V BCl_3 process.

After growth of the layer stack, the process includes four electron beam lithography (EBL) steps and one optical lithography step. The process description given in this section, not only shows the optimized results of each lithography step, but also gives some counter examples to illustrate difficulties during process optimization.

The basic idea in our device concept is the magnetization manipulation of a ferromagnetic domain with a spin polarized electrical current. This current changes the magnetization of the domain by the means of current induced switching. To generate such a spin polarized current the carriers pass through a magnetic source domain, where they

acquire a spin polarization. For imparting a torque from the carriers onto magnetic moments, the directions of magnetization of source and drain domain are different. We use anisotropic strain relaxation due to patterning of the material to achieve adjacent regions with different magnetic anisotropies. Different anisotropies can yield different magnetization directions of adjacent domains. The pencil sketch in fig. 6.1 shows a conceptual drawing of the device. It consists of four nanobars which are connected to a central region. Guidelines for the size of the device are set by the nanobars. The width of the nanobars is determined by the transition of the magnetic anisotropy from biaxial to a uniaxial, due to anisotropic strain relaxation [Hump 07]. The nanobars have a width of 200 nm and as a starting shape of the central region we use a square. As a magnetization read-out tool for the central region a TAMR contact is used.

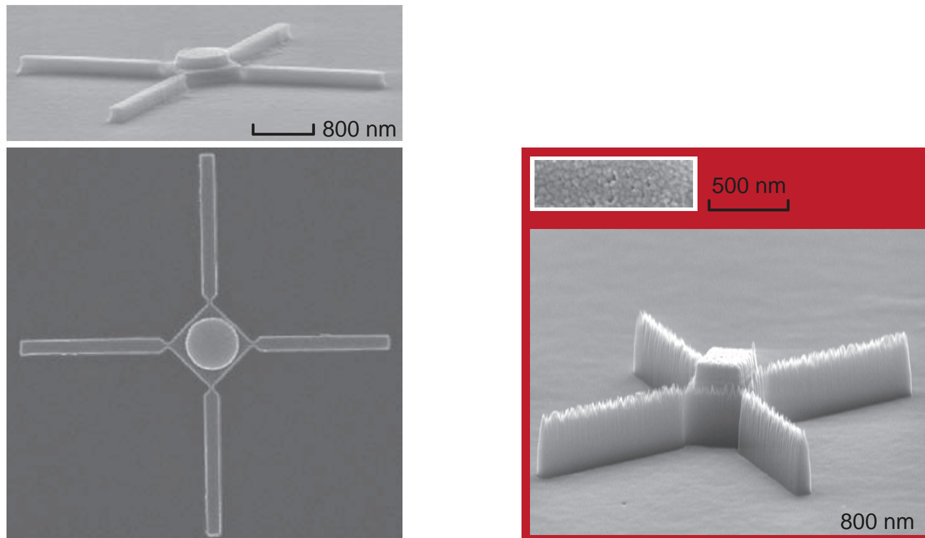

Fig. 6.3: Second lithography step (EBL 2). Define the tunnel contact with a Ti/Au/Ti evaporation on top of the central square and remove the remaining in-situ Ti/Au and AlOx material from the nanobars. Left: etching of in-situ Au with an Ar-sputtering process in CAIBE. Removing the in-situ Ti and AlOx barrier with a wet chemical HF dip. Right: 80 V, BCl_3 process to etch the in-situ Ti/Au and AlOx barrier from the nanobars. Out of plane direction in the right column is exaggerated. Inset: Example of a Au surface with grain structure.

Figure 6.2 shows the first process step, which defines the device geometry. After e-beam exposure, Titanium (Ti) serves as an etching mask for dry etching with chemical assisted ion beam etching (CAIBE). CAIBE combines an Ar-sputtering and a chemical etching process with a reactive gas component and thus has the advantages of anisotropic etching and high etching selectivity. In CAIBE the argon ions are accelerated from a beam source through a voltage onto the target. We use BCl_3 as a reactive gas component, which is directly guided into the etching chamber through a ring source above the sample. This concept decouples the generation of the ion beam from the supply of the reactive gas

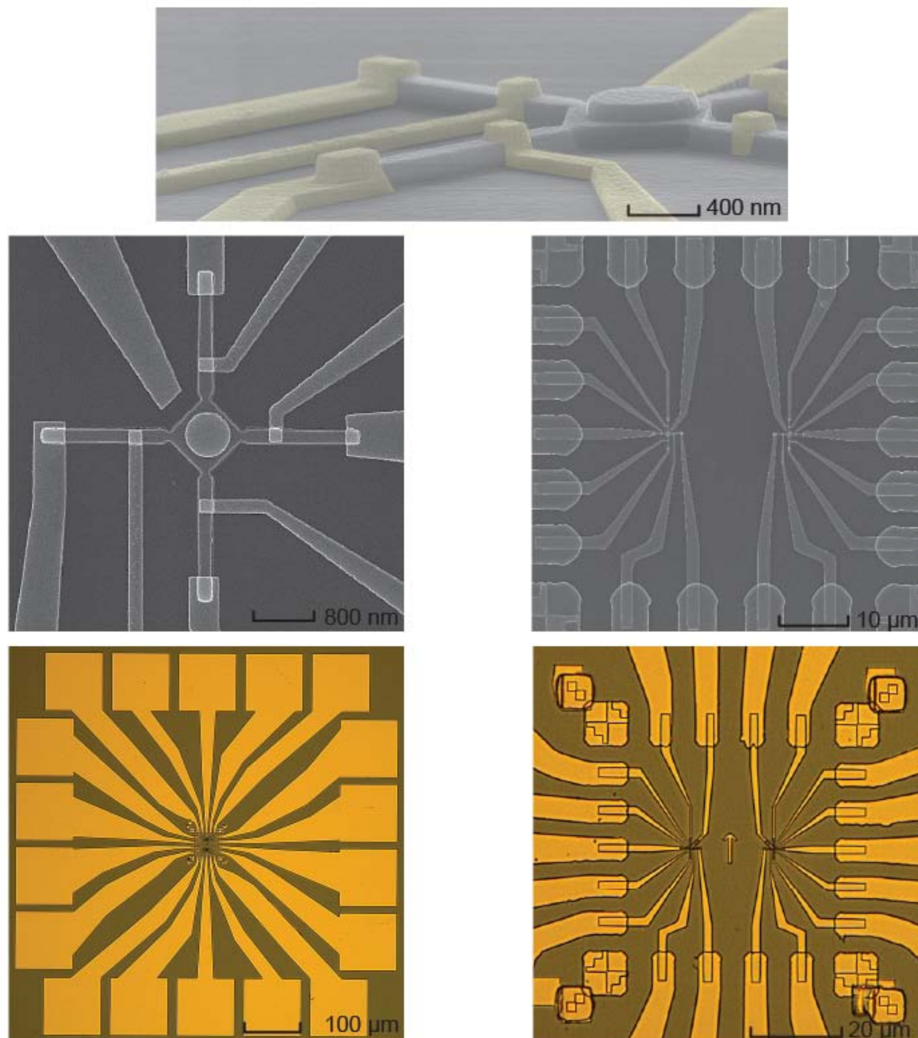

Fig. 6.4: Third and fourth lithography step (EBL 3, OPT 4). A E-beam lithography step defines the current and voltage leads out of Ti/Au. Top: side view of the read-write device after patterning of the Ti/Au contact by e-beam lithography. The leads are colored in yellow for better visibility. Top row: SEM picture of the device with contacts (left) and a view of the 81.92 × 81.92 write-field which includes two read-write devices. The SEM picture is taken after patterning of the bonding pads with an optical lithography step. Bottom row: optical microscope pictures of the structure with bonding pads (left) and a zoomed in version (right).

[Mich 99]. The interplay between chemical and physical etching processes determines the etching properties. The right column in fig. 6.2 shows an example for a process with a beam voltage of 400 V and BCl_3. The width of the bar is 150 nm at the top and 200 nm at the bottom. The difference in width is equivalent to a slope of $\sim 80°$. A pure physical Ar-sputtering process usually yields a slope of $\sim 70°$. The physical etching is still prevalent in the 400 V BCl_3 process. A reason for the slope is the facetation and shrinking of the Ti-mask during the etching process. A second reason is the redeposition of etched particles at the base of the structure. The redeposition can be avoided with a higher BCl_3 gas flow, because the BCl_3 gas reacts with the desorbed particles and creates volatile compounds. A SEM figure of an optimized process and a straight etching profile can be seen in the left column. Here we use a 400 V BCl_3 process to etch trough the in-situ Ti/Au metal with a high physical etching component. A more chemical dominated 80 V BCl_3 process is used to etch through the (Ga,Mn)As into the GaAs substrate. The Ti which is used as an etching mask and defines the structure is also removed during CAIBE step. The etching stops in the in-situ Au layer on top of the structure.

The second e-beam lithography step is used to define the tunnel contact to read-out the magnetization of the central region, fig. 6.3. After exposure and development we evaporate a Ti/Au/Ti layer stack on top of the central region. The top Ti layer serves as an etching mask for a second etching step to remove the remaining in-situ AlOx/Ti/Au layers from the nanobars. Careful Ar-sputtering etches the remaining in-situ Au from the nanobars and stops at the in-situ Ti layer. Because diluted HF does not attach (Ga,Mn)As, we use a HF:H_2O = 1:200 wet chemical etching step to remove the AlOx/Ti layer from the nanobars, left column of fig. 6.3. Before having optimized the described wet chemical etching step with HF we used a 80 V BCl_3 dry etching step with CAIBE to remove the metal on top of the nanobars. The right column of fig. 6.3 shows this as an example of a high etching selectivity of CAIBE. The etching rates for the 80 V BCl_3 process are 36 nm/min for (Ga,Mn)As, 6 nm/min for Au and 2 nm/min for Ti. The SEM shows a rough surface of the (Ga,Mn)As nanobars. The surface roughness appears due to the high selectivity of the 80V BCl_3 process. Gold has a grainy surface after electron beam deposition. The grain structure of the gold (see inset of fig. 6.3 right) is transfered to the Ti-layer during the 80V BCl_3 process. The thereby created surface roughness of the Ti and the quite different etching rates for Ti and (Ga,Mn)As result in a rough etching profile, fig. 6.3 right.

Contacting the nanobars includes an e-beam and an optical lithography step, figure 6.4. The top picture shows a side view of the read-write device including the Ti/Au contact defined by e-beam lithography. For these "e-beam" contacts we utilize a 400 nm thick PMMA resist and evaporate 10 nm Ti and 200 nm Au. Every nanobar is contacted by two leads (colored in yellow for better visibility) with a contact area of 200 $\times$ 200 nm to measure the longitudinal resistance in a two terminal configuration. Figure 6.4 (top column left) shows a top view of the read-write device after patterning of the e-beam contacts. The Au lead, coming from the left upper part of the picture and ending just

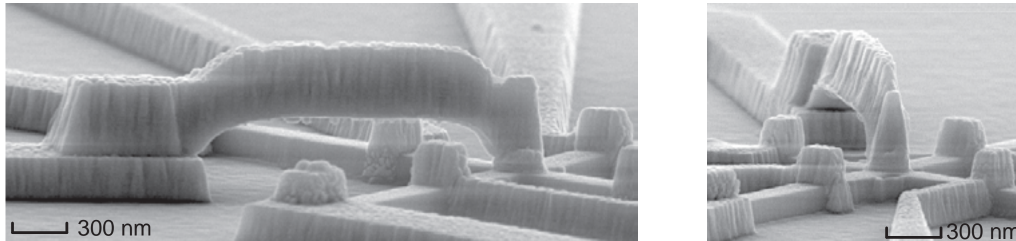

Fig. 6.5: Last e-beam lithography step to pattern down metallic air bridges to contact the TAMR pillar.

before the central region, serves as a lead for the metallic air bridge to contact the TAMR pillar. An additional optical lithography step is used to pattern down the bonding pads. The write field of the electron beam lithography is 81.92 × 81.92 µm and includes two read-write devices, fig. 6.4 top column right. The overlap of the e-beam and optical contacts is also visible in this figure. A last e-beam step is needed to contact the TAMR pillar with a metallic-air bridge (fig. 6.5). During the e-beam exposure of the 1 µm thick PMMA resist we use different beam voltages to expose the span and the post of the metallic-air bridge. A description for the fabrication of such metallic-air bridges can be found in ref. [Borz 04].

6.2 Read-Write Device Design

The aim of the read-write device is to switch the central (Ga,Mn)As region by current induced switching. In (Ga,Mn)As the exact mechanism of current induced switching is not yet understood but demonstrated by Yamanouchi et al. [Yama 04]. Injecting polarized holes with a spin angular momentum into a magnetic region, changes the magnetization direction of the region due to the p-d exchange interaction between localized Mn spins and itinerant holes [Yama 04].

The previous section describes the different lithography steps for processing a read-write device. The width of the nanobars is determined by the work of S. Hümpfner [Hump 07], whereas the exact design of the central region still needs to be optimized. The first demonstration of current induced switching in (Ga,Mn)As is shown in material with a perpendicular to plane magnetic anisotropy [Yama 04]. In this work a Hall bar geometry with a 20 µm wide current channel is used. The current channel exists of three (Ga,Mn)As regions with different layer thicknesses. Due to the different layer thicknesses, the regions have different coercive fields. After an appropriate initializing process the Hall bar consists of three domains with different magnetization directions. The left and the right domain serve as injectors of a spin-polarized current and the central domain

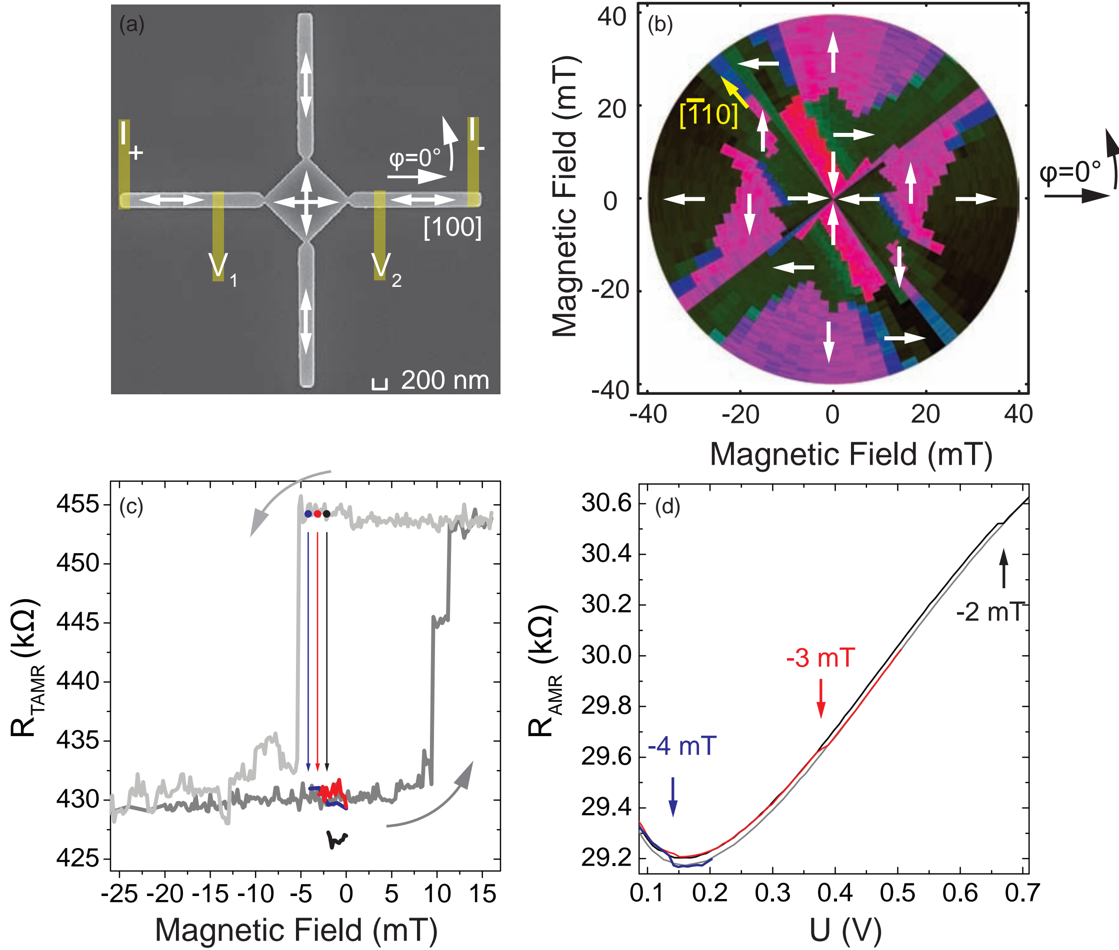

Fig. 6.6: (a) SEM picture of the device with a central square of 800 nm. Possible magnetization configurations of the individual magnetic regions are sketched with white arrows. (b) Resistance polar plot of the TAMR read out of the central square showing a biaxial magnetic anisotropy with a strong uniaxial anisotropy component parallel to the [$\bar{1}$10] crystal axis. (c) TAMR measurements of the central square. Magnetic field sweep starting from applying -300 mT to 16 mT along 0° (dark gray) and back sweep (light gray). Repeating the measurement and stopping the back sweep at -4 mT (blue), -3 mT (red) and -2 mT (black). (d) Current assisted magnetization manipulation by injecting a spin-polarized current from the nanobars along 0° into the central square. The longitudinal AMR resistance is measured as sketched in (a). The magnetization switching from 90° to 180° occurs at different voltages dependent on the applied magnetic field: at 140 mV for -4 mT (blue), at 380 mV for -3 mT and at 670 mV for -2 mT.

switches its magnetization dependent on current direction.

Figure 6.6 shows a first read-write device with a central square of 800 nm and narrow constriction at the transition from nanobars to central square. The white arrows in the SEM picture represent the possible magnetization configurations of the individual magnetic domains. The device consists of four magnetic uniaxial nanobars and a magnetic

biaxial central square. The RPP in fig. 6.6b shows the TAMR measurements of the central square, which has a mainly fourfold symmetry and confirms the magnetic biaxial character. However, the RPP also reveals an enhanced uniaxial anisotropy component parallel to the $[\bar{1}10]$ crystal axis. The white arrows in the RPP are the magnetization directions for the central square at various angles and magnetic field steps. To initialize a magnetic configuration for a current assisted switching experiment we sweep a magnetic field along the [100] crystal axis. A TAMR measurement of the central square with a magnetic field sweep from -300 mT to 16 mT along 0° (dark gray) is shown in fig. 6.6c. At zero field the magnetization is parallel to the 180° direction and the TAMR read-out has a low resistance state. The magnetization switches at ~10 mT by 90° due to a DW parallel to the 90° direction and the TAMR read-out is now in the high resistance state. Stopping the magnetic field at 16 mT and sweeping it back to -300 mT switches the magnetization at -5.2 mT back parallel to the 180° direction (light gray in fig. 6.6c). For the current assisted magnetization procedure we repeat this minorloop and stop the magnetic field on the back sweep at -4 mT. -4 mT is just before the magnetization would change its direction from 90° to 180°. The magnetization of the central square is now parallel to the 90° direction and the magnetization of the [100]-nanobars point along 180°. Driving a spin polarized current along the [100]-nanobars through the central square switches the magnetization of the square along 180°. The change in magnetization can be observed in the TAMR resistance, which is now in its low state. The magnetization remains in the 180° direction when sweeping the magnetic field back to zero (blue in fig. 6.6). While increasing the current the longitudinal resistance R_{AMR} is recorded by the contacts I_+, I_-, V_1 and V_2, fig. 6.6a. The resistance includes parts of the two nanobars, two constrictions and the central square. As soon as the current overcomes a certain threshold the magnetization of the central square switches. This change results not only in a TAMR resistance change, but also in the longitudinal AMR resistance decrease, fig. 6.6d. R_{AMR} decreases, because the angle between current and magnetization of the square changes from perpendicular to parallel. With an applied field of -4 mT the magnetization direction changes at a voltage of 140 mV and AMR resistance changes to its low state. The back sweep of the voltage (low resistance state) is also shown in the figure (light gray). We repeat the procedure two more times and instead of stopping the magnetic field at -4 mT we stop at -3 mT (red) and -2 mT (black). By lowering the auxiliary field the current threshold increases and the magnetization switches at 380 mV and 670 mV for an applied field of -3 mT and -2 mT, respectively. The current density in the central square at the magnetization reversal with an applied field of -2 mT is $J = \frac{I}{A} = \frac{21\mu A}{800nm \times 70nm} \sim 4 \times 10^4 Acm^{-2}$. The critical threshold for the current density decreases with increasing applied magnetic field. Because of a missing direction dependence, the reason for the magnetization reversal, shown in the above experiment, can not be unambiguously attributed to a pure spin-torque mechanism. One can speculate that slight local heating of the (Ga,Mn)As material changes the magnetic anisotropies and thus reduces the coercive field. The applied magnetic field could change the magnetization direction due to lower switching fields.

To rule out a pure heating mechanism the magnetization has to show a dependence on current direction.

The current distribution in the central square of the device design shown in fig. 6.6 is inhomogeneous, because the central square has four times the width of a nanobar. The constriction at the transition from nanobar to central square could also act as a heat spot, where the spin information of the injected carriers are lost. The Hall bar geometry of ref. [Yama 04] has a more homogeneous current distribution, because the different magnetic regions have identical width of 20 µm and a height of 25 nm, 18 nm and 22nm. A homogeneous current distribution in our case results in a central region with a width of 200 nm. Figure 6.7a shows the top view of a read-write device with a central region having a diameter of 300 nm. For better visibility of the design the SEM picture is taken before patterning of the metallic air bridge. A side view of the device is shown in figure 6.7b including the metallic air bridge. The design is almost a pure cross and the nanobars are directly connected to the central region without any notches or constrictions separating the nanobars from the central region.

Figure 6.7c shows the angular dependence of the TAMR resistance of the central region in a 300 mT saturation φ-scan. The TAMR resistance at 300 mT is 235 $k\Omega$ along $\varphi = 0°$ compared to 214 $k\Omega$ along $\varphi = 90°$. Hence, the two directions have different resistance values and thus are distinguishable. The tunneling resistance has its maximum along $\varphi = 130°$ with a value of 258 $k\Omega$. TAMR measurements for magnetic field sweeps from -300 mT to 300 mT every 30° are shown in fig. 6.7d. Sweeping the magnetic field along the 0° direction (black), the TAMR resistance remains at a constant value of R $\sim$ 235 $k\Omega$. Hence, the magnetization for this field sweep direction is either along 180° for negative fields or along 0°. The magnetization reversal process from 180° to 0° happens in a single step and is not visible in the TAMR measurement. Applying -300 mT in the 90° (green) direction forces the magnetization along 270°, which is an easy axes for unpatterned (Ga,Mn)As. While sweeping the magnetic field back to zero the resistance changes from 214 $k\Omega$ to 235 $k\Omega$ at -15 mT. The change in resistance happens before zero field and denotes a magnetization reversal by 90° to the 0° direction. The [010] crystal direction is no longer a direction of easy magnetization. As soon as the applied positive field along 90° is large enough, the magnetization of the central regions will be parallel to the field direction. The material of the central disk has a uniaxial magnetic anisotropy with the easy axes along [100] and lost its biaxial character of the host material. The single resistance state of 235 $k\Omega$ at zero field is one signature of a uniaxial magnetic anisotropy. Anisotropic strain relaxation can not be the reason of the uniaxial magnetic character, because the nanobars prevent the central region to relax the growth strain along [100] and [010]. Whereas strain relaxation is possible along [110] and [$\bar{1}$10] crystal axes. In the case of fig. 6.7 the central region rather follows the magnetization of the nanobars which are aligned along [100]. The nanobars induce its magnetic properties onto the central region. A second device of this geometry shows similar results with the exception that the central

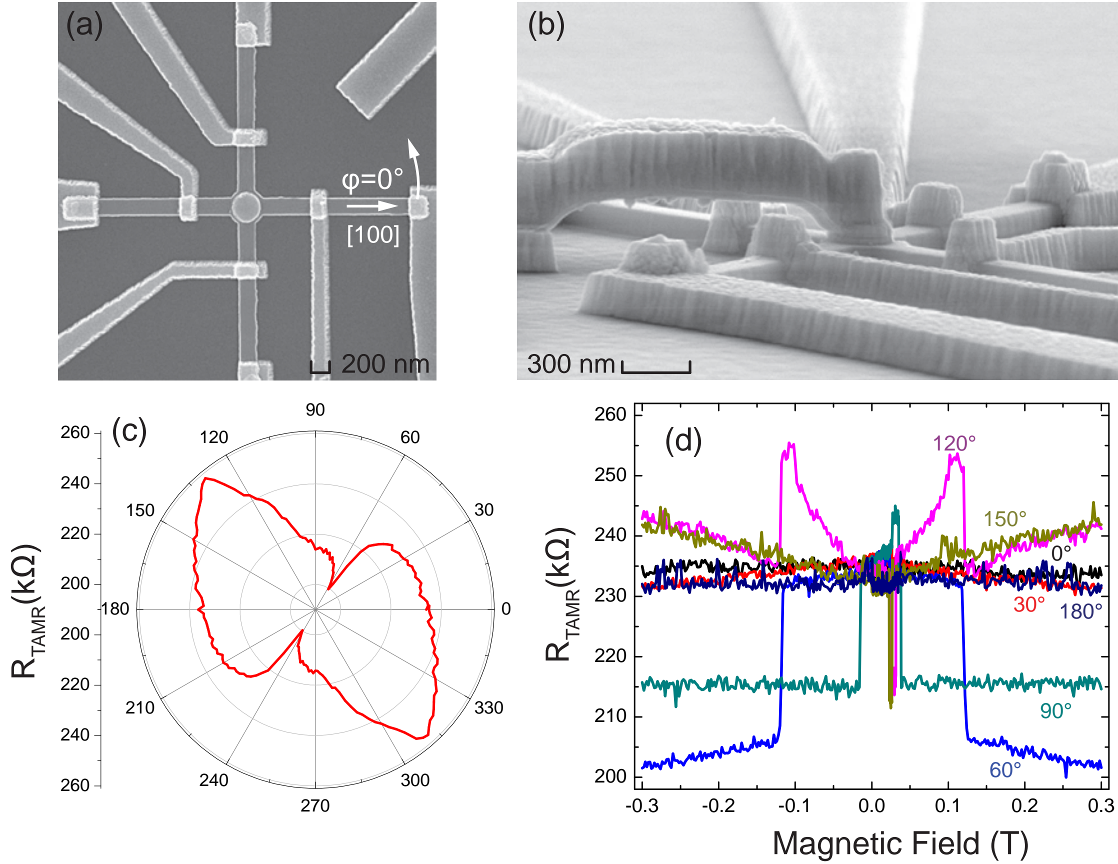

Fig. 6.7: a) Top view of the device. The central disk has a diameter of 350 nm. The nanobars are directly contacted to the central disk without any notches or constrictions. b) Side view of the device. c) Angular dependence of the TAMR resistance at 10 mV bias voltage of the central region in a 300 mT saturation φ-scan. d) TAMR measurements in a three terminal configuration for the tunnel pillar every $\varphi = \Delta 30°$.

region follows the nanobars along [010]. Imperfections in the lithography make one or the other direction predominant and force the magnetization of the central disk to follow the magnetization of the nanobars.

The goal of our design is four uniaxial nanobars and a magnetic biaxial central region. In the following experiment the dimensions of the central region will be increased compared to the device of fig. 6.7 to achieve a magnetic biaxial anisotropy of the central region. Additionally we pattern small notches at the transition from the nanobars to the central disk to support the pinning of a domain wall at the end of the nanobars.

6.3 Read-Write Device Operation

In this section we report the realization of a read-write device out of the ferromagnetic semiconductor (Ga,Mn)As as the first step to fundamentally new information processing paradigm. Writing the magnetic state is achieved by current-induced switching and read-out of the state is done by the means of the tunneling anisotropic magneto resistance (TAMR) effect. This one bit demonstrator device can be used to design a electrically programmable memory and logic device.

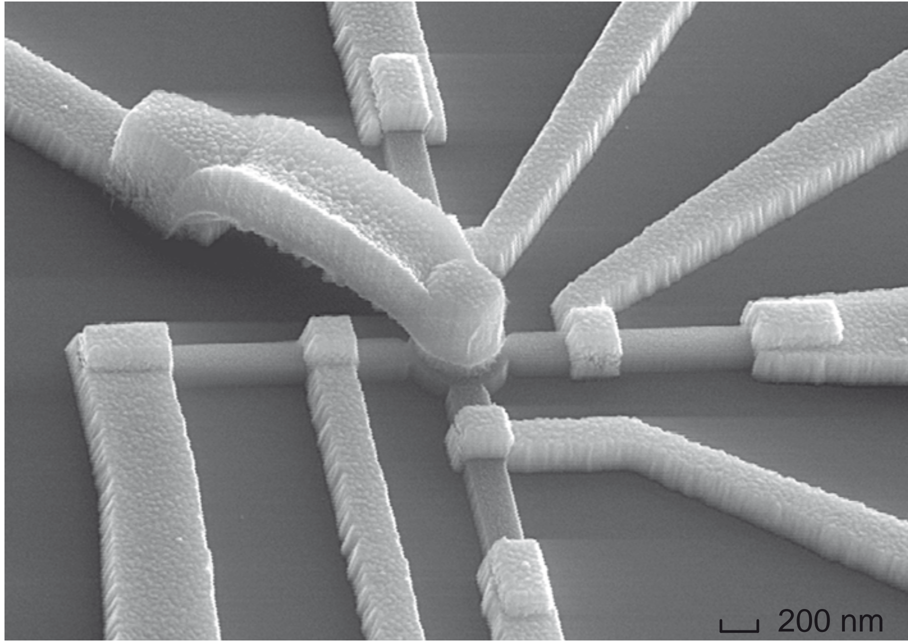

Fig. 6.8: SEM picture of the read-write device. A metallic air bridge out of Gold contacts the central disk. Each of the four nanobars connected to the central disk is contacted by two Ti/Au wires. The central disk has a diameter of 650 nm and small notches are at the transition from nanobars to central disk which serve to pin down a domain wall.

Figure 6.8 shows the read-write device. Our structure consists of four nanobars which are connected to a circular center region. The nanobars are 200 nm wide and 2 µm long and the central disk has a diameter of 650 nm. The Alox/Ti/Au layer on top of the 650 nm central disk remains on the structure and together with the metallic air bridge acts as a read-out tunnel contact. The tunnel barrier consist of $3\times$ 0.9 nm AlOx which is deposited in a electron beam evaporation chamber. Small notches are patterned at the transition from the nanobars to the central disk and serve to pin down domain walls. For a more detailed description of the device fabrication see section 6.1.

Thin films of unpatterened compressively strained (Ga,Mn)As exhibit an in-plane biaxial magnetic anisotropy at low temperatures. The bars connected to the central disk are aligned with their length parallel to the magnetic easy axes of the bulk. As a result of patterning induced anisotropic strain relaxation [Hump 07] the lattice can relax the strain

perpendicular to the long axis of the nanobar. Fig. 6.9b shows a view on a nanobar from the front face. The formerly compressively strained (Ga,Mn)As can relax after etching and thus change the lattice constant in the direction perpendicular to the long axis of the bar. The bar retains its strained character along the long axis of the bar. The lattice and the magnetic anisotropies are coupled via the spin-orbit coupling and due to the change in lattice parameters the magnetic anisotropy changes. As a rule of thumb for (Ga,Mn)As we can state, that the direction with the shortest lattice constant is the direction of easy magnetization. Each bar has a uniaxial magnetic easy axis parallel to its long axis, making the bars appropriate for sources of current induced switching of the central disk.

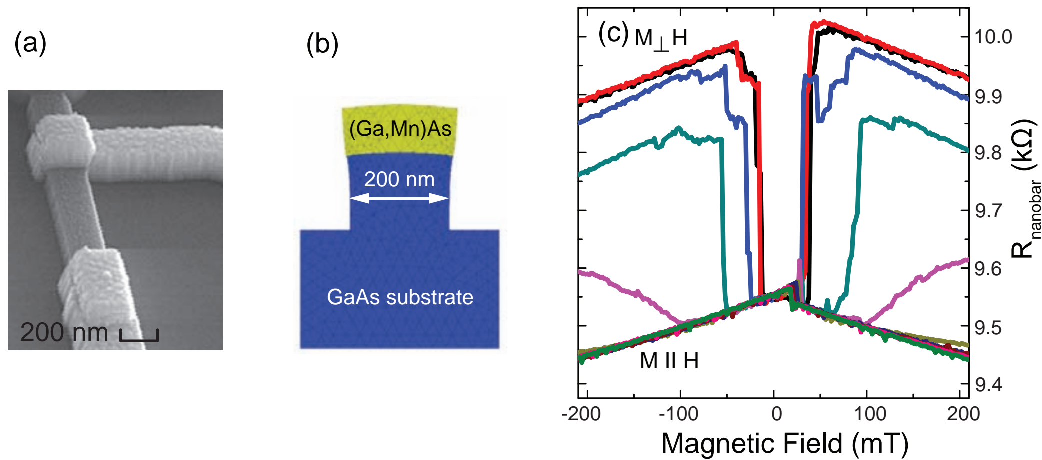

Fig. 6.9: a) SEM picture of a single nanobar with two Ti/Au contacts for a two terminal longitudinal resistance measurements. b) Sketch of the strain relaxation of a nanobar b) AMR measurements of one of the nanobars which shows a uniaxial magnetic anisotropy. Magnetic field sweeps for various in-plane angles in steps of $\Delta\varphi = 10°$ from along the long axis of the nanobar (M||H) to perpendicular to it (M⊥H).

The magnetic anisotropy of each nanobar can be measured in a two terminal configuration. The change in longitudinal resistance in response to an external magnetic field follows the normal AMR sign for (Ga,Mn)As, which shows a typical $cos^2\vartheta$-dependence where ϑ denotes the angle between magnetization and current. In (Ga,Mn)As, the resistance for current perpendicular to the magnetization is larger than for current parallel to the magnetization. Fig. 6.9c shows representative magneto resistance measurements on one bar (fig. 6.9a) for field sweeps along various in-plane directions φ referenced to the [100] crystal direction. Such a measurement on a bulk piece of (Ga,Mn)As would show both high and low resistance values at B = 0 mT, as the magnetization would relax to either of the biaxial easy axes depending on the orientation of the magnetic field sweep. In contrast, the resistance of a nanobar at zero magnetic field is always in the low resistance state and independent of the field sweep direction, indicating that, in the absence of an external field, magnetization and current are always parallel to the long axis of the nanobar. The nanobars thus have a uniaxial magnetic anisotropy with its magnetic easy

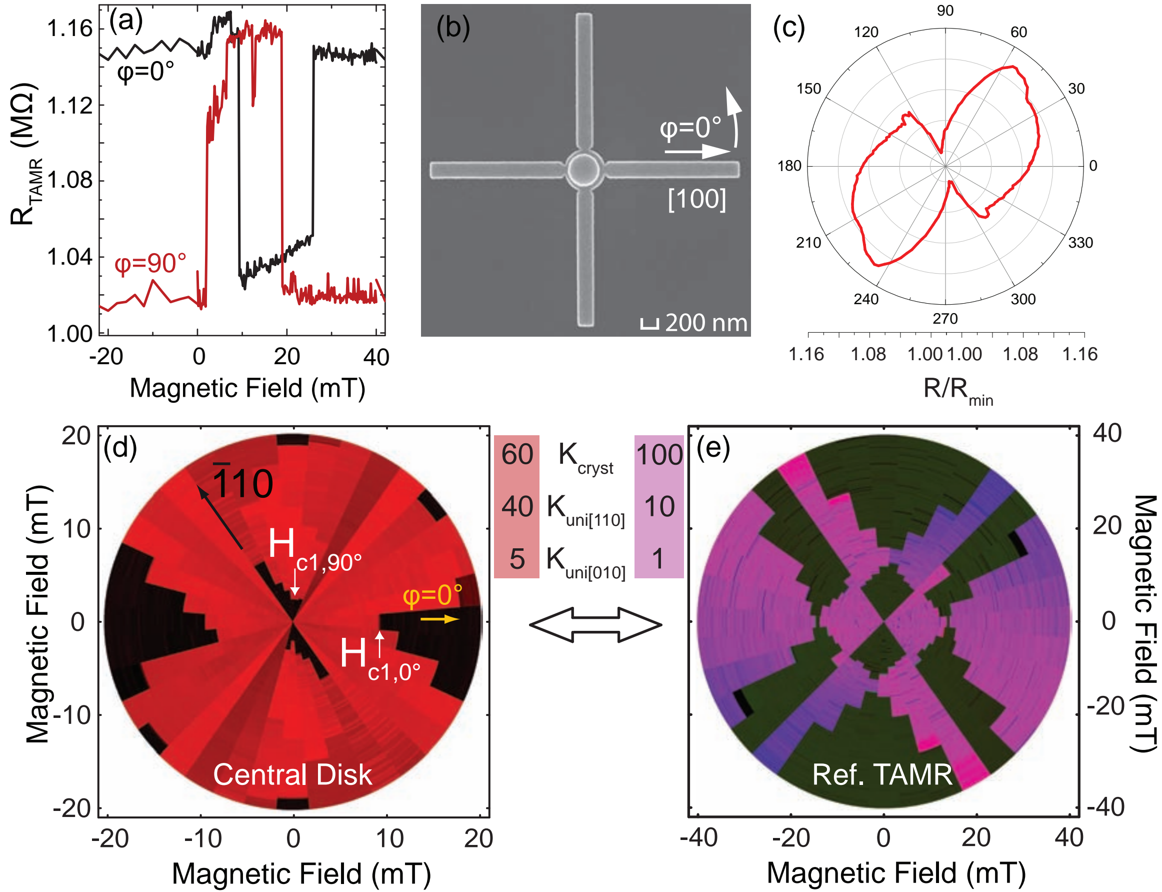

Fig. 6.10: a) Three terminal TAMR measurements of the central disk parallel to the $\varphi = 0°$ and $\varphi = 90°$ direction. b) SEM picture of the device showing small notches at the transition from central disk to nanobar to pin a domain wall. c) TAMR resistance as a function of angle in an applied field of 300mT. d) Tunneling Anisotropic Magneto Resistance (TAMR) measurements of the central disk summarized in a Polar Plot. e) Reference TAMR measurement of a 260 nm pillar on unpatterned (Ga,Mn)As.

axes parallel to the bar.

The relatively large central disk is less influenced by strain relaxation and retains the mainly biaxial anisotropic character of the bulk material. To obtain exact information about the magnetic anisotropies of the central disk we make use of the TAMR effect. The TAMR resistance for this pillar is high for magnetization along [100] ($\varphi = 0°$) and low for magnetization parallel to [010] crystal direction ($\varphi = 90°$), fig. 6.10c. Fig. 6.10a (black) shows a TAMR measurement along the $\varphi = 0°$ direction. The measurement starts with applying -300 mT in the $\varphi = 0°$ direction and sweeping the magnetic field back to zero. The magnetization at zero field points along $\varphi = 180°$. Sweeping the field to positive values, the magnetization switches at 9 mT from $\varphi = 180°$ to $\varphi = 90°$ and reverses its direction to $\varphi = 0°$ at 26 mT. To map the full anisotropy of the central disk, we

compile the positive field half of the TAMR-measurements for various directions into a resistance polar plot, shown in fig. 6.10d. Red denotes high and black low resistance. The magnetic field increases with the radius in the RPP and high and low (red and black) resistances exist at zero or small positive fields. For perfectly biaxial material the switching field H_{c1} (where the magnetization first reverses its direction by $\sim 90°$) along each easy axes is equivalent. Fig. 6.10e shows a reference RPP for TAMR measurements on an unpatterned (Ga,Mn)As layer. In (Ga,Mn)As, secondary anisotropy contributions cause the two H_{c1} to differ by typically a few percent [Goul 08], fig. 6.10d. As can be seen in fig. 6.10a, the switching fields H_{c1} in our disk are different for $\varphi = 0°$ and $\varphi = 90°$ ($H_{c1,0°}$= 9.4 mT, $H_{c1,90°}$ = 2.0 mT) reflecting a small additional magnetic anisotropy between the two easy axes resulting from strain and patterning. The usual ratio for the anisotropy components in (Ga,Mn)As is 100:10:1 for K_{cryst} : $K_{uni[\bar{1}10]}$: $K_{uni[100]}$. Reading the anisotropy components from the resistance polar plot gives a ratio of 60:40:5 = K_{cryst} : $K_{uni[\bar{1}10]}$: $K_{uni[100]}$ which is also confirmed by a RPP simulation.

Having characterized all the individual elements of the structure, we continue with its device operation. To prepare an initial state, we apply a magnetic field $\mu_0 H$ of 300 mT along the $\varphi = 120°$ direction and sweep it back to 0 mT. As the external field is removed, the device relaxes to a state where (Fig. 6.11c) the magnetization of every nanobar is aligned along its respective long axis. Because it is the biaxial easy axis nearest to the angle of the preparation field, the magnetization of the central disk relaxes to point along 90° which corresponds to the low resistance state in the TAMR read out (Fig. 6.11b). We define the device to be in its logical "0" state when the magnetization of the central disk points along 90°, and to be "1" when it points along the 180° direction. To compensate the small magnetic asymmetry of the central disk mentioned above, we apply a static magnetic field of $\mu_0 H = 7.8$ mT along 90°.

Electrical control of the device is then implemented by making use of current induced switching [Yama 04, Goul 06, Wund 07, Ohno 08]. When a current flows through one of the bars with fixed magnetization, the current carrying holes acquire a polarization, and thus a defined angular momentum. As they pass from the bars into the relatively free disk, the interaction of these carriers with the local Mn moments imparts a torque onto the latter, and for currents above a threshold value, causes the moment in the central region to align to that of the bars from where the current is flowing.

By choosing the appropriate bars as current source and drain, the magnetization state in our disk can thus be fully controlled. The device is written into a "1"-state (high resistance state) by applying a current with a density of $1 \times 10^5 Acm^{-2}$ between contacts A and C of Fig. 6.11c, the magnetization of the central disk switches from the 90° to the 180° direction, which results in a high resistance signal for the TAMR read-out contact (Fig. 6.11a). The central disk is switched back by applying a current between contacts B and D. This current-induced switching is clearly detected in the TAMR read-out signal (Fig. 6.11a). The information is written fully electrically and the information storage in the disk is non-volatile. The current density, $1 \times 10^5 Acm^{-2}$, is comparable to the current

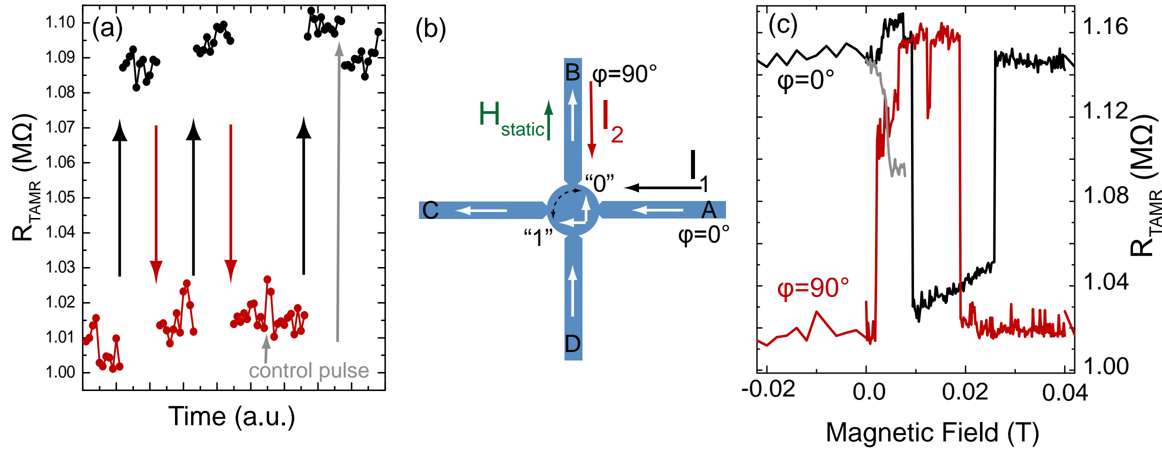

Fig. 6.11: a) Switching the magnetization of the central disk due to an electrical current from the 90° to 180° direction and back. The device can be written into a "1" (180°) by applying a current along 180°. For switching back the magnetization in the "0" state one applies the same current in the 90° direction. Having prepared the "0" state and applying a current in the 90° direction, the magnetization of the central disk does not change (control pulse). b) Sketch of the experimental configuration. c) Full TAMR traces for the central disk (90° red 0° black) and back sweep of the static magnetic field to zero after switching of the magnetization (light gray).

density of ref. [Yama 04] and one to two orders of magnitude lower than the densities needed in metallic memory elements. We observe that the switching is better controlled when the current is delivered as a series of 10 pulses, each 40 µs long, during a 5 s time frame. The TAMR read-out measurement is done with a non-perturbative current of ~ 1 nA which does not change the magnetic state of the central disk.

To confirm that the switching of the disk is indeed due to the spin polarization of the current, we prepare again the "0" resistance state. Applying a current along the 90° direction (contacts B and D) does not change the magnetization of the central disk (see control pulse in Fig. 6.11). Applying the current in the 180° direction (contacts A and C) switches the central disk to the high resistance state. We have performed similar control experiments for the 180° direction. The clear outcome of our control experiments is that the switching of the central disk is indeed due to the spin polarization of the current and not due to heating effects, and that we can use current induced switching to control an electrically programmable logic architecture. As a final issue we note that the switching amplitude due to the current is just over 60% of the full TAMR. This is presumably due to the fact that, when electrically switched, the central disk does not behave as a pure macro spin but allows the formation of domains due to small geometrical imperfections at its edges. To further confirm that the change in resistance has its origin in a switch of the magnetization states, we sweep the static magnetic field back to zero (light gray curve in Fig. 6.11b). This shows that the part of the domain which is not switched was pinned by the applied static magnetic field, and that as soon as we sweep the field back to zero, this part of the disk aligns with the electrically switched domain. By sweeping back

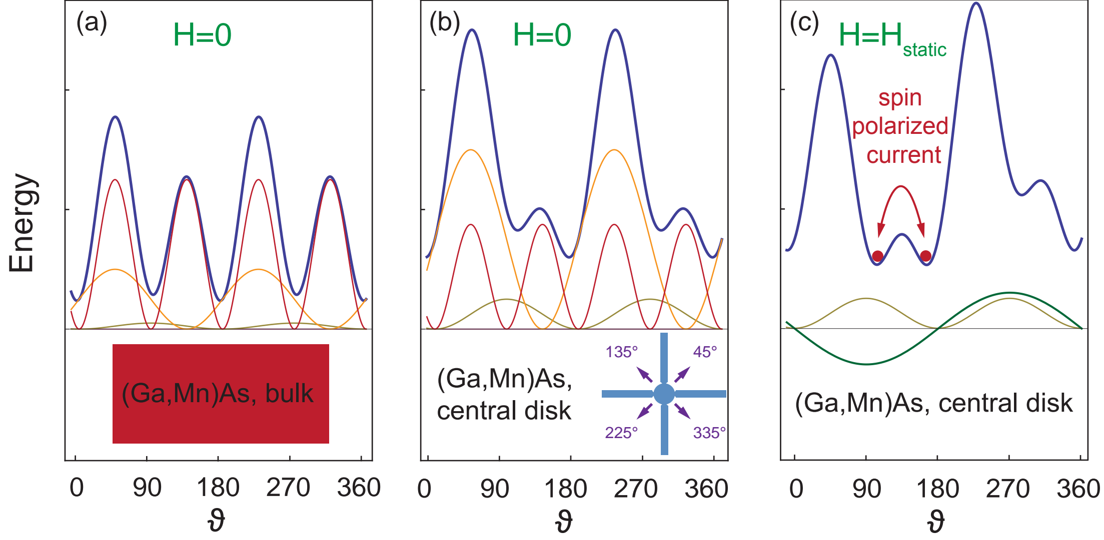

Fig. 6.12: a) Energy potential (blue) of an unpatterned (Ga,Mn)As layer with its anisotropy components K_{cryst} (red), $K_{uni[\bar{1}10]}$ (orange) and $K_{uni[100]}$ (brown) and their typical ratio of 100:10:1. b) Energy potential of the central disk with a changed ratio of the anisotropy components due to imperfections of the lithography and strain relaxation at the edges of the disk. c) Energy potential of the central disk with an applied auxiliary field H_{static} along the 90° direction to equalize the minima along 180° and 90°.

the magnetic field to 300 mT along 180° the magnetization remains in its position which is clear evidence that the electric current caused a magnetization reorientation of the disk.

Auxiliary Field

Now we comment on the auxiliary field H_{static}, which we apply during the read-write device operation. For unpatterned (Ga,Mn)As the total anisotropy energy is shown in fig. 6.12a (blue) and consists of K_{cryst} (red), $K_{uni[\bar{1}10]}$ (orange) and $K_{uni[100]}$ (brown) as described in section 2.2. Patterning of nanobars with a width of 200 nm gives the material a magnetic uniaxial character due to anisotropic strain relaxation. Patterning influences the magnetic anisotropies of the material noticeable for dimensions below ∼1 µm, e.g. bars with a width of 1 µm already have an increased uniaxial component along the long axis of the bar. As mentioned earlier the ratio of the anisotropy components changed from 100:10:1 for unpatterned (Ga,Mn)As to 60:40:5 for the central disk. Figure 6.12b shows the warped anisotropy energy potential for the central disk. The enhanced single components are also shown. The energy potential still has four minima and thus four easy magnetization directions. Compared to the energy potential of the unpatterned (Ga,Mn)As the energy potential of the central disk is distorted. As described in section 6.2 imperfections in the lithography induce an enhanced uniaxial anisotropy component along [100] (0°) onto the central disk. A second reason is anisotropic strain relaxation of the central disk. The central disk has a diameter of 650 nm thus in a regime where strain

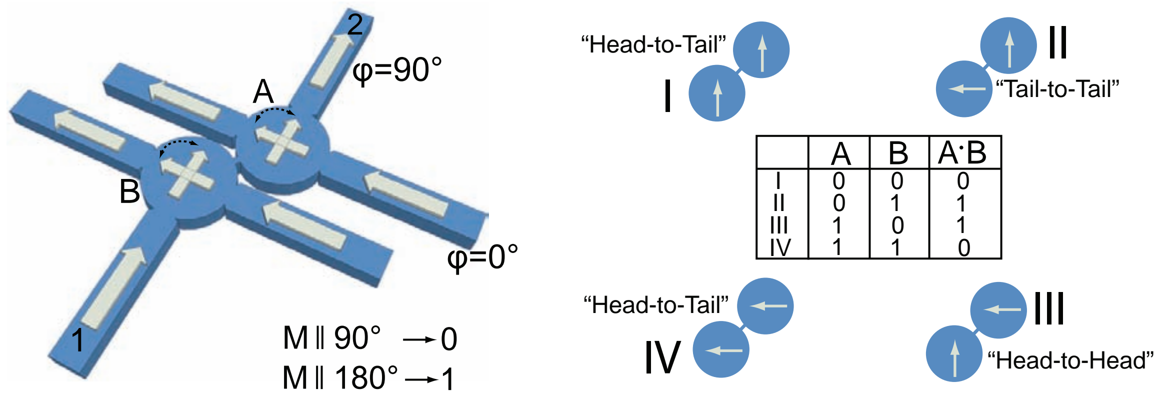

	A	B	A·B
I	0	0	0
II	0	1	1
III	1	0	1
IV	1	1	0

Fig. 6.13: Proposed programmable logic element. The two central disks serve as two memory bits as well as two input bits of the logic device. The constriction between the two central disks is the key to reading-out the result. The resistance from contact 1 to 2 will be dominated by the constriction which is dependent on the magnetization configurations of the input bits. In this configuration the input bits have four possible magnetization states: twice "Head-to-Tail", "Head-to-Head", "Tail-to-Tail". Truth table as it could be programmed as an exclusive OR (A XOR B) gate.

relaxation is not negligible. The lattice of the central disk has the opportunity to relax its strain in the 45°, 135°, 225° and 315° directions, inset in fig. 6.12b, whereas the lattice is not able to strain relax along 0°, 90°, 180° and 270°. The nanobars are along the latter direction and prevent the lattice to relax its strain.

The minima along the switching directions (90° and 180°) of the central disk have different energy values. To symmetrize the 90° and the 180° directions we apply a small field H_{static} along 90° during the read-write operation. The magnetization of the central disk can be switched forth and back with a spin polarized current from the respective nanobars overcoming the energy barrier between the respective directions. The magnetization is implied by the red dot in fig. 6.12c.

As a first step towards a realization of a fully a programmable logic device is described in ref. [Papp 07c] as an ultra-compact (Ga,Mn)As based memory cell. In that work, the authors made use of lithographically engineered strain relaxation to produce a structure comprised of two nanobars with mutually orthogonal uniaxial easy axes, connected by a narrow constriction. Measurements showed that the resistance of the constriction depends on the relative orientation of the magnetization in the two bars. While very small, the functionality of the memory cell was dictated by its lithographic layout. We will now describe how a universal gate can be fabricated in (Ga,Mn)As by adding bulk biaxial anisotropy and writing of the information by electrical means to the initial concept.

Extending our read-write device from Fig. 6.8 to two central disks and connecting the two disks with a small constriction creates a fully electrically programmable logic and storage device. The blue shape in Fig. 6.13 depicts the design of such a logic device. Two central disks act as non-volatile storage units and at the same time represent the input of

the two bit logic operation. The 'bit value' is represented by the in-plane magnetization direction of each disk. The element is initialized by applying a field in a specific direction and sweeping it back to zero. For example, for initializing along 120°, the resulting magnetic orientation of the bars is as given by white arrows in Fig. 6.13 and the initial magnetization of both central disks points in the 90° direction. During device operation, the configuration of each central disk can be changed into two possible magnetization directions pointing either in the 180° or 90° direction. A current flowing from a given bar into the disk switches the magnetization of the disk parallel to the magnetization of that bar. The constriction between the two central disks is the key to reading-out the result. As long as the connection is sufficiently narrow, the resistance between contacts 1 and 2 in Fig. 6.13 will be dominated by this constriction. The resistance of this constriction depends on the relative magnetization states of the central disks [Papp 07c]. If the magnetization of both disks point either towards or away from the constriction we call the configuration Head-to-Head or Tail-to-Tail, respectively as depicted in the insets of Fig. 6.13. The magnetic field lines caused by the magnetization of the disks are perpendicular to the current direction in the constriction. On the other hand, if the magnetization of the disks is in series (magnetization of one disk pointing toward the constriction and the other disk pointing away from the constriction, Head-to-Tail) the magnetic field lines in the constriction are parallel to the current direction. Because of an effect akin to anisotropic magnetoresistance (AMR), and associated with a magnetization dependence of the impurity wave functions in (Ga,Mn)As [Papp 07c, Schm 07], the resistance of the constriction depends on the angle between the field lines and the current through the constriction allowing to determine the relative magnetization states of the two bits. The output of the logic operation is defined as "1", if the magnetic configuration of the disks is Head-to-Head or Tail-to-Tail and is "0", if the states are in Head-to-Tail configuration.

For e.g. an exclusive OR (A XOR B) logic element we define the magnetization direction of the disks pointing in 90° as "1" and pointing along 180° as "0". For the initial configuration both disks are in the "1" state and the magnetic configuration of the output is Head-to-Tail and therefore "0". A switching current through disk "A" along 180° switches the magnetization of disk "A" along 180° changing the "A" input to "0". The relative magnetization is now Head-to-Head, as symbolized by configuration III in Fig. 6.13 and the XOR logic operation yields "1" as an output (III: 1 XOR 0 = 1). If disk B is also switched to the 180° direction the device has again Head-to-Tail configuration and therefore yields "0" as output. The complete truth table is given in Fig. 6.13.

The present results for electrically writing information into the read-write device, combined with the constriction read-out results of ref. [Papp 07c], provide all essential elements for the realization of our programmable logic element. In closing we stress that the functionality of the programmable logic scheme presented here can be straightforwardly extended to produce multi-purpose functional elements [Papp 07b], where the given geometry can be used as various different computational elements depending on the number of input bits and the chosen electrical addressing. Such a paradigm has technological

advantages as it allows for the generation of entire computational circuits consisting of multiple identical elements, which can thus be easily, rapidly and cheaply produced by parallel lithography.

Chapter 7

Domain Wall Resistance in (Ga,Mn)As

The RW device design offers also the possibility to measure the resistance of domain walls (DWs), which exist for the various magnetization configurations. A domain wall separates two ferromagnetic regions with different magnetization orientation. The magnetization in a domain wall changes continuous from the initial to the final magnetization state and the most common sorts of DWs are Bloch walls or Néel walls. In a Bloch wall the magnetization rotates through the plane of the wall, whereas for a Néel wall the magnetization rotates in the plane of the DW. The configurations of the magnetic moments for a Néel and a Bloch wall are shown in fig. 7.1. The origin, which causes a DW resistance can be threefold. The extrinsic contribution stems from an inhomogeneous current distribution due to opposite polarity of the Hall electric field on the two sides of the DW [Part 74]. The intrinsic part originates from domain wall scattering analogues to the giant magneto resistance in structures with collinear magnetic alignments [Levy 97] and the third part is the AMR resistance of the DW. When a holes or electrons carrying a magnetic moment propagate trough the domain wall region (II), and the local magnetic moments within the region change the orientation of the magnetic moments, the carriers perceive an extra resistance due to the change of magnetization orientation in the domain wall region with respect to the current direction. Our device design does not allow to distinguish among the different contributions. On going discussion about domain wall resistances and the DW-displacement in (Ga,Mn)As show, that the relative importance of the different terms in (Ga,Mn)As still need to be clarified [Tang 04, Chib 06].

The RW device is ideal to set up different magnetization configurations and thus create domain walls at the transition from the nanobars to the central region. Our RW device design is similar to that reported in [Rust 03] with the difference, that our central magnetic region has a biaxial magnetic anisotropy. The virtual contacts in fig. 7.2a are used to measure the resistance including the DW-resistance. It consists of the resistance of the central square, parts of the two used nanobars and the constriction, which serves as a pinning center of the domain wall. The resistance is determined by performing a

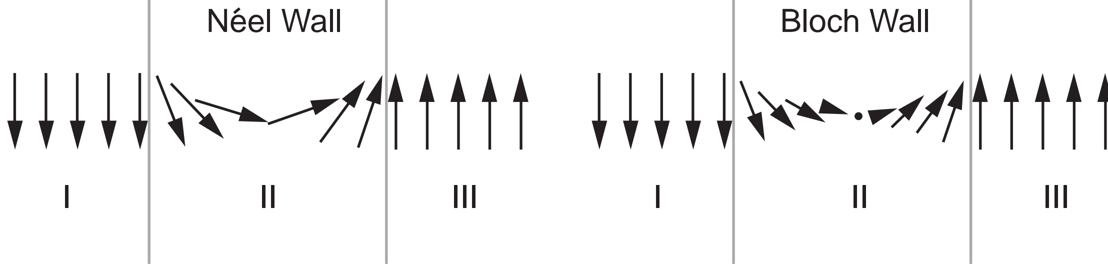

Fig. 7.1: Configuration of the magnetic moments for a Néel- and Bloch domain wall. In a Bloch wall the magnetization rotates through the plane of the wall and for a Néel wall the magnetization rotates while staying in the plane of the wall.

four terminal IV measurement from ±100 mV. The constrictions are wide enough for a linear IV-dependence as expected for metallic transport in (Ga,Mn)As, fig. 7.2f . The magnetization direction of the individual nanobars are determined by their two terminal AMR resistance, whereas the magnetization of the central square is read-out by a TAMR contact. The TAMR is in its low resistance state for the magnetization along the [100] crystal axis. Initializing the magnetic configuration by applying a -300 mT magnetic field parallel to the [100] direction and sweeping it back to zero results in a magnetization configuration where the magnetization of the two nanobars and the central square are parallel to the 180° direction, as shown in fig. 7.2a. The resistance in this magnetization configuration is (29320±11) Ω and no domain walls exist along the current path, fig. 7.2f.

To generate a DW at the constriction, we sweep a magnetic field to 16 mT along 0° and back to zero. The magnetization of the central square changes its direction at ∼10 mT to the 90° direction, which can be seen in the change of the TAMR resistance from 425 kΩ to 450 kΩ. The magnetization of the nanobars remains unchanged. This configuration (fig. 7.2b) includes two 90° domain walls and the four terminal resistance increases by (106±19) Ω to (29426±16) Ω. Sweeping the magnetic field to 22 mT along 0° switches the magnetization of the square along 180° and creates an anti parallel magnetization configuration with two 180° domain walls, fig. 7.2c. The four terminal resistance goes to (29536±17) Ω. Applying a 40 mT magnetic field aligns the magnetization of the different domains along 0° and generates the the parallel configuration again. The four terminal resistance reaches the initial value.

The difference in resistance of parallel and anti-parallel magnetization configuration is (216±20) Ω and stems from the two domain walls at the constrictions. The DW is most likely expanded within the dimensions of the constriction, which is ∼40×40 nm. Thus the resistance of our 180° DW with a dimension of ∼ 40×40 nm is $R_{DW,180°}$ ∼ (108±10) Ω. The difference in resistance for the 90° magnetization configuration (fig. 7.2b) is ∼ (106±19) Ω. The resistance value in the 90° configuration additionally includes the change in AMR resistance of the central square. The change of longitudinal resistance for the 180° and 90° can not be measured in the existing configuration. An estimate for ΔAMR

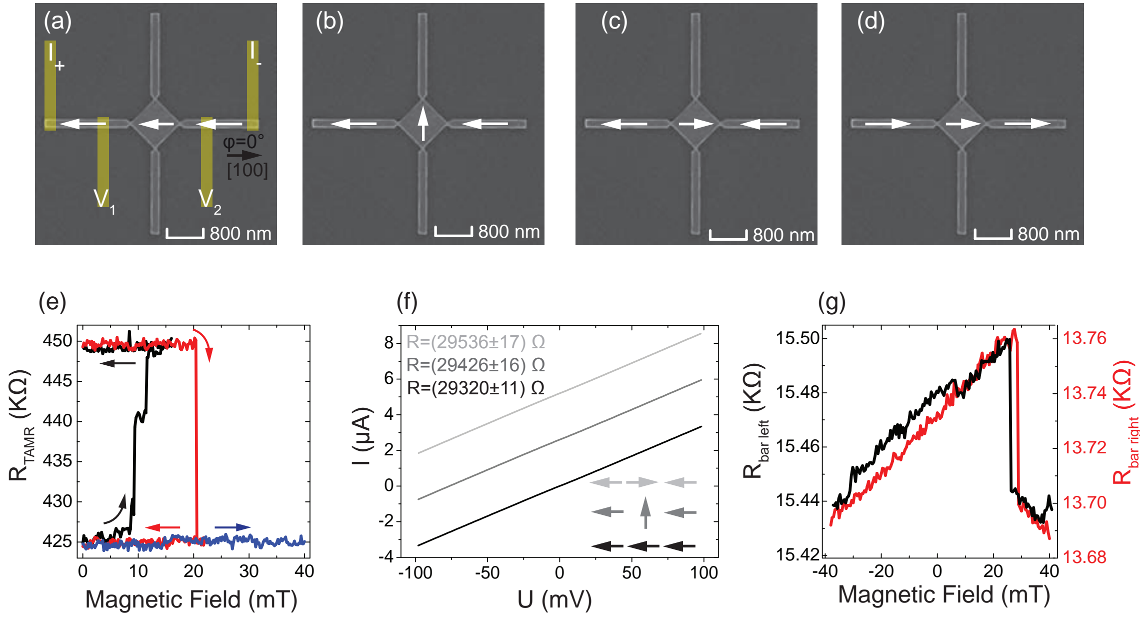

Fig. 7.2: (a) SEM of the RW-device with virtual contacts showing the measurement configuration. The dimensions of the constriction between nanobar and central square is ∼40×40 nm. (a-d) Possible magnetization configurations for a magnetic field sweep along 0°. The white arrows show the magnetization direction of the different domains. (e) TAMR read-out of the central square for MR measurements parallel to [100] crystal direction. Sweeping the magnetic field until 16 mT (black), 22 mT (red), 40 mT (blue) and back to zero field at any time after having prepared the initial state shown in (a). (f) Linear IV measurement in a four terminal configuration as shown in (a) and resistances of the different magnetization configurations. (g) Resistance of the two nanobars along [100] for a field sweep along 0°. The magnetization of both nanobars reverse their direction by 180° at ∼27 mT.

of the central square is 3% of 1 kΩ/square (for a 70 nm layer) results in (30±10) Ω. This yields $2R_{DW,90°} + \Delta R_{AMR}$ = (106±19) Ω and thus $R_{DW,90°}$ = (38±21) for a 90° DW with dimensions of ∼40×40 nm.

Chapter 8

Programmable Logic Device

In the end of chapter 6 we give a description how to combine our fully electrically controllable Read-Write device with a non-volatile-memory device of ref. [Papp 07c] to a programmable logic element. The key element in the device concept is a narrow constriction, which serves as the output for the logic element. According to [Papp 07c] the constriction resistance is dependent on the relative magnetization states of the connected (Ga,Mn)As nanobars and thus able to distinguish between relative magnetization states (Head-to-Head, Tail-to-Tail and Head-to-Tail) of the two magnetic regions. Each of the two nanobars of [Papp 07c] has a uniaxial magnetic anisotropy and thus only two non-volatile magnetization states at zero field. In the non-volatile states the magnetization is parallel the long axis of the bar. However, the device concept shown in section 6.2 connects two magnetic biaxial disks and each disk has four non-volatile magnetization directions at zero field.

8.1 Characterization of the Individual Logic Bits

Fig. 8.1 shows an SEM picture of the logic device. The element consists of two central disks which are connected via a $\sim$ 15 nm narrow constriction. Each disk is contacted by three 200 nm wide nanobars which are aligned either along a [100] or a [010] crystal direction of the (Ga,Mn)As host material. The longitudinal resistance and thus the magnetization direction of each nanobar can be measured with Ti/Au contacts in a two terminal configuration. Similar to the Read-Write element the TAMR contacts serve as magnetization read-out of the central disks. The tunnel barriers are made of (0.9 + 0.6) nm AlOx deposited in a magnetron sputtering chamber. Both central disks have a diameter of 650 nm and at the transition from nanobars to disk we patterned down small notches to pin down a DW. The processing of the logic device is similar to processing of the read-write device described in section 6.1.

The constriction resistance serves as output during the logic operation. The $\sim$ 15 nm

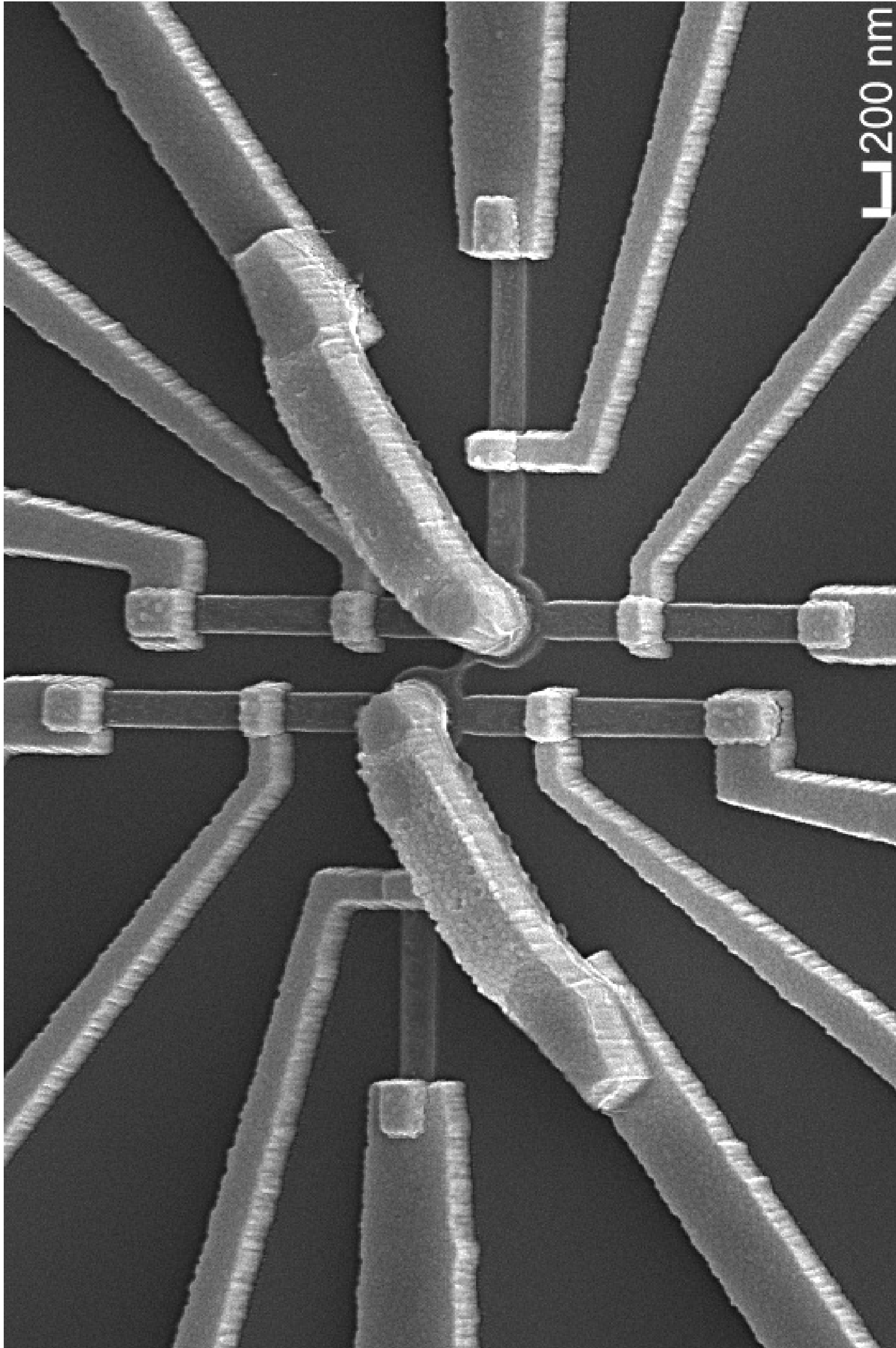

Fig. 8.1: SEM picture of a Logic-Device. Two metallic air bridges out of Gold contact the two central disks. Each of the three nanobars connected to a central disk is contacted by two Ti/Au wires. The two central disks are connected with a ∼15 nm small constriction

narrow constriction is fully strained relaxed perpendicular to the orientation of the constriction and the (Ga,Mn)As material within the constriction is depleted and shows a nonlinear IV-dependence compared to a usual linear IV-relation for ”metallic” (Ga,Mn)As. The IV measurement shown in fig. 8.2b is taken in a four terminal configuration by sending the current from $I_{+,constr}$ to $I_{-,constr}$ and measuring the voltage at $V_{+,constr}$ and $V_{-,constr}$ as sketched in fig. 8.2a (schematic yellow contacts) to rule out any contact resistance effects during the measurement. The constriction is in a nonlinear transport regime, where the valence band holes bound to active Mn impurities inside (Ga,Mn)As start to play a major role. In this hopping regime the dependence of transport effects on magnetization direction increases, because of the magnetization dependence of the impurity wave functions in (Ga,Mn)As [Schm 07].

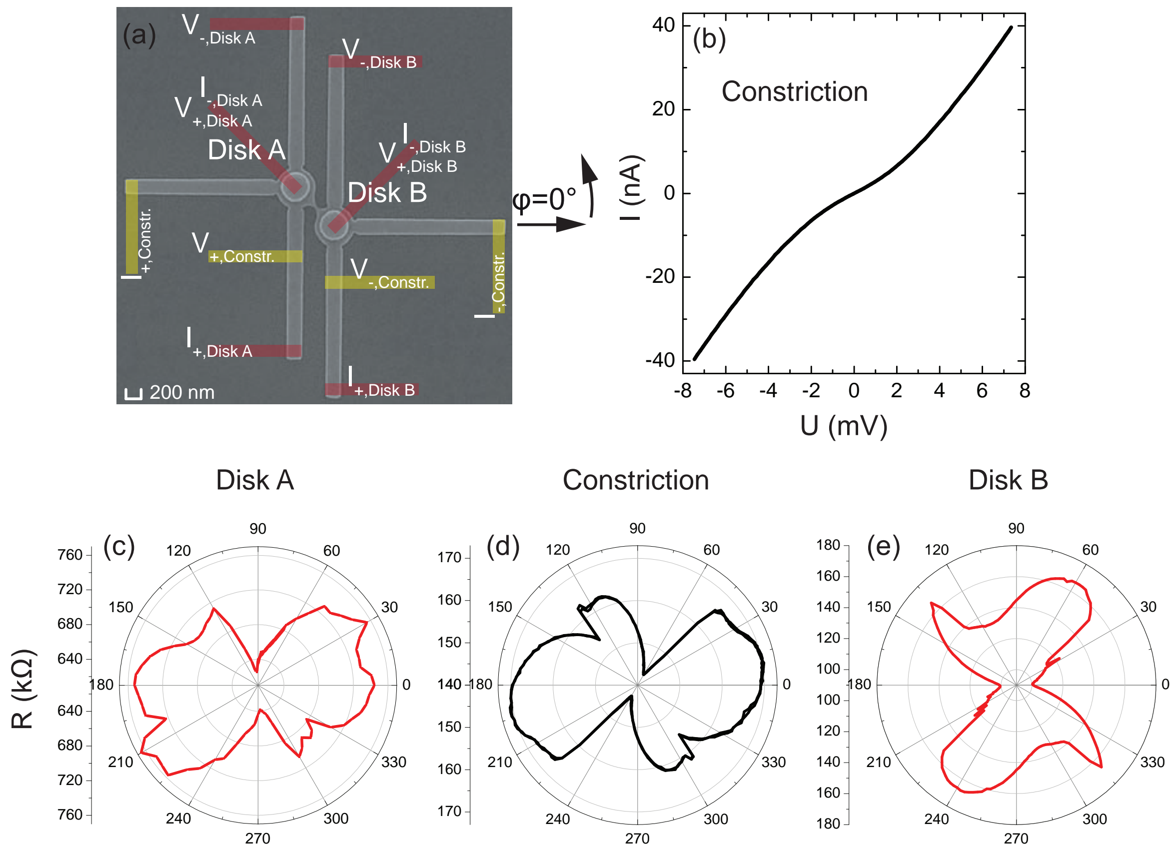

Fig. 8.2: (a) SEM picture of a logic-device with schematic contacts. Yellow contacts depict the measurement configuration of the constriction and schematic red contacts display the three terminal configuration of the TAMR read-out. (b) Non-linear IV measurement of the constriction. (c,d,e) Angular dependence of the magnetization in a 300 mT applied field for disk A (three terminal TAMR measurement), constriction (four terminal longitudinal measurement) and disk B (three terminal TAMR measurement), respectively.

Figure 8.2c, d, e show the in-plane angular dependence of the magnetization in a 300 mT magnetic field for disk A, the constriction and disk B, respectively. The amplitude

of the TAMR measurements of disk A and disk B have opposite signs for the [100] and [010] crystal direction, an effect described in section 5.1.2. Disk A has high resistance for magnetization along [100] and low $R_{TAMR,DiskA}$ for M along [010], the opposite is true for disk B. The constriction shows a M-φ dependence with a MR amplitude of $\sim 20\%$, which additionally excludes usual (Ga,Mn)As AMR (~3% amplitude) as the dominating effect in the constriction.

To reveal the exact magnetic anisotropies of the individual elements we record various magneto resistance measurements and compile them into RPP's for disk A, constriction and disk B (fig. 8.3). The resistance polar plots of the two central disks show a four-fold symmetry and thus the (Ga,Mn)As material of the two disks have a mainly biaxial magnetic anisotropy. The second anisotropy components along [010] and [$\bar{1}$10] of both (Ga,Mn)As disks are increased similar to the central disk of the read-write device discussed in section 6.3. The single MR measurements of the two disks parallel to the 15° direction next to the respective RPP show a usual (Ga,Mn)As double step process for the 90° magnetization reversal at H_{c1} and H_{c2}. At H_{c1} M switches from 180° to 90° and at H_{c2} M changes its direction from 90° to 0°. At H_{c1} the TAMR read-out of the central disk A changes from high to low resistance. Due to the opposite amplitude of the TAMR read-out of disk B the resistance changes from low to high. However, both TAMR measurements show two clear distinct switching events. Contrary to that, the single magneto resistance measurements of the constriction parallel to the 15° has four abrupt resistance changes. This results in the RPP of the constriction in four distinguishable resistances and thus four different color areas in the RPP (black, green, blue and red).

8.2 Logic Device Operation

To further investigate the switching behavior of the constriction we prepare an initial magnetization configuration as shown in fig. 8.4b. We use a lock-in technique combined with an AC-voltage having a frequency of 117 Hz to measure the TAMR resistance of disk B and simultaneously measure the constriction resistance with a DC-voltage. In the following we consider the top panel of fig. 8.4. In the initial state the magnetization of both disks is parallel to 180°, and depending on the orientation of the long axis the magnetization of the nanobars is either parallel to 90° or 180°, fig. 8.4b. Starting from zero field and sweeping the magnetic field along 90° the magnetization of disk B switches parallel to the field at 9 mT, which results in a resistance change from low to high in the TAMR read-out of Disk B (black measurement in fig. 8.4a). A change in constriction resistance coincides with the magnetization switch of disk B and changes its value at 9 mT from ~ 190 kΩ to ~ 200 kΩ (red in fig. 8.4a). The current magnetic configuration is shown in fig. 8.4c. By increasing the field the TAMR resistance of disk B remains constant

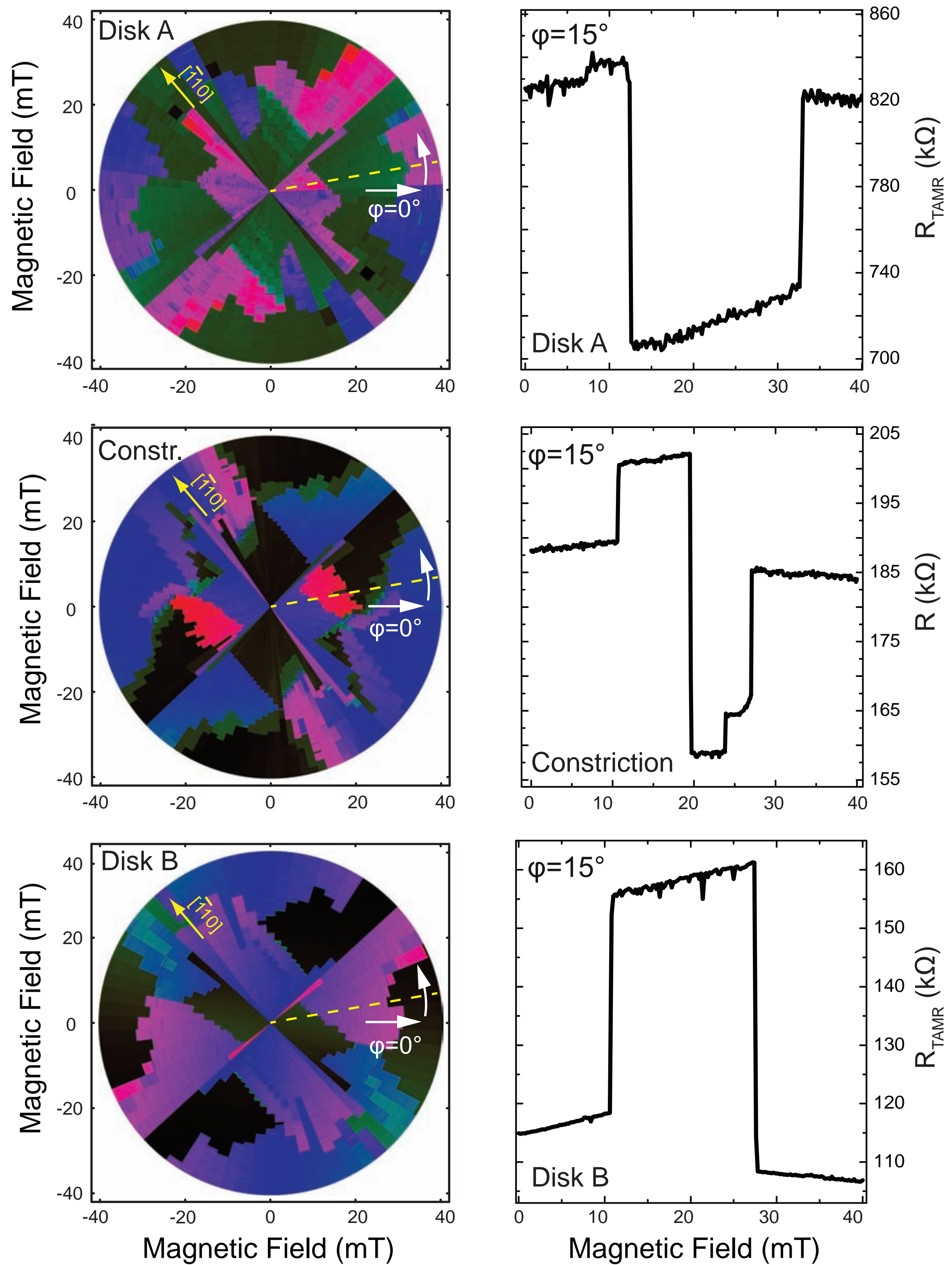

Fig. 8.3: RPP and a single magneto resistance measurement parallel to the $\varphi = 15°$ direction for disk A (first row), the constriction (second row) and disk B (third row).

at ∼ 192 kΩ, whereas the constriction resistance changes a second time to a low state (∼ 160 kΩ at 21 mT). This second resistance change originates from the magnetization reorientation of disk A from 180° to 90° (magnetic configuration of fig. 8.4d).

Now we consider the bottom panel of fig. 8.4 and prepare again the initial state and sweep the magnetic field to 8 mT along 90°. Analogue to the read-write operation in chapter 6.3 we can switch the magnetization by the means of a spin polarized current. Sending a current I_1 along the appropriate nanobars from contact A to B through disk B, the magnetization of disk B switches parallel to the magnetization of the source and drain nanobars. Thus the TAMR read-out of disk B changes from low to high resistance and additionally the constriction resistance changes from ∼ 190 kΩ to ∼ 200 kΩ (red measurement). This constriction resistance change is analogue to the resistance change at 9 mT described above by sweeping a magnetic field. While increasing the magnetic field the TAMR read-out remains in its high state and $R_{constriction}$ switches to its low resistance at 23 mT.

We prepare a third time the initial state and until the magnetic field sweet along 90° reaches 18 mT we perform the identical experiment described in previous paragraph. At 18 mT the magnetization of disk A can be switched from 180° to 90° by applying a current between contact D and C which results in a low resistance signal for the constriction and no change of the TAMR read-out out of disk B (green and gray in fig. 8.4g, respectively). The TAMR read-out of disk A is measured separately and changes its resistance from high to low (not shown). This shows that the second resistance change in the constriction originates from the magnetization reorientation of disk A.

Switching the magnetization of both disks with an electrical current can be detected in the TAMR read-out of the respective disks and by a change in the constriction resistance. Thus we have shown that the constriction indeed can serve as a tool to read-out the relative magnetization states of the two connected disks. The measurements shown above are taken at the constriction and disk B. Measuring disk A in combination with the constriction yields an analogue result.

Having confirmed the read-out ability of the relative magnetization states by the constriction we analyze the RPP of the constriction (fig. 8.3 center) in more detail. In order to be able to analyze the constriction RPP we normalize the RPP's of the individual disks. By normalizing is meant assigning the value zero to areas in the RPP's, where the magnetization of the individual disks is parallel or anti parallel to the [100] crystal axes and the parts, where the magnetization directions are along [010] or [0$\bar{1}$0], are set to one. Zero is the low value and appears black and one is high and appears red in the normalized RPP's, fig. 8.5d and e. Now the different colors in the normalized RPP should be interpreted as different magnetization directions rather than different resistances. The white arrows in the respective areas show the magnetization directions of the disks.

Combining the two normalized RPP's of the individual disks in a single RPP results in regions, where the magnetizations of the two disks are parallel or perpendicular, fig.

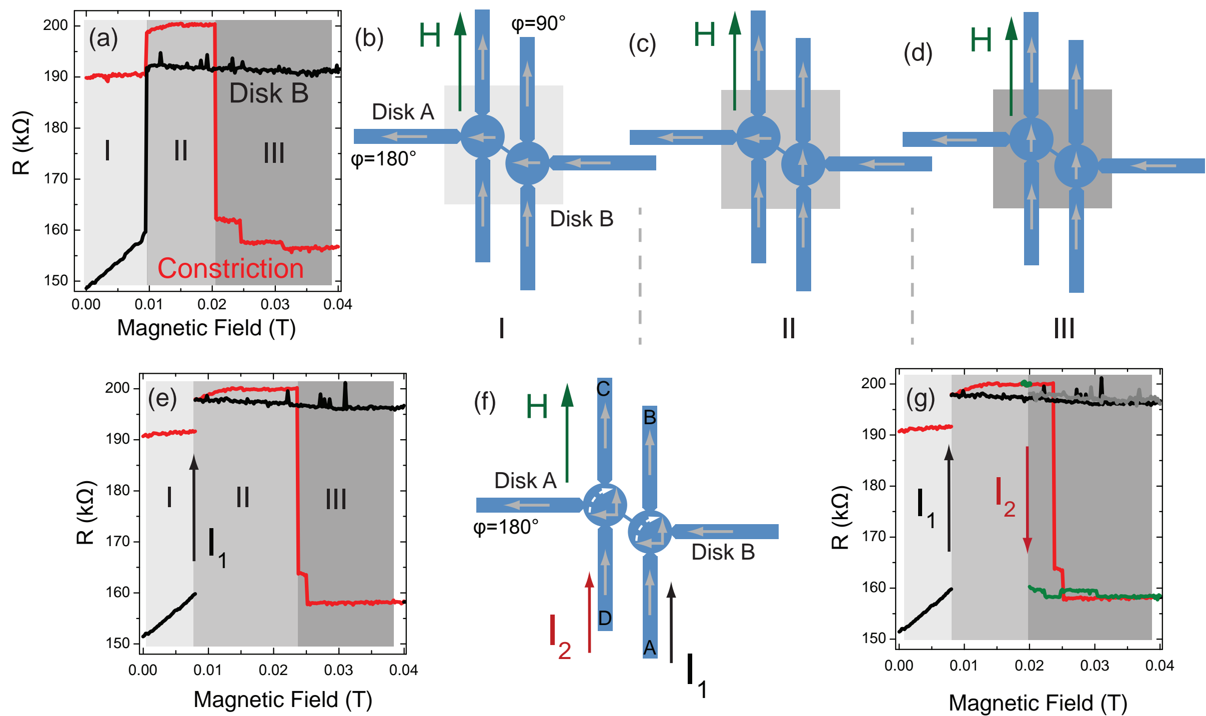

Fig. 8.4: (Top panel) TAMR measurement of disk B (black) and MR of the constriction (red) starting from an initial state (first sketch and light gray zone in the measurement) and sweeping the magnetic field along 90°. The second and third sketch show the magnetization configuration of both disks for the second and third zone depicted in the measurement with medium and dark gray. (Bottom panel) Switching of the magnetization of disk B by the means of current-assisted magnetization switching at an applied field of 8 mT along 90° (left). Experimental configuration of the logic-device (central). The magnetization of both disks is switched by current-assisted magnetization switching (right).

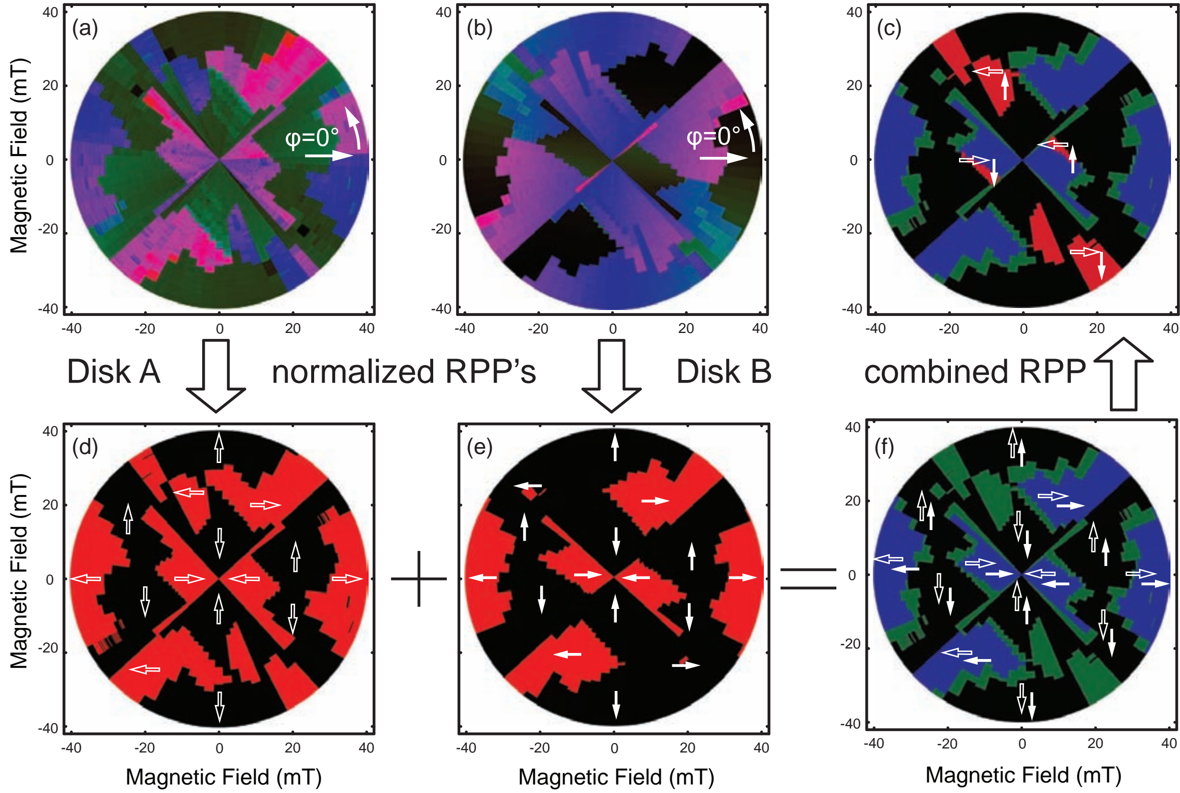

Fig. 8.5: Measured RPP of disk A (a) and disk B (b). Normalized RPP's of disk A (d) and disk B (e) including arrows of the respective magnetization direction. (f) Combined RPP stemming from a combination of the normalized RPP's of disk A and B. (c) Coloring a 90° magnetization state red in the combined RPP.

8.5f. If the magnetization of both disks is parallel or anti-parallel to the [100] crystal direction the combination yields zero ($0_{DiskA} + 0_{DiskB} = 0_{Combined}$), which appears black in the combined RPP. On the other hand, if M of both disks are along [010] axis the sum yields two ($1_{DiskA} + 1_{DiskB} = 2_{Combined}$) and appears blue in the combined RPP. For magnetization state, where the magnetization of one disk is parallel or anti parallel to the [100] axis and the magnetization of the second disk is aligned along [010] or $[0\bar{1}0]$ yields one in combination ($1_{DiskA} + 0_{DiskB} = 1_{Combined}$ or $0_{DiskA} + 1_{DiskB} = 1_{Combined}$) and appears green in the RPP. The RPP for the combination of both disks is shown in fig. 8.5f and the individual switching fields H_{c1} and H_{c2} of both disks are visible. Green in the RPP shows the combination where the relative magnetization state of both disks is 90°.

Each disk has four non-volatile magnetization directions and both disks have in total 16 (4×4) different relative magnetization states. Not all relative magnetization states are accessible because the switching H_{c1} and H_{c2} of the individual disks do not differ enough to prepare e.g. an anti-parallel magnetization configuration. We now concentrate on the magnetization state, where M of disk A is along $[0\bar{1}0]$ (180°) and M_{DiskB} is parallel to [010]

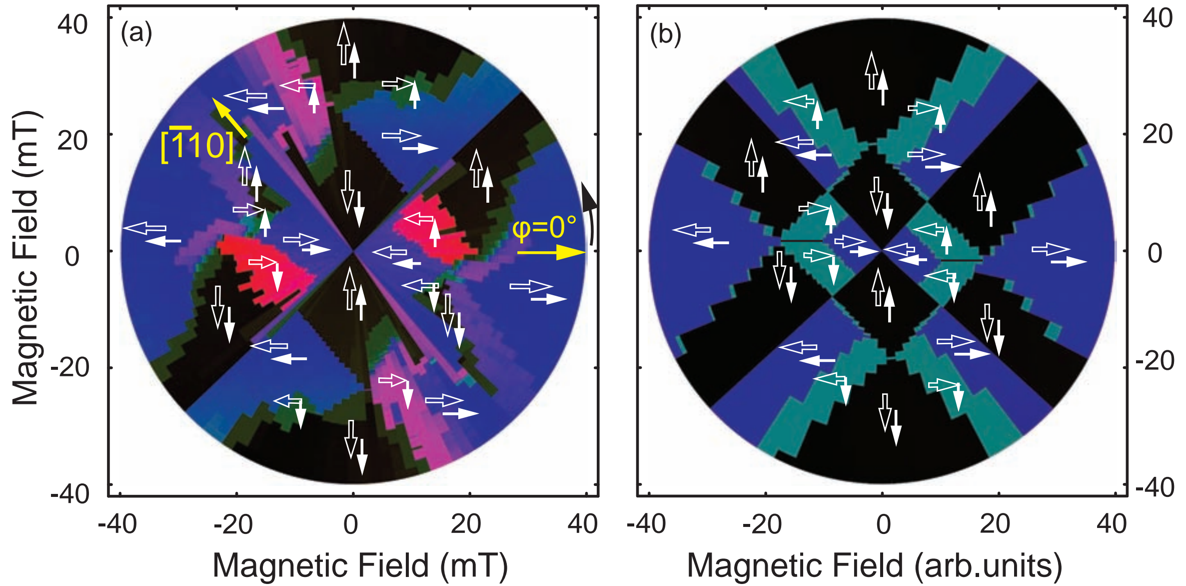

Fig. 8.6: (a) RPP of the constriction resistance. The arrows show the respective magnetization direction of the disk A (light grey) and disk B (white). (b) Combined RPP out of two calculated (Ga,Mn)As RPP's with different magnetic anisotropies.

(90°) and color this regions red in the combined RPP, fig. 8.5c. Analyzing the measured RPP of the constriction (fig. 8.3) and the combined RPP shows, that the switching fields H_{c1} and H_{c2} do not perfectly match but the combined RPP reflects the same symmetry as the RPP taken from the constriction. The imperfect match in switching fields of the individual disks compared to the constriction stems most likely from a break up into a multi domain state within the constriction. We presumably have magnetic domains at the transition from constriction to disk which do not strictly follow the reversal process of the disk. The magnetization state colored in red in the combined RPP reveals a maximum in constriction resistance and this areas appear red in the measured constriction RPP. Thus we can attribute the different areas in the measured constriction RPP to different relative magnetization states, fig. 8.6a. The exact microscopic origin of the resistance change is not clear up to now and needs further detailed investigations. To support our experimental result we calculated two (Ga,Mn)As RPP's with different magnetic anisotropies for comparison. Combining the two calculated RPP's similar to fig. 8.5f results in fig. 8.6b. Again the different colors should be interpreted as different magnetization states. Comparing calculated combined RPP in fig. 8.6b to the measured RPP of the constriction (8.6a) shows that both RPP reflect the same symmetry.

We have shown that the resistance of the constriction depends on the magnetization direction of the individual disks. First, switching an individual disk by current-assisted magnetization switching changes not only the TAMR read-out of the individual disk, but

additionally changes the constriction resistance. Second, the symmetry of the combined RPP generated from the RPP's of the individual disks is equivalent to the symmetry of the constriction RPP. The combined RPP of the calculated (Ga,Mn)As polar plots also support the experimental results.

Chapter 9

Conclusion and Outlook

In this thesis we realized an all-electrical, all-semiconductor logic element out of a ferromagnetic semiconductor. The key ingredients for (Ga,Mn)As device applications are local anisotropy control via anisotropic strain relaxation, miniaturization of the TAMR pillar size as a magnetization read-out tool at the 100 nm scale and the current induced switching mechanism for a local control of the magnetization direction.

Here we show the miniaturization of TAMR pillar size which opens the possibility of using the effect for device applications. The sub-micron pillars have an increased TAMR amplitude and are able to very locally sense the magnetization direction of different magnetic regions. The implementation of sub-micron TAMR pillars is successfully demonstrated in the device operation of the read-write and logic device. Since the TAMR effect is very sensitive to barrier properties and the details of the density of states, the resistance shows a complicated magnetization dependence. The barrier quality and local doping fluctuations are potential reasons for this dependence. One goal for the future should be to realize a crystalline barrier accompanied with a non-volatile resistance difference for the [100] and [010] crystal directions to exclude the barrier quality as the reason for the complicated resistance-magnetization dependence. Since (Ga,Mn)As is a disordered material system it will inherently have local doping fluctuations. By patterning a series of pillars with various diameters and a crystalline barrier it should be possible to identify the length scale, where local doping fluctuations start to influence the TAMR resistance, and thus the length scale of the inhomogeneities in the electronic density of states.

The fully electrically controllable read-write device demonstrated in chapter 6 is able to serve as one bit during a logic operation. The information is written by electrical means and is read-out by a non-destructive current. Combining two of the one bit demonstrator devices with a narrow constriction is the realization of a programmable logic device. The concept is introduced in chapter 6 and the realization is presented in chapter 8. The two central disks are the input bits and the constriction serves as the output of the logic

operation. In our logic concept each disk is connected to three nanobars contrary to the read-write device where the central disk has four attached nanobars. The source and drain nanobars of the read-write device have identical magnetization direction. That is not necessarily true for the logic device. However, for a fully functional programmable logic element we still need to show that the magnetization of a central disk switches its magnetization dependent on current direction when source and drain nanobars have different magnetization orientations. As an alternative one can change the logic device design in a way that four nanobars are connected to each disk.

As an aside project we investigate a FM metal/semiconductor heterostructure. The two layer hybrid system is studied using lateral transport and direct magnetization SQUID measurements. The independent magnetization behavior of the two ferromagnetic layers in direct contact is confirmed by both techniques. Transport studies in perpendicular device geometry sending the current through the interface are also performed during this work. At this stage the studies are inconclusive and need further investigations.

Appendix A

Uniaxial Nanobars

The authors of ref. [Weni 07] are first to report the realization of anisotropic strain relaxation in (Ga,Mn)As as a driving force to change the magnetic anisotropies of unpatterned layers to patterned nanobars. A comprehensive SQUID study of an array of nanobars and transport measurements are shown in [Hump 07] including a temperature dependence for compressively strained material grown on GaAs. E.g. a 200 nm wide nanobar relaxes its strain perpendicular to the long axis of the bar. Up to now all studies on anisotropic strain relaxation in (Ga,Mn)As have been performed on layers without any cover layers. Typically Ti is used as an etching mask to define the nanobars. The Ti is deposited ex-situ after an electron beam lithography step and the remaining Ti is removed with an HF:H_2O = 1:200 dip.

The layer stack used in our experiment requires an AlOx tunnel barrier and a Ti/Au cover layer to properly define and protect the barrier. These layers are deposited in-situ on top of the (Ga,Mn)As layer without breaking the vacuum. To investigate the reliability of the anisotropic strain relaxation effect in (Ga,Mn)As layers covered with in-situ metal, we pattern nanobars with different length parallel to the [100] and [010] crystal direction. The in-situ metal is removed from the nanobars during processing. The top panel of fig. A.1 presents an optical and SEM pictures of the experimental configuration showing nanobars with a length of 2 µm, 4 µm, 8 µm and 22 µm. Fig. A.1d presents longitudinal AMR measurements of a 8 µm long nanobar for magnetic field sweep angles of $\varphi = 0°$ (green), 30° (blue), 60° (red) and 90° (black) in a two terminal configuration. The current I is along $\varphi = 0°$ with respect to the [100] crystal axis. The measurement does not show a nanobar with a dominating uniaxial magnetic anisotropy. The resistance at zero field depends on magnetic field sweep direction and the magnetization of the nanobar has two non-volatile states, parallel and perpendicular to the long axis of the bar accompanied with two resistances at zero field. A nanobar with a dominating uniaxial magnetic anisotropy has only one resistance value at zero field reflecting the single magnetic easy axis. The field sweep along 90° (black) still shows a (Ga,Mn)As double step reversal process with an increased gap between H_{c1} and H_{c2}. For field sweep directions

parallel to 0° (green) and 30° (blue) magnetization reverses its direction at once. The uniaxial magnetic anisotropy component along the nanobar is enhanced, but the biaxial component is still significantly present. In this sample the described behavior is present independent of orientation and length of the nanobars. In other samples we observe some nanobars with a mainly uniaxial magnetic anisotropy, which have been formerly covered with in-situ metal. To enhance the strength of the anisotropic strain and thus increase the reliability of the uniaxial anisotropy component, we grow an additional 70 nm pseudomorphic (In,Ga)As layer which acts as a stressor to the overlying 70 nm (Ga,Mn)As layer [Weni 07]. Fig. A.1e shows two terminal AMR measurements on such a layer. Again the in-situ metal is removed during the patterning. The resistance of the nanobar at zero field is in its low state independent of field sweep direction and thus reflects a dominant uniaxial magnetic anisotropy. The magnetic easy axes is aligned parallel to the long axis of the nanobar.

We have shown, that the anisotropic strain relaxation mechanism does not reliably produce 200 nm nanobars with a magnetic uniaxial anisotropy when the (Ga,Mn)As material is covered with in-situ metal. Similar observations are made in our group for (Ga,Mn)As layers covered with in-situ Ti/Au. The exact mechanism of this phenomena remains unclear. An origin could be that after removing the in-situ metal some mono-layer islands of in-situ metal remain on top of the (Ga,Mn)As and prevent the material to relax its strain. To make sure the anisotropic strain relaxation effect is strong enough to generate a magnetic uniaxial anisotropy one can grow an additional underlying pseudormorphic (In,Ga)As stressor layer.

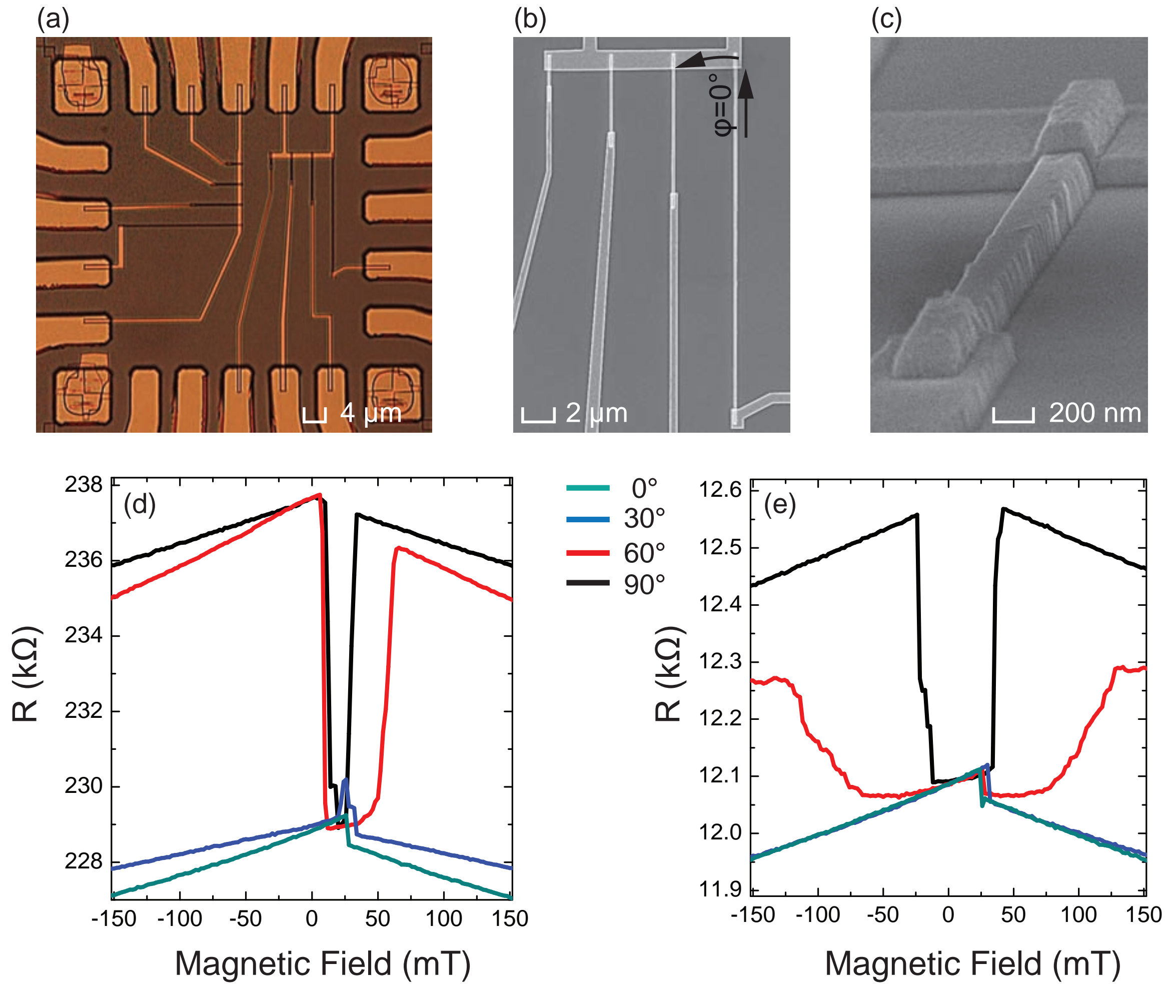

Fig. A.1: (a) Various 200 nm wide (Ga,Mn)As nanobars patterned of material with in-situ AlOx and Ti/Au elongated parallel to the [100] and [010] crystal axis. The in-situ metal is removed from the bars before measuring. The length of the bars is 2 µm, 4 µm, 8 µm and 22 µm. (b) SEM of nanobars with different length along the [010] crystal direction. (c) side view of a 2 µm long bar contacted by two Ti/Au contacts for measuring the longitudinal AMR resistance. (d) AMR measurement of a 8 µm every $\Delta\varphi = 30°$ starting with a field sweep parallel to the long axis of the bar (green) and ending with a perpendicular field sweep (black). (e) AMR measurement of a nanobar patterned from an identical layer stack as (d) including a 70 nm pseudomorphic (In,Ga)As layer which acts as a stressor to the overlying 70 nm (Ga,Mn)As layer to enhance the anisotropic strain effect.

Appendix B

Picture Gallery

The chapter shows some particular SEM and optical microscope pictures of some samples.

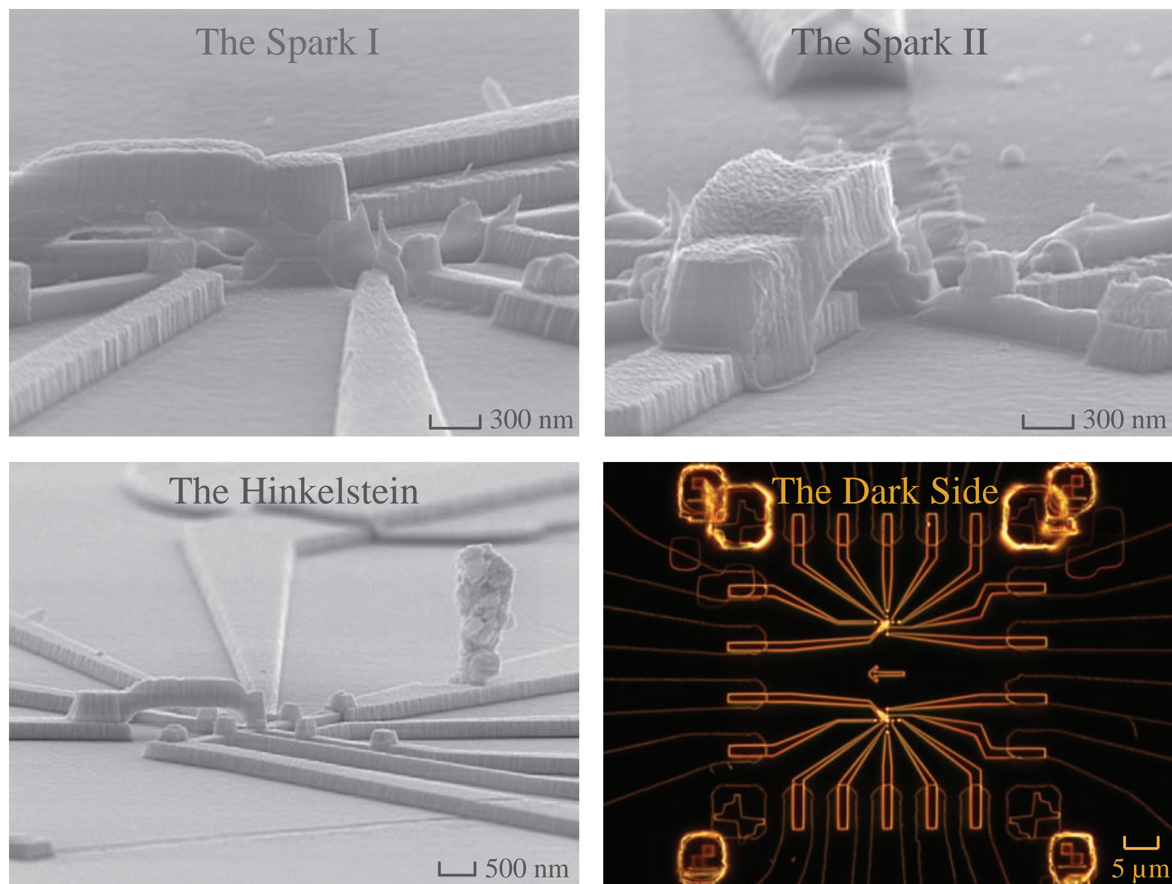

Fig. B.1: The Spark I/II: Read-Write device which is destroyed due to a high voltage spark. The (Ga,Mn)As material exploded while the metallic air bridge is not damaged. The Hinkelstein: During cleaving the sample a piece of GaAs substrate fall onto a Ti/Au lead. The Dark Side: optical microscope picture of the write field of a Read-Write device in dark field mode.

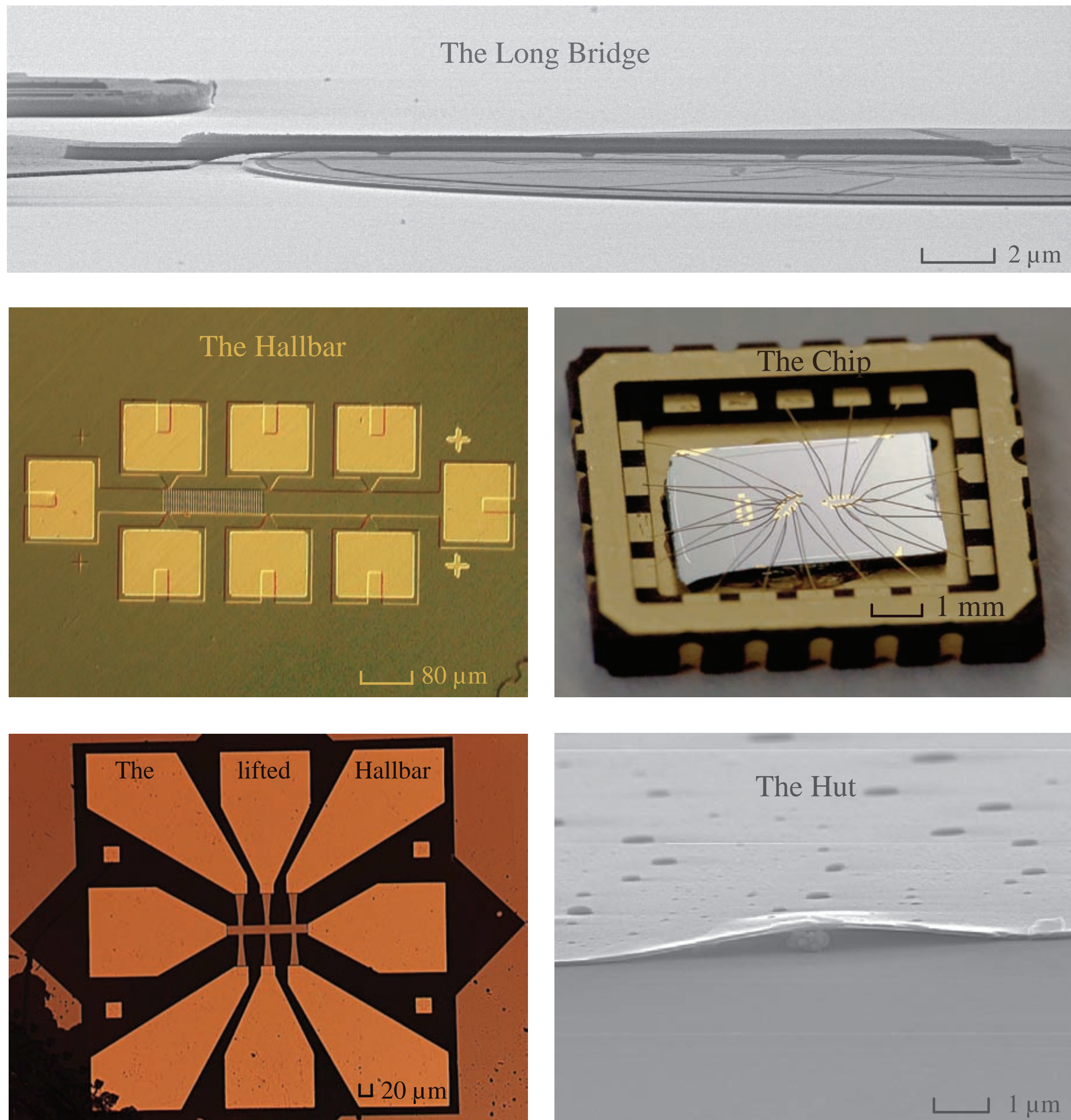

Fig. B.2: The Long Bridge: Side view of a hybrid system in perpendicular geometry. The permalloy ellipse is contacted by a metallic bridge including insulating posts. The Hall bar: Standard Hall bar geometry including an array of permalloy ellipses between the left and the central voltage pad. The permalloy ellipses are supposed to influence the magnetic anisotropies of the (Ga,Mn)As. The Chip: Standard chip carrier with a bonded sample. The sample includes three Hall bars along three different directions. Two Hall bars are bonded, photo by G. Dengel. The Lifted Hall bar: Hall bar geometry for a lifted (Ga,Mn)As layer. The Hut: SEM picture of a lifted (Ga,Mn)As layer [Greu 11]. Dirt is covered by the layer while putting the lifted layer back on a SiO substrate.

Bibliography

[Abol 01] M. Abolfath, T. Jungwirth, J. Brum, and A. H. MacDonald. *Phys. Rev. B*, Vol. 63, No. 5, pp. 054418–, 2001.

[Ahar 98] A. Aharoni. *J. Appl. Phys.*, Vol. 83, No. 6, pp. 3432–3434, 1998.

[Aker 02] J. Akerman, R. Escudero, C. Leighton, S. Kim, D. Rabson, R. W. Dave, J. Slaughter, and I. K. Schuller. *J. Magn. Magn. Mat.*, Vol. 240, No. 1-3, pp. 86–91, 2002.

[Aker 05] J. Akerman. *Science*, Vol. 308, No. 5721, pp. 508–510, 2005.

[Ashc 76] N. Ashcroft and N. Mermin. *Solid State Physics.* Thomson Learning, Inc., 1976.

[Awsc 07] D. D. Awschalom and M. E. Flatté. *Nat. Phys.*, Vol. 3, No. 3, pp. 153–159, 2007.

[Baib 88] M. N. Baibich, J. M. Broto, A. Fert, F. N. Vandau, F. Petroff, P. Eitenne, G. Creuzet, A. Friederich, and J. Chazelas. *Phys. Rev. Lett.*, Vol. 61, No. 21, pp. 2472–2475, 1988.

[Baxt 02] D. V. Baxter, D. Ruzmetov, J. Scherschligt, Y. Sasaki, X. Liu, J. K. Furdyna, and C. H. Mielke. *Phys. Rev. B*, Vol. 65, No. 21, pp. 212407–, 2002.

[Bina 89] G. Binasch, P. Grünberg, F. Saurenbach, and W. Zinn. *Phys. Rev. B*, Vol. 39, No. 7, pp. 4828–4830, 1989.

[Bock 09] T. Bock. *MgO Tunnelbarrieren auf (Ga,Mn)As Nanostrukturen,* Diplomarbeit, University of Würzburg, EP3. 2009.

[Borz 04] T. Borzenko, C. Gould, G. Schmidt, and L. W. Molenkamp. *Microelectron. Eng.*, Vol. 75, No. 2, pp. 210–215, 2004.

[Brei 08] R. Breitwieser, M. Marangolo, J. Luning, N. Jaouen, L. Joly, M. Eddrief, V. H. Etgens, and M. Sacchi. *Appl. Phys. Lett.*, Vol. 93, No. 12, p. 122508, 2008.

[Chan 67] L. L. Chang, P. J. Stiles, and L. Esaki. *J. Appl. Phys.*, Vol. 38, No. 11, pp. 4440–4445, 1967.

[Chen 09] L. Chen, S. Yan, P. F. Xu, J. Lu, W. Z. Wang, J. J. Deng, X. Qian, Y. Ji, and J. H. Zhao. *Appl. Phys. Lett.*, Vol. 95, No. 18, p. 182505, 2009.

[Chib 06] D. Chiba, M. Yamanouchi, F. Matsukura, T. Dietl, and H. Ohno. *Phys. Rev. Lett.*, Vol. 96, No. 9, p. 096602, 2006.

[Dahl 67] W. E. Dahlke and S. M. Sze. *Solid-state Electr.*, Vol. 10, No. 8, pp. 865–&, 1967.

[Diet 00] T. Dietl, H. Ohno, F. Matsukura, J. Cibert, and D. Ferrand. *Science*, Vol. 287, No. 5455, pp. 1019–1022, 2000.

[Diet 01] T. Dietl, H. Ohno, and F. Matsukura. *Phys. Rev. B*, Vol. 6319, No. 19, p. 195205, 2001.

[Fitz 06] M. R. Fitzsimmons, T. J. Silva, and T. M. Crawford. *Phys. Rev. B*, Vol. 73, No. 1, p. 014420, 2006.

[Gira 05] R. Giraud, M. Gryglas, L. Thevenard, A. Lemaitre, and G. Faini. *Appl. Phys. Lett.*, Vol. 87, No. 24, p. 242505, 2005.

[Goen 05] S. T. B. Goennenwein, S. Russo, A. F. Morpurgo, T. M. Klapwijk, W. Van Roy, and J. De Boeck. *Phys. Rev. B*, Vol. 71, No. 19, p. 193306, 2005.

[Goul 04] C. Gould, C. Rüster, T. Jungwirth, E. Girgis, G. M. Schott, R. Giraud, K. Brunner, G. Schmidt, and L. W. Molenkamp. *Phys. Rev. Lett.*, Vol. 93, No. 11, p. 117203, 2004.

[Goul 06] C. Gould, K. Pappert, C. Ruster, R. Giraud, T. Borzenko, G. M. Schott, K. Brunner, G. Schmidt, and L. W. Molenkamp. *Jpn. J. Appl. Phys*, Vol. 45, No. 5A, pp. 3860–3862, 2006.

[Goul 07a] C. Gould, K. Pappert, G. Schmidt, and L. W. Molenkamp. *Adv. Mat.*, Vol. 19, No. 3, pp. 323–340, 2007.

[Goul 07b] C. Gould, G. Schmidt, and L. W. Molenkamp. *Ieee Trans. Electr. Dev.*, Vol. 54, No. 5, pp. 977–983, 2007.

[Goul 08] C. Gould, S. Mark, K. Pappert, R. G. Dengel, J. Wenisch, R. P. Campion, A. W. Rushforth, D. Chiba, Z. Li, X. Liu, W. Van Roy, H. Ohno, J. K. Furdyna, B. Gallagher, K. Brunner, G. Schmidt, and L. W. Molenkamp. *New J. Phys.*, Vol. 10, p. 055007, 2008.

[Greu 11] F. Greullet, L. Ebel, F. Munzhuber, S. Mark, G. V. Astakhov, T. Kiessling, C. Schumacher, C. Gould, K. Brunner, W. Ossau, and L. W. Molenkamp. *Appl. Phys. Lett.*, Vol. 98, No. 23, p. 231903, 2011.

[Hage 67] F. B. Hagedorn. *J. Appl. Phys.*, Vol. 38, No. 9, pp. 3641–&, 1967.

[Hump 07] S. Hümpfner, K. Pappert, J. Wenisch, K. Brunner, C. Gould, G. Schmidt, L. W. Molenkamp, M. Sawicki, and T. Dietl. *Appl. Phys. Lett.*, Vol. 90, No. 10, pp. 102102–3, 2007.

[Inte 11] Intel. *Moore's Law evolves.* http://www.intel.com/technology/mooreslaw/, 2011.

[Jan 57] J. P. Jan. *Solid State Physics.* Academic Press Inc., New York, 1957.

[Jull 75] M. Julliere. *Phys. Lett. A*, Vol. 54, No. 3, pp. 225–226, 1975.

[Jung 06] T. Jungwirth, J. Sinova, J. Mascaronek, J. Kuccaronera, and A. H. MacDonald. *Rev. Mod. Phys.*, Vol. 78, No. 3, pp. 809–, 2006.

[Jung 07] T. Jungwirth, J. Sinova, A. H. MacDonald, B. L. Gallagher, V. Novak, K. W. Edmonds, A. W. Rushforth, R. P. Campion, C. T. Foxon, L. Eaves, E. Olejnik, J. Masek, S. R. E. Yang, J. Wunderlich, C. Gould, L. W. Molenkamp, T. Dietl, and H. Ohno. *Phys. Rev. B*, Vol. 76, No. 12, p. 125206, 2007.

[Lema 08] A. Lemaitre, A. Miard, L. Travers, O. Mauguin, L. Largeau, C. Gourdon, V. Jeudy, M. Tran, and J.-M. George. *Appl. Phys. Lett.*, Vol. 93, No. 2, p. 021123, 2008.

[Levy 97] P. M. Levy and S. Zhang. *Phys. Rev. Lett.*, Vol. 79, No. 25, pp. 5110–5113, 1997.

[Linn 97] M. Linnarsson, E. Janzén, B. Monemar, M. Kleverman, and A. Thilderkvist. *Phys. Rev. B*, Vol. 55, No. 11, pp. 6938–6944, 1997.

[Macc 08] F. Maccherozzi, M. Sperl, G. Panaccione, J. Minár, S. Polesya, H. Ebert, U. Wurstbauer, M. Hochstrasser, G. Rossi, G. Woltersdorf, W. Wegscheider, and C. H. Back. *Phys. Rev. Lett.*, Vol. 101, No. 26, p. 267201, 2008.

[Mark 07] S. Mark. *Transportmessungen an ferromagnetischen Metall/Halbleiter Hybridsystemen,* Diplomarbeit, University of Würzburg, EP3. 2007.

[Mark 09] S. Mark, C. Gould, K. Pappert, J. Wenisch, K. Brunner, G. Schmidt, and L. W. Molenkamp. *Phys. Rev. Lett.*, Vol. 103, No. 1, p. 017204, 2009.

[Mark 11a] S. Mark, P. Dürrenfeld, K. Pappert, L. Ebel, K. Brunner, C. Gould, and L. W. Molenkamp. *Phys. Rev. Lett.*, Vol. 106, No. 5, p. 057204, 2011.

[Mark 11b] S. Mark, L. Ebel, K. Brunner, C. Gould, and L. W. Molenkamp. *Submitted to Appl. Phys. Lett.*, 2011.

[McGu 75] T. R. McGuire and R. I. Potter. *IEEE Trans. Magn.*, Vol. 11, No. 4, pp. 1018–1038, 1975.

[Meik 56] W. H. Meiklejhon and C. P. Bean. *Phys. Rev.*, Vol. 102, No. 5, pp. 1413–1414, 1956.

[Mich 98] R. P. Michel, A. Chaiken, C. T. Wang, and L. E. Johnson. *Phys. Rev. B*, Vol. 58, No. 13, pp. 8566–8573, 1998.

[Mich 99] K. Michael. *Etching in Microsystem Technology.* Wiley-VCH, 1999.

[Nogu 99] J. Nogues and I. K. Schuller. *J. Magn. Magn. Mat.*, Vol. 192, No. 2, pp. 203–232, 1999.

[Nova 08] V. Novák, K. Olejník, J. Wunderlich, M. Cukr, K. Výborný, A. W. Rushforth, K. W. Edmonds, R. P. Campion, B. L. Gallagher, J. Sinova, and T. Jungwirth. *Phys. Rev. Lett.*, Vol. 101, No. 7, p. 077201, 2008.

[Ohno 08] H. Ohno and T. Dietl. *J. Magn. Magn. Mat.*, Vol. 320, No. 7, pp. 1293–1299, 2008.

[Ohno 96] H. Ohno, A. Shen, F. Matsukura, A. Oiwa, A. Endo, S. Katsumoto, and Y. Iye. *Appl. Phys. Lett.*, Vol. 69, No. 3, pp. 363–365, 1996. journal article.

[Ohno 98] H. Ohno. *Science*, Vol. 281, No. 5379, pp. 951–956, 1998.

[Olej 09] K. Olejnik, V. Novak, M. Cukr, J. Masek, and T. Jungwirth. *Journal of Crystal Growth*, Vol. 311, No. 7, pp. 2151–2154, 2009.

[Olej 10] K. Olejnik, P. Wadley, J. A. Haigh, K. W. Edmonds, R. P. Campion, A. W. Rushforth, B. L. Gallagher, C. T. Foxon, T. Jungwirth, J. Wunderlich, S. S. Dhesi, S. A. Cavill, G. van der Laan, and E. Arenholz. *Phys. Rev. B*, Vol. 81, No. 10, p. 104402, 2010.

[Papp 07a] K. Pappert, C. Gould, M. Sawicki, J. Wenisch, K. Brunner, G. Schmidt, and L. W. Molenkamp. *New J. Phys.*, Vol. 9, p. 354, 2007.

[Papp 07b] K. Pappert, S. Hümpfner, C. Gould, G. Schmidt, and L. W. Molenkamp. *PCT/CH2007/000390*, 2007.

[Papp 07c] K. Pappert, S. Hümpfner, C. Gould, J. Wenisch, K. Brunner, G. Schmidt, and L. W. Molenkamp. *Nat. Phys.*, Vol. 3, No. 8, pp. 573–578, 2007.

[Papp 07d] K. Pappert, S. Hümpfner, J. Wenisch, K. Brunner, C. Gould, G. Schmidt, and L. W. Molenkamp. *Appl. Phys. Lett.*, Vol. 90, No. 6, p. 062109, 2007.

[Park 99] S. S. P. Parkin, K. P. Roche, M. G. Samant, P. M. Rice, R. B. Beyers, R. E. Scheuerlein, E. J. O'Sullivan, S. L. Brown, J. Bucchigano, D. W. Abraham, Y. Lu, M. Rooks, P. L. Trouilloud, R. A. Wanner, and W. J. Gallagher. *J. Appl. Phys.*, Vol. 85, No. 8, pp. 5828–5833, 1999.

[Part 74] D. Partin, M. Karnezos, L. deMenezes, and L. Berger. *J. Appl. Phys.*, Vol. 45, No. 4, pp. 1852–1859, 1974.

[Read 07] J. C. Read, P. G. Mather, and R. A. Buhrman. *Appl. Phys. Lett.*, Vol. 90, No. 13, p. 132503, 2007.

[Rich 10] A. Richardella, P. Roushan, S. Mack, B. Zhou, D. A. Huse, D. D. Awschalom, and A. Yazdani. *Science*, Vol. 327, No. 5966, pp. 665–669, 2010.

[Rush 07] A. W. Rushforth, K. Výborný, C. S. King, K. W. Edmonds, R. P. Campion, C. T. Foxon, J. Wunderlich, A. C. Irvine, P. Vašek, V. Novák, K. Olejník, J. Sinova, T. Jungwirth, and B. L. Gallagher. *Phys. Rev. Lett.*, Vol. 99, No. 14, pp. 147207–, 2007.

[Rush 08] A. W. Rushforth, M. Wang, N. R. S. Farley, R. P. Campion, K. W. Edmonds, C. R. Staddon, C. T. Foxon, and B. L. Gallagher. *J. Appl. Phys.*, Vol. 104, No. 7, p. 073908, 2008.

[Rush 09] A. Rushforth, K. Vborn, C. King, K. Edmonds, R. Campion, C. Foxon, J. Wunderlich, A. Irvine, V. Novk, K. Olejnk, A. Kovalev, J. Sinova, T. Jungwirth, and B. Gallagher. *J. Magn. Magn. Mat.*, Vol. 321, No. 8, pp. 1001–1008, 2009.

[Rust 03] C. Rüster, T. Borzenko, C. Gould, G. Schmidt, L. W. Molenkamp, X. Liu, T. J. Wojtowicz, J. K. Furdyna, Z. G. Yu, and M. E. Flatté. *Phys. Rev. Lett.*, Vol. 91, No. 21, p. 216602, 2003.

[Rust 05a] C. Ruster, C. Gould, T. Jungwirth, E. Girgis, G. M. Schott, R. Giraud, K. Brunner, G. Schmidt, and L. W. Molenkamp. *J. Appl. Phys.*, Vol. 97, No. 10, p. 10C506, 2005.

[Rust 05b] C. Rüster, C. Gould, T. Jungwirth, J. Sinova, G. M. Schott, R. Giraud, K. Brunner, G. Schmidt, and L. W. Molenkamp. *Phys. Rev. Lett.*, Vol. 94, No. 2, p. 027203, 2005.

[Sacc 08] M. Sacchi, M. Marangolo, C. Spezzani, L. Coelho, R. Breitwieser, J. Milano, and V. H. Etgens. *Phys. Rev. B*, Vol. 77, No. 16, p. 165317, 2008.

[Sawi 04] M. Sawicki, F. Matsukura, A. Idziaszek, T. Dietl, G. M. Schott, C. Ruester, C. Gould, G. Karczewski, G. Schmidt, and L. W. Molenkamp. *Phys. Rev. B*, Vol. 70, No. 24, p. 245325, 2004.

[Schm 07] M. J. Schmidt, K. Pappert, C. Gould, G. Schmidt, R. Oppermann, and L. W. Molenkamp. *Phys. Rev. B*, Vol. 76, No. 3, p. 035204, 2007.

[Shen 97] A. Shen, H. Ohno, F. Matsukura, Y. Sugawara, N. Akiba, T. Kuroiwa, A. Oiwa, A. Endo, S. Katsumoto, and Y. Iye. *J. Cryst. Growth*, Vol. 175, pp. 1069–1074, 1997.

[Simm 63] J. G. Simmons. *J. Appl. Phys.*, Vol. 34, No. 6, pp. 1793–1803, 1963.

[Stil 99] M. D. Stiles and R. D. McMichael. *Phys. Rev. B*, Vol. 59, pp. 3722–3733, 1999.

[Ston 48] E. C. Stoner and E. P. Wohlfarth. *Philos. Trans. Roy. Soc. London*, Vol. 240, No. 826, pp. 599–642, 1948.

[Tang 04] H. X. Tang, S. Masmanidis, R. K. Kawakami, D. D. Awschalom, and M. L. Roukes. *Nature*, Vol. 431, No. 7004, pp. 52–56, 2004.

[Thei 03] T. N. Theis and P. M. Horn. *Phys. Today*, Vol. 56, No. 7, pp. 44–49, 2003.

[Welp 03] U. Welp, V. K. Vlasko-Vlasov, X. Liu, J. K. Furdyna, and T. Wojtowicz. *Phys. Rev. Lett.*, Vol. 90, No. 16, pp. 167206–, 2003.

[Weni 07] J. Wenisch, C. Gould, L. Ebel, J. Storz, K. Pappert, M. J. Schmidt, C. Kumpf, G. Schmidt, K. Brunner, and L. W. Molenkamp. *Phys. Rev. Lett.*, Vol. 99, No. 7, pp. 077201–, 2007.

[WinG] WinGreen. *http://www2.fz-juelich.de/ibn/index.php?index=341*.

[Wolf 01] S. A. Wolf, D. D. Awschalom, R. A. Buhrman, J. M. Daughton, S. von Molnar, M. L. Roukes, A. Y. Chtchelkanova, and D. M. Treger. *Science*, Vol. 294, No. 5546, pp. 1488–1495, 2001.

[Wund 07] J. Wunderlich, A. C. Irvine, J. Zemen, V. Holy, A. W. Rushforth, E. De Ranieri, U. Rana, K. Vyborny, J. Sinova, C. T. Foxon, R. P. Campion, D. A. Williams, B. L. Gallagher, and T. Jungwirth. *Phys. Rev. B*, Vol. 76, No. 5, p. 054424, 2007.

[Yama 04] M. Yamanouchi, D. Chiba, F. Matsukura, and H. Ohno. *Nature*, Vol. 428, pp. 539–542, 2004.

[Yu 99] Y. Yu and M. Cardona. *Fundamentals of Semiconductors*. Springer-Verlag GmbH, 1999.

[Zhu 07] M. Zhu, M. J. Wilson, B. L. Sheu, P. Mitra, P. Schiffer, and N. Samarth. *Appl. Phys. Lett.*, Vol. 91, No. 19, p. 192503, 2007.

Acknowledgements

It would not have been possible to prepare this work without the contribution and great support of many people. Thanks to all of you!!!

- First of all I would like to express my thankfulness to Prof. Laurens W. Molenkamp the head of the EP3 chair and the spintronics group for giving me the opportunity to work in his group and for all the discussions, guiding and support.

  Additionally, I want to thank:

- PD Dr. Charles Gould the leader of the spintronics group. Physics is about asking questions, and with his support, many questions could be answered. Charles, thanks for the insight of your scientific way of thinking, solving lab problems, improving my denglish and many fruitful scientific discussions. And of course thanks for many improving comments on this thesis.

- Prof. Georg Schmidt, the former leader of the spintronics group, for the opportunity to work with him and a lot of useful discussions about processing and clean room problems.

- Michael Rüth, Gabriel Dengel and Philip Hartmann, the members of C114a, for having a great working environment during the last four years. Thanks for the cheese cake day, fresh coffee in the morning, a brilliant trip to Krakow and many controversial scientific discussions.

- Bastian Büttner and Andreas Riegler for having a great time as lab-mates. Thanks to both of you and Florian Lochner for helping me with all the little hard- and software challenges.

- Fanny Greullet, Tsvetelina Naydenova, Jennifer Constantino and Marjan Samiepour in our "girls office" for giving the physics world a little non-scientific smile, but as well as for support during measurements and taking care of the cryostat.

- Katrin Pappert guiding me during my Diploma thesis and teaching me how to use the lab equipment. Thanks also for the hint with Stockholm and many advices to and during this Phd thesis.

- Tobias Bock for the help with the MgO tunnel barrier and Michael Freitag for helping with the ferroelectric-gate project.

- Lars Ebel for growing the (Ga,Mn)As wafers and chatting about the weekly soccer news. And special thanks to Tanja Borzenko and Volkmar Hock for support during processing and ideal clean room conditions. Not to forget many other people who contributed to discussions, measurement setups etc.: Petra Wolf-Müller, Roland Ebert, Hans, Tobias Kiessling, Claus Schumacher, Martin Zipf and everyone else from EP3.

- I also would like to gratefully acknowledge financial support from the German DFG (Schm1532/5-1).

- Ragi, Geischi and Yvo for a great time during the physics study.

- Finally, vielen vielen Dank an meine Familie für beides, die permanente Unterstützung und das ernsthafte Interesse an meiner Arbeit im Labor, aber auch dafür, dass ihr euch nicht zu sehr gekümmert und gesorgt habt. Danke Mama, Papa und Daniela.

- To Bianca: Thanks for your endless support and preventing me to think too much about physics problems back home. Special thanks for listening passionate to many of my exercise presentations.

Ehrenwörtliche Erklärung

gemäß §6 Abs. 3 und 5
der Promotionsordnung der
Fakultät für Physik und Astronomie
der Universität Würzburg

Hiermit erkläre ich ehrenwörtlich, daß ich die Dissertation selbständig und ohne Hilfe eines Promotionsberaters angefertigt und keine weiteren als die angegebenen Quellen und Hilfsmittel benutzt habe.

Die Dissertation wurde bisher weder vollständig noch teilweise einer anderen Hochschule mit dem Ziel, einen akademischen Grad zu erwerben, vorgelegt.

Am 02. Januar 2008 wurde mir von der Julius-Maximilians Universität Würzburg der akademische Grad 'Diplom-Physiker Univ.' verliehen. Weitere akademische Grade habe ich weder erworben noch versucht zu erwerben.

Würzburg, den

Stefan Mark